2

Materials Sciences Corporation

MICROMECHANICAL EVALUATION OF CERAMIC MATRIX COMPOSITES

Technical Final Report
MSC TFR 2201/1506
February, 1991

Contract No. F49620-88-C-0069

Prepared For:
AFOSR
Bolling AFB, DC 20332-6448

930 Harvest Drive, Union Meeting Corporate Center, Blue Bell, PA 19422
Tel: 215-542-8400 Fax: 215-542-8401

UNCLASSSIFIED

SECURITY CLASSIFICATION OF THIS PAGE

REPORT DOCUMENTATION PAGE

Form Approved
OMB No 0704-0188

1a REPORT SECURITY CLASSIFICATION
UNCLASSIFIED

1b RESTRICTIVE MARKINGS

2a. SECURITY CLASSIFICATION AUTHORITY

2b DECLASSIFICATION / DOWNGRADING SCHEDULE

3 DISTRIBUTION / AVAILABILITY OF REPORT
Approved for public release,
distribution unlimited

4. PERFORMING ORGANIZATION REPORT NUMBER(S)
MSC TFR 2201/1506

5 MONITORING ORGANIZATION REPORT NUMBER(S)

6a. NAME OF PERFORMING ORGANIZATION
Materials Sciences Corporation

6b. OFFICE SYMBOL (If applicable)
N/A

7a. NAME OF MONITORING ORGANIZATION
AFOSR

6c. ADDRESS (City, State, and ZIP Code)
930 Harvest Drive, Suite 300
Blue Bell, PA 19422

7b. ADDRESS (City, State, and ZIP Code)
AFOSR/NA
Bolling AFB DC 20332-6448

8a. NAME OF FUNDING / SPONSORING ORGANIZATION
AFOSR/NA

8b OFFICE SYMBOL (If applicable)
~~F08671~~ NA

9 PROCUREMENT INSTRUMENT IDENTIFICATION NUMBER
F49620-88-C-0069

8c. ADDRESS (City, State, and ZIP Code)
Building 410
Bolling AFB, DC 20332-6448

10 SOURCE OF FUNDING NUMBERS

PROGRAM ELEMENT NO.	PROJECT NO.	TASK NO	WORK UNIT ACCESSION NO.
61102F	2302/[illegible]	B2	

11. TITLE (Include Security Classification)
Micromechanical Evaluation of Ceramic Matrix Composites (U)

12. PERSONAL AUTHOR(S)
C-F. Yen, Z. Hashin, C. Laird, B.W. Rosen, Z. Wang

13a. TYPE OF REPORT
Technical Final Report

13b. TIME COVERED
FROM 88APR01 TO 28FEB91

14. DATE OF REPORT (Year, Month, Day)
February, 1991

15. PAGE COUNT
107

16. SUPPLEMENTARY NOTATION

17. COSATI CODES

FIELD	GROUP	SUB-GROUP

18. SUBJECT TERMS (Continue on reverse if necessary and identify by block number)
Ceramic Matrix Composite, Micromechanics, Failure mechanism, Crack propagation, Debonding, Energy Release Rate, Cyclic Loading, Residual Stress, Residual Strain, Hexagonal Array

19. ABSTRACT (Continue on reverse if necessary and identify by block number)

Analytical and experimental studies have been performed to investigate the thermomechanical properties and failure mechanisms in unidirectional ceramic composites in which the ceramic matrix is flawed and variable. Preliminary model for brittle matrix with a periodic hexagonal array of identical fibers has been analyzed on the basis of numerical fracture mechanics to assess criticality of various kinds of cracks. When this composite model is subjected to an axial load, it was found that transverse matrix cracks become unstable for perfect bonding and for disbonding between fibers and matrix, while disbond cracks propagating parallel to the fibers tend to stabilize.

The behavior of cracks in unidirectional ceramic composites has been investigated experimentally by observing the unidirectional strands in a ceramic cross weave, which was failed in tension. The failure surfaces show a characteristic feature of protruding groups of ruptured bundles, typically, consisting of 5-9 fibers. This has been attributed to the variability and flaws in the matrix and has formed the basis for the proposed failure scenario - transverse cracks are deflected by the longitudinal flaws and then grow axially to form so-called H shaped cracks (HSC).

20. DISTRIBUTION / AVAILABILITY OF ABSTRACT
☒ UNCLASSIFIED/UNLIMITED ☐ SAME AS RPT. ☐ DTIC USERS

21. ABSTRACT SECURITY CLASSIFICATION
UNCLASSIFIED

22a. NAME OF RESPONSIBLE INDIVIDUAL
Lt. Col. George Haritos

22b. TELEPHONE (Include Area Code)
202-767-0463

22c. OFFICE SYMBOL
NA

DD Form 1473, JUN 86 *Previous editions are obsolete.*

SECURITY CLASSIFICATION OF THIS PAGE

UNCLASSIFIED

19. Abstract (Cont'd.)

The behavior of the HSC has been analyzed based on a hexagonal model and a simplified axisymmetric cylindrical model with homogeneous transversely isotropic effective properties. The numerical studies reveal that the axial cylindrical cracks are stable and get arrested after propagating a sufficient distant. This is an important ingredient of the failure scenario. Damage accumulates in the form of HSC which ultimately merge to form the failure surface. Analytical results also show that the pull-out-length of a fiber-bundle depends on the ratio of the local critical values of energy release rates of mode I and mode II. The stiffness reduction due to HSCs has also been analyzed.

Cyclic loading experiments have revealed the phenomenon of residual macro-strain formation after each cycle, in spite of the fact that the material is elastic brittle. A theoretical explanation has been given on the basis of the thermal residual stress state due to the cooldown from fabricating temperature.

PREFACE

This reports presents the results of a study performed under Air Force Office of Scientific Research (AFOSR) - Contract No. F49620-88-C-0069. The Contract Monitor at AFOSR was Lt. Col. George K. Haritos. Dr. B. Walter Rosen was the program manager. At Materials Sciences Corporation, Dr. Chian-Fong Yen was the principal investigator and Dr. Zvi Hashin was a consultant. At the University of Pennsylvania, Professor Campbell Laird was the principal investigator and Dr. Zhongguang Wang was actively involved in experimental work.

Approved by:

B. Walter Rosen
President

TABLE OF CONTENTS

INTRODUCTION

The Air Force goal of developing high thrust-to-weight turbine engines depends strongly upon the advancement of high temperature ceramic composites. Ceramic materials retain stiffness at very high temperatures but their extreme brittleness precludes their use as a structural material, since cracks propagate easily and catastrophically. When a ceramic matrix is reinforced with unidirectional fibers the effect of cracks changes fundamentally. In this respect it is important to distinguish between fiber dominated and matrix dominated unidirectional ceramic fiber composites (UCFC). In the former the load is carried primarily by the fibers. UCFC with glassy matrix and graphite or Nicalon fibers are of this kind, since the fibers are so much stiffer than the matrix. When a crack forms in the matrix it can propagate transversely without rupturing the fibers thus forming what has been called in the literature a bridging crack. This kind of crack propagation has been extensively studied, notably in [1-4]. Several such bridging cracks can appear in sequence in a specimen loaded by monotonically increasing tensile load and the specimen will fail because of fiber rupture and pullout at some bridging crack location [5-9].

When fibers and matrix stiffness are of the same order, and there are cases when the matrix is stiffer than the fibers, the composite will be called matrix dominated. Examples are SiC matrix reinforced by graphite or Nicalon fibers. For such composites the failure mechanisms are entirely different. The tensile stresses in fiber and matrix are now of same order and either one of the constituents may now rupture locally. A local crack in the matrix of sufficient magnitude will produce significant local overload in fibers which will consequently rupture. Cracks in the matrix do not propagate easily in transverse direction because of the flaw distribution in a ceramic matrix produced by the large residual stresses due to the cool down during manufacturing. What emerges is a random accumulation of local failures at different locations which may merge to produce larger flaws, ultimately leading to catastrophic failure. It is with this kind of UCFC that the present work is concerned.

As an example of the behavior of the matrix dominated composite, consider the stress-strain curves of the SEP Nicalon fiber reinforced/SiC matrix composites shown in Figures 1 and 2, taken from [10]. Figure 1 shows measured tensile stress-strain curves which appear to be very nonlinear until failure. Figure 2 on the other hand shows compressive stress-strain curves which are linear until failure. This indicates that during tensile loading many cracks accumulate progressively in the specimen, thus the gradual reduction of stiffness which is manifested by the nonlinearity of the stress-strain relation. Compressive load, on the other hand, does not generate cracks, hence the linear-to-failure stress-strain relation shown in Figure 2.

In addition to the presence in the matrix material of cracks, photomicrographs of these composites show a high degree of porosity (Figure 3) and a very definite interphase between the fiber and the matrix (Figure 4). The porosity inhibits transverse crack propagation, as has been discussed above. The presence of an interphase is also liable to have significant effect on crack propagation.

The residual stresses may also play a significant role in the behavior of the matrix dominated ceramic composites. For example, the tensile stress strain curves shown in Figure 1 are for a 13 ply laminate, $[0/\pm60/90/\pm30/0_{1/2}]_s$. In the Nicalon/SiC composite the Young's moduli and thermal expansions of the fiber and matrix are of the same order. Classical laminated plate theory can apparently predict the initial modulus of this composite very well. The agreement between theory and experimental may be due in part to the low level of residual stresses in the constituents of this composite. The residual stresses are low because the fiber and matrix exhibit nearly the same thermal expansion coefficient. Therefore, very little microcracking is expected and the assumptions of laminated plate theory are valid.

On the other hand, the same laminate fabricated from Graphite/SiC, shows a much lower initial modulus in Figure 1. In this composite, although the moduli of the constituents are nearly the same, the thermal expansions are much different. The mismatch in thermal expansions results in residual tensile stresses in the matrix which may cause severe microcracking. The microcracking in the matrix, as well as the anisotropy of the graphite fibers, may be necessary to explain the much lower initial modulus of the graphite/SiC laminate.

The above observations suggest a rather complex failure approach. Hence, the primary effort in this program is to gain an understanding of the nature and importance of the various potential failure mechanisms.

We shall begin by investigating the criticality of various kinds of cracks in an ideal UCFC, including the effect of interphase. In particular we shall be interested in the criticality of transverse versus axial (in fiber direction) crack propagation. The experimental program is directed towards uncovering details of failure as well as nonlinear stress-strain relations under monotonic and cyclic loads. On the basis of the crack criticality studies and the experimental findings, a novel failure scenario is proposed and analyzed. Furthermore, a new theory for residual strain formation under cyclic load is constructed.

DEVELOPMENT OF LOCAL FAILURE MODELS

A critical objective of the local failure mechanism models is to assess the progression and arrest of dispersive local matrix cracks. This study is essential in identifying the key mechanisms that toughen and strengthen the ceramic composites. In this task, various possibilities of crack propagation in unidirectional ceramic matrix composites under tension have been examined on the basis of a hexagonal array model. Initial dispersive matrix cracks of various forms were first assumed. Then, the stability of the cracks progressing along different paths have been analyzed utilizing finite element methods together with fracture mechanics theories. The crack progression under the influence of various kinds of interphase has also been considered. It has been shown that transverse cracks become unstable for perfect bonding and for disbonding between the fibers and matrix, while disbonding cracks propagating along the fiber/matrix interface tend to stabilize. The approach and results are discussed in detail as follows.

APPROACH

In addressing local failure mechanisms at the early stages of composite damage growth, we first consider the idealized geometric model for the repeated matrix cracks perpendicular to the fibers illustrated in Figure 5. The model assumes a hexagonal array of identical fibers; and the repeating matrix cracks are spaced by a given number of fibers. Such a model has the required macroscopic transverse isotropy and the great advantage that its numerical analysis is confined to a typical repeating triangular element, Figure 5. This representative model has been analyzed by finite element methods on the basis of the ANSYS and ABAQUS codes developed by Swanson Analysis Systems, [11], and Hibbitt, Karlson and Sorensen, Inc., [12], respectively.

Potential surfaces of the crack growth were considered along the planar continuation of the initial matrix crack as shown in

Figure 5. We also considered the crack growth along the interfaces of all fibers at the point where they meet the existing matrix crack. The latter case resulted in fiber and matrix debonding.

Since no singular element was utilized, the stress intensity factors at crack tips could not be accurately calculated. Alternately, the energy release rate, G, at any point on the crack periphery was calculated. This was accomplished using the well established procedure of multiplying the concentrated line force at the crack periphery by half of the crack opening displacement gradient in the radial direction at the same location. The line forces were obtained from nodal reaction forces by distributing them evenly over the nodal spacing.

RESULTS

In this task SiC matrix composites reinforced with Nicalon fibers, P100 fibers or SiC monofilaments were considered. The monolithic SiC matrix has a Young's modulus of 66 Msi which is stiffer than the Nicalon fiber, Young's modulus of 29 Msi and softer than the P100 fiber, Young's modulus of 112 Msi. As it can be expected that the in situ matrix may be more compliant than the monolithic ceramic due to the presence of porosity and microcracks. A SiC matrix consisting 25% of spherical voids was also considered. The elastic properties of the porous matrix were evaluated on the basis of the differential scheme, [13]. It was found that the SiC matrix has a reduced Young's modulus of 37 Msi which is softer than the SiC monofilament, Young's modulus of 62 Msi. The SiC matrices, SiC monofilament and Nicalon fiber were considered to be isotropic, while the P100 fiber was transversely isotropic. The constituent properties are listed in Table 1.

(a) Ring Crack With Bridging Fibers

The finite element model for the repeating area of Figure 6 is shown in Figure 7. Note that the ring crack lies in the x-y plane (z=0), and extends from the fiber/matrix interface into the matrix with a length a. There were nine such rows of nodes and eight such rows of elements in z direction as that shown in Figure 7. Due to the nature of a repeating element, symmetric conditions were applied to the three planes defining the triangular area. Symmetric conditions were also applied to the plane z=o. The crack area had a traction free surface. A uniform displacement in z direction, u_{zo}, was imposed on the topmost layer of nodes at z=h, h being the total length in z direction.

For a 40% fiber volume fraction, the fiber radius, r_f, has the value of 0.332d, where d is the base of the repeated triangular area shown in Figure 7. With h=3.17d and u_{zo}=0.002d, finite element analysis was performed to compute the concentrated line force, which are perpendicular to the crack plane, at a nodal point on the crack periphery. Corresponding to the same nodal point, the crack opening displacement gradient in the radial direction was also calculated. The energy release rate of node I cracking, G_I, at this point was then computed by multiplying the line force by half of the displacement gradient. The results for these nodal points extending from the side A of the triangular area to the side B along the crack peripheries r_f and r_f+a (see Figure 7), respectively, are listed in Table 2. The constituents were Nicalon fibers and monolithic SiC matrix (SiC-1).

Uniform stresses, 41.8 ksi in the matrix and 18.4 ksi in the fibers, were computed at the boundary z=h. Note that the energy release rate on the crack periphery is proportional to the square of the applied stresses. Thus, based on the experimental values of critical energy release rates for matrix and fibers, it is possible to determine whether the crack will extend into the fiber or progress in the matrix. Note that the nearly constant values of energy rate along each of the crack peripheries shown in Table 2 demonstrate that the crack would propagate uniformly and remain as a ring crack. Furthermore, since usually there is a high axial shear zone extending along the fiber/matrix interface from the matrix crack tip where it meets the fiber, it is possible that fiber/matrix debonding may be occurred for a relatively weak interface strength. However, due to the lack of experimental data on these aspects, the progression of matrix crack and fiber debonding were determined qualitatively at the current stage.

By considering no fiber fracture or debonding, the matrix crack was assumed to extend in the same plane to various crack lengths, as shown in Figure 8. Note that the fourth and fifth cracks were assumed to meet the adjacent fibers at the interface without fiber fracture. Again, a uniform displacement of 0.002d in the fiber direction was applied at the boundary z=3.17d. The computed energy release rates at the crack peripheries of various crack lengths along the sides A and B of the repeating triangular area are listed in Table 3. It can be seen that the energy release rate increases with the increase of crack length until the crack meets the most adjacent fibers at $a/r_f=1.2$. The energy release rate then slightly decreases as the crack extended from $a=1.2r_f$ to $1.6r_f$. Since a crack is less stable with a higher value of energy release rate under the same loading condition, it can be expected that the crack started to propagate at $a=0.35r_f$ would propagate beyond the point where $a/r_f=1.66$.

(b) Circular Crack With Bridging Fibers

A circular plane crack embedded in the matrix shown in Figure 9 was also analyzed. The circular crack has a radius, a, of $0.5r_f$. Utilizing the same boundary conditions as that for the previous cases, the energy release rates at the nodal points on the crack periphery are shown in Table 4. The results indicate that the crack would propagate as a circular crack due to the nearly uniform values of energy release rate computed along the circular crack periphery. By comparing with the results of energy release rate in Table 2, we may also conclude that the circular crack would start to propagate at almost the same stress level as that for the ring crack of Figure 7.

(c) Ring Crack with Fiber/Matrix Interphase

Shown in Figure 10 is the repeating triangular area of Figure 5 with interphases between fibers and matrix. In the current analyses, an interphase thickness of 2.5% of the fiber radius, r_f, was assumed. In-plane ring cracks extending at three various locations with no fiber fracture or debonding were considered. The finite element model for the case with a crack length of $a_3 = 1.6r_f$ is shown in Figure 11. Note that wherever the matrix cracks meet the fibers, the crack fronts were extended one layer of small elements into the fibers. This ensured that the energy release rates in the fibers could be reasonably estimated. The constituents chosen here were the SiC monofilament and the SiC matrix with reduced modulus due to a 25% void content as listed in Table 1. The influence of the interphases on the crack progression was then analyzed by varying the interphase properties with respect to the matrix properties. Finite element analyses have been performed following the procedures similar to that described previously.

The computed energy release rates for an interphase with its Young's modulus, E_i, being 10% of the matrix Young's modulus, E_m, are compared with the results for no interphase, i.e., $E_i = E_m$, in Table 5. It is readily seen that the in-plane matrix crack is unstable with or without the interphases. Such an unstable character is similar to that shown in Table 3, only in the current case the fibers are stiffer than the matrix. The comparison in Table 5 also shows that the soft interphase reduces the values of energy release rates in the fibers and increases the energy release rates in the matrix. This reflects the fact that a soft interphase can protect the fiber by blunting the matrix crack front and retarding its penetration into the fiber. On the other hand, the soft interface provides a less constrained matrix, and thus allows the in-plane crack easier to extend in the matrix.

(d) Ring Crack With Fiber/Matrix Debonding

Next, the debonding characteristics of a unidirectional Nicalon fiber reinforced SiC matrix composite with the presence of initial matrix cracks perpendicular to the fiber direction as that shown in Figure 6 were studied. Here, we considered the composites consisting of Nicalon fibers and monolithic SiC matrix without interphase. The three-dimensional finite element model for $h/d=3.17$ and $r_f/d=0.332$ is shown in Figure 12. For this particular case, there are 141 elements in x-y plane and 14 rows of such elements in z direction. The model includes a ring crack in $z=0$ plane with crack length a. Then, extending from the interphase at which the plane matrix crack meets the fiber, a cylindrical crack surface parallel to the fiber with a length of b was embedded in the model (see also the insert at right of Figure 12). Note that the debonding crack was assumed to be symmetric with respect to plane $z=0$.

Finite element analyses were performed for the repeating volume with a uniform displacement $u_{zo}=0.002d$ in z direction imposed at $z=h$. The energy release rates were then calculated for the nodal points at the crack peripheries utilizing the previously described procedure. While the in-plane matrix crack (at $r=r_f+a$ and $z=0$) remains as mode I cracking, both mode I and II cracking were considered at the debonding crack periphery (at $r=r_f$ and $z=b$). However, it was found that for the debonding crack the energy release rate of mode I is usually an order of magnitude smaller than that of mode II and thus is negligible. The results for various values of a/r_f and b/r_f are listed in Table 6. Note that for the cases of $b/r_f=0$ the in-plane matrix cracks without fiber debonding were replicated.

It can be seen from Table 6 that the crack periphery extending into the matrix with a crack length, a, becomes more unstable as the debonding length, b, increased. This is also true for larger in-plane matrix crack length, a, with the same fiber debonding length. However, for a fixed value of a, the debonding crack becomes stabilized as the debonding increased. In general, an increase in the sizes of the cracks, a or b, results in more unstable conditions for crack growth. It can be readily seen that the sequence of crack growth can be quantitatively determined only if the corresponding fracture properties for the constituents and the interface can be accurately determined.

EXPERIMENTAL INVESTIGATION

INTRODUCTION

The purpose of the experimental investigation is to examine the stress-strain relations, damage and failure mechanisms and ultimate failure under monotonic and cyclic load for unidirectional ceramic fiber composites. We are specifically concerned with ceramic composites with variable matrix, which implies that there are relatively large flaws in the matrix which produce the variability. This, in contrast to the usual glassy matrix ceramic composite where the matrix is homogeneous. In the latter kind of composite the predominant damage is transverse cracking of the matrix in the form of matrix cracks which leave the fibers intact and traverse the whole specimen in transverse planes. Such cracks have become known as bridging cracks. By contrast, in variable matrix composites such cracks are not observed and the damage and failure mechanisms are different as will be described below.

Unfortunately, we were not able to find a materials supplier who manufactures unidirectional ceramic composites with variable matrix and as a result of our searches we have come to believe that unidirectional ceramic specimens are available only for glassy matrix. We, therefore, had to resort to different specimen configuration, namely a cross-ply weave composed of T300 carbon fibers which are embedded in a SiC matrix. The damage and failure mechanisms can thus be observed by examination of individual yarn bundles, and the stress-strain relation is also governed by the yarns in load direction. The material has been supplied by the Dupont company.

In the following we shall describe the experimental work performed for monotonic and for cyclic loading.

MONOTONIC LOADING

The external appearance of the as-supplied composite is shown in Figure 13. The composite is made up from several layers of carbon fiber bundle cross-weaves, inter-penetrated with SiC particles by a CVD process, coated with a layer of SiC, and the whole sintered into a rigid mass. The material was furnished in the specimen configuration shown in Figure 14 with the carbon plies oriented 0°/90°. The distribution of SiC was found to be highly inhomogeneous with a greater thickness existing between plies than between fibers in a bundle, which was reasonably close packed; the external layer of SiC was the thickest. The typical appearance of the intra-bundle regions, viewed by SEM, is shown in Figure 15. In this particular region, the fibers are not precisely close packed, but contacts between fibers numbering six were commonplace. In the region shown, there are three, four or five contacts per fiber. Figure 16 shows the Si map obtained by EDS technique corresponding to the region shown in Figure 15 and this confirms the chemistry of the SiC matrix. Note the highly defective nature of the matrix in which voids were commonplace both at fiber/matrix interfaces and within the matrix. Often these voids were found to be elongated in the fiber direction. The diameters of the fibers typically measured 7-8 μm.

In order to determine the purity of the materials used in the composite and to determine whether or not there was impurity segregation at the fiber/matrix interface, the composite was studied by Auger spectroscopy. Figure 17 shows a typical fracture surface of the composite broken in the high vacuum of the SAM in order to prevent contamination associated with preparing the sample in air. The fibers were examined both on their fracture surfaces and at the fiber/matrix interfaces revealed by pull-out episodes during the fracture sequence. Plots of the differential of observed Auger intensities against the electron energy are shown in Figure 18 for both matrix (Figure 18) and fiber interface (Figure 18), as read on a pulled-out fiber. Only Si and C were detected, the Si level being quite small for the fiber interface. This indicates a small residual adherence of SiC to the fractured interface and apparently no deliberate or accidental modification of the interphase structure.

Stress-Strain-Response - Monotonic Behavior

(a) Tensile Tests

Tensile tests were carried out with samples of the types shown in Figure 14 (gage section measured 3.2 by 8.1 by 40 mm). Tests were performed in an Instron servo-hydraulic machine, using a clip-on extensometer to measure strain. The tensile strain rate was about 10^{-5}/sec. The specimens were held by friction type grips, and testing alignment was achieved by using universal joints. After the tests were complete, the outer specimen surface and fracture surface were examined by SEM.

A typical stress-strain curve is shown in Figure 19. It turns out to be similar to the stress-strain curve for SEP Nicalon-SiC composite [10]. The material shows a fairly low elastic limit. The tensile behavior of the material was found to be highly nonlinear and it had a small measure of ductility. The E-modulus (tangent) decreases continuously from about 85 Gpa at the beginning of straining to about 36 GPa close to the ultimate stress level. An abrupt load drop occurred at an ultimate strength of about 437 MPa and a corresponding strain of about 1.05%. However, some load-bearing capability was retained beyond the ultimate load, such that further straining proceeded subject to a continuously decreasing stress.

The residual stresses inherited from processing due to differences between the thermal expansion coefficients of the matrix and fiber may have a major effect on the microstresses within a composite material and then play a significant role in the stress-strain behavior of the composite material. The residual stresses are, of course, additional to the stresses produced by external loads. Therefore, the residual tensile stresses in the matrix may cause severe microcracking during tensile loading even at a low stress level. Because the matrix is relatively stiff, cracks generating in the matrix and propagating through the composite during tensile loading can be expected to have a large, measurable effect upon the instantaneous composite stiffness. Therefore, it seems reasonable to suggest that the microcracking in the matrix and cracks propagating through the composite are responsible for the continuous reduction of the stiffness. Final failure of fiber bundles and the resulting link-up of multiple cracks in the matrix may be the fundamental processes which dictate the ultimate strength. The region of decreasing stress with increasing strain is associated with fiber pullout and delamination.

Figure 20 shows the reloading stress-strain curve of a specimen which was initially loaded to a stress of about 306 MPa, unloaded and then reloaded. Unlike the behavior shown in Figure 19 for the as-received specimen, the re-loaded specimen shows a large portion of linear stress-strain behavior. A deviation from linearity occurred at a stress of about 280 MPa, followed by the usual nonlinear region with reduced stiffness. Apparently, the presence of linear behavior resulted from the fact that numerous matrix microcracks generated in the previous loading exerted their effect on reloading and few new matrix cracks would be generated during tensile reloading until the previous highest stress was exceeded. However, when the reapplied tensile stress increased about 280 MPa, more matrix cracks were created and caused nonlinear behavior, resulting in a large increase in compliance or decrease in stiffness.

(b) Compressive Tests

As indicated above, the stress-strain response of matrix-dominated ceramic composites is mainly governed by the cracks which form internally in the brittle matrix. Therefore, one of the basic problems is to evaluate the stiffness reduction due to such cracks. Many investigations of this kind have been published in the literature but in literally all of them it is assumed that the cracks always remain open. This is a realistic assumption only if the tractions normal to the crack surfaces are tensile. When this traction is compressive, the crack will close and will thus have no effect on stiffness reduction. Compressive tests were performed in this study to verify this argument.

The compressive tests were carried out in a conventional Instron servohydraulic machine. Some of the problems with compressive testing are alignment difficulties, buckling and local crushing of the test specimen. A test fixture which is schematically shown in Figure 21 was specially designed for the tests. The compressive displacement of the specimen was measured by the attached sensitive extensometer. A typical example of a compressive stress-strain curve for the C/SiC cross-weave composite is shown in Figure 22. The design of the compression specimen wchih was cut from the end of the as-received specimen is also shown in Figure 22 as an insert. The initial nonlinear portion of the curve was obviously caused by the two ends of the specimen not being precisely parallel. After the initial portion, the compressive stress-strain curve was actually found linear up to the ultimate stress level. This behavior indicated that the growth of existing matrix cracks was suppressed and few new cracks generated. The ultimate stress level was associated with overall failure, involving particularly the buckling of fiber bundles and matrix fragmentation. A SEM micrograph (Figure 23) recorded right after the ultimate load was attained documented the situation. The continuous decline of load bearing capacity beyond the ultimate stress reflects the processes of fiber failure, matrix fragmentation and interlayer delamination.

Possible Fracture Processes

It was reported [14, 15] that tensile failure of a unidirectional SiC/glass ceramic composite included the following sequential processes: the development of a single crack that passes completely through the matrix, but remains bridged by intact fibers, formation of regularly spaced matrix cracks, fiber failure and pullout. However, the failure mechanism of cross-ply laminates becomes even more complex. Preliminary studies [16] on symmetric (0°/90°) SiC/LAS composite laminates indicated that tensile failure involves several stages of damage development with increasing applied load: edge delamination, matrix cracking in the 90° ply, matrix cracking in the 0° ply, and fiber failure in the 0° ply following by catastrophic delamination.

In addressing failure processes or local damage mechanisms, it is important to understand the relative roles of both fiber and matrix variability. For short fibers and a large matrix volume, the strength distribution functions of the two constituents are far apart, and extensive matrix cracking without fiber failure is likely. Conversely, for long fibers and small matrix volume, as in the present case, there may be an overlap in the strength distributions of the two phases. It is this latter case which motivates consideration of the early stages of damage growth. It will be appropriate to address matrix microcracking which may be followed by any of the following types of damage: fiber debonding, fiber fracture, matrix crack propagation past unbroken fibers, and the formation of multiple micro-cracks.

A notched specimen small enough to fit easily into the SEM sample chamber was used for studying the sequential failure processes in tension. Figure 24 shows a typical load versus crosshead displacement curve for such a specimen tested in tension. The configuration of the specimen is also shown in Figure 24. The appearance of the central part of a specimen before testing is shown in Figure 25, from which the edge damage by machining can be clearly seen. The specimen was first stretched to 2681 N (600 lbs.) (just above the knee of the tensile load-deflection curve, see Figure 24). The resulting damages were observed in the SEM and are shown in Figure 26. Notice that surface cracks are visible (Figure 26) and a single surface crack stretches right to the specimen edge, stimulating local fracture of fibers (Figure 26). The specimen was then reloaded, first to 4022 N (900 lbs.) and again to 4469 N (1000) lbs. The same areas were examined by SEM after each reloading. Figure 27, showing SEM micrographs, indicates little subsequent change in surface cracking and spalling even after loading to 4469 N (1000 lbs). The specimen was finally fractured at 6256 N. Figure 28 illustrates the appearance of the fractured specimen at both the top and side of the gage section. In comparison with the surface cracks shown in Figure 26 and 27, it is clearly seen that the final failure path lies exactly along the surface cracks observed early in the deformation process. Figure 28 also demonstrates the possible internal damage modes: fiber fracture, delamination and fiber pullout. It should be noted that the damage appeared more localized than normally observed for long specimens, reflecting the "notched" gage section of the short specimen used.

Characteristics of Fracture Surface

As indicated above, the tensile failure of a cross-weave C/SiC composite involves several damage modes which are governed by the fiber bundle and matrix variability. One of the most important sources of information relating to the case of failure is the fracture surface itself. A fracture surface shows a detailed record of the failure history of the specimen (which may be too complex to interpret confidently). The principal technique used to analyze fracture surfaces is electron fractography. Fundamental to the application of this technique is an understanding of how materials fracture and how the microstructure (for example, in composites, the constituents and their arrangements) affects the fracture process. Extensive fractographic studies were performed by scanning electron microscope (SEM) in the present work.

A macroscopic view of the fracture surface of a C/SiC cross-weave composite which had been tested in tension to complete fracture is shown in Figure 29. The fracture surface is characterized by fabric strands failed at various elevations, and extensive pull-out of fibers. Lateral and normal views of the fiber bundle fracture viewed at higher magnifications are shown in Figure 30 and 31, respectively. These show what is considered a characteristic feature of the fracture in the composite, namely, protruding groups of ruptured fibers. Essentially, a crack has formed and propagated transversely through a small group of fibers but then the cracks turn parallel to the specimen axis and produce fracture at the fiber-matrix interface, defining a small cylinder of fractured fibers. This group-linked fracture process is distinct from "fiber pullout" which generally follows matrix cracking rather than being part of it.

A typical number of fibers involved in this group process is not large, but appears to lie between 4 and 8. This fractographic evidence demonstrates that the composite does not fail because of one single dominant crack, being bridged by, and then rupturing, the fibers. Such a fracture surface is reminiscent of that of a unidirectional glass fiber/polymer matrix composite but in such a case single fibers protrude from the surface [17]. It is well known that a jagged irregular failure surface is caused by the accumulation of fiber breaks at random places, prior to failure. It, therefore, stands to reason that the failure surface for the ceramic composites results from a similar accumulation of flaws involving groups of fibers. This has led us to a failure scenario which concludes that transverse cracks are arrested by matrix voids, causing the cracks to grow along the fibers. After they have travelled some distance by fiber-matrix interface fracture, the cracks become stable and arrested. Therefore, fiber debonding and fiber group pull out are considered to be the two major damage modes in the early stages of the fracture process. Fractographic studies also revealed fiber debonding and pull out in the final stages of fracture as shown in Figure 32. Figure 32 also provides evidence that matrix cracks sometimes stimulate rupture of the fibers, causing them to be cut in the plane of the matrix crack.

Conclusions

Montonic loading deformation and fracture tests of C/SiC composite, coupled with microstructural observation of the damage, have led to the following summary and conclusions:

(1) The C/SiC cross-weave composite studied contains a variety of macro and micro voids: systematic gaps in the interstices of the weave and a variety of cylindrical microvoids within the ceramic-impregnated strands of the carbon fiber weave. No interphasial layer was found between the fibers and matrix.

(2) Specimens have been subjected to mechanical tests both in tension and compression. As expected, the behavior in tension and compression was found to be asymmetric. The stress-strain curve in tension and compression was found to be asymmetric. The stress-strain curve in tension shows a fairly low elastic limit, followed by a regime of inelastic behavior with a continuous reduction of stiffness. However, the stress-strain curve in compression and the tensile stress-strain curve of a pre-loaded specimen mainly show linear elastic behavior.

(3) The initial deviation from linearity in the tensile tests of as-received specimens is caused by the formation of matrix cracks. This microcracking process in the matrix is presumed to be governed by residual stresses. The ultimate failure occurs when such flaws interact and coalesce resulting in fiber bundle failure and pullout.

(4) The failure surface is very irregular in nature and consists of distinct groups of about 4-8 ruptured fibers

"pulled out" as a group from the matrix. Therefore, the propagation of one dominant crack is not the mode of failure. A possible failure scenario is that local cracks rupture similar fiber groups with transverse cracks which are arrested by the internal voids and then the cracks propagate in the fiber direction by fiber-matrix interface fracture until these cracks become self arrested. Catastrophic failure follows by the linking of these group fractures and ultimately, massive fiber debonding.

CYCLIC LOADING

Tension-Tension Cycling on Notched Specimen

The same ceramic cross-weave material was employed in the cyclic loading testing. Tests under tension-tension cycling were carried out with notched samples of the design shown in Figure 33 cut from composite strips. An Instron hydraulic machine was used to conduct the tests at frequencies in the range of 0.01 to 0.2 Hz. The specimens were held by friction type grips and the alignment was achieved by using universal joints. Load vs. displacement curves of the specimen were recorded during the test using an X-Y recorder with high sensitivity.

Figure 34 shows the cyclic stress-strain response associated with an exploratory ascending step test. Initially, the test was run at 605 of the fracture load using a low cyclic frequency, 0.01 Hz; further frequency increments were made later. The effects of the first 100 loading cycles were recorded continuously and indicate cyclic creep behavior. It is seen that the specimen exhibited a continuously decreasing cyclic creep rate with cycling and the cyclic creep behavior of the specimen was found to be frequency dependent. As can be seen from Figure 34, a change in frequency from 0.01 Hz to 0.08 Hz led to a transient acceleration of creep deformation at the first cycle (on the basis of elapsed time) and then the elapsed strain rate was found to decrease.

There is no obvious explanation so far for this remarkable observation. After 100 cycles of recording, the creep rate was typically observed to decrease and thereafter only occasional hysteresis loops were recorded. For the relatively few cycles of stress applied (1000), there was no sign that the creep finally abated. Figure 34 shows that two more loading steps were applied at 74 and 80% of the fracture load, respectively. Any load increment had the effect of greatly (if transiently) increasing the inelastic residuum (creep). The particular sample illustrated in Figure 34 failed at 80% of the monotonic fracture load after a total of 3680 cycles.

The development of cracking associated with cyclic creep was studied by SEM during test interruptions. Figure 35 shows the appearance of the central part of the sample before repeated loading. There were no surface cracks initially visible at the indicated magnification or at higher magnification. The specimen was first cycled for 1850 cycles under a tensile load range from 222N to 3782 N (60% of the fracture load), then cycled for 2500 cycles under a tensile load range from 222N to 4672N (74% of the fracture load) and finally cycled to failure under 222N to 5116N (81% of the fracture load). The total number of cycles to failure was found to be 4530 cycles. The cycling frequency was 0.05 Hz. The test was interrupted at 150 cycles and 850 cycles for investigation of the damage phenomena by SEM. Figure 36 indicates the same area as shown in Figure 35 but after 150 cycles surface cracks can be clearly seen after the specimen was exposed to repeated loading for this short period. Figure 37 shows the resulting damage to the specimen edge by cycling for 150 cycles. Figures 38 and 39 were taken from the same areas as shown in Figures 36 and 37, respectively, and show the multiplication of surface cracks and spalling episodes associated with a further cyclic exposure for 700 cycles. These cracks were clearly important in the ultimate failure of the specimen since they were ultimately incorporated into the final rupture as shown in Figure 40(a), (b), (c), and (d). Normally, the cracks seemed confined to the SiC matrix and appeared to avoid the bundles of carbon fibers. Occasionally, the cracks penetrated the bundles, cutting the fibers in the plane of the matrix crack. In comparison with the development of cracking under monotonic loading as reported in the section of monotonic loading, it seems here that repeated loading created more surface cracks and spalling. As indicated in Figure 34, on repeated loading there is a considerable creep. This is attributed to the opening of cracks under load and their failure to close completely on unloading, through their being propped open by debris.

Tension-Tension Cycling on a Smooth Specimen

In order to exclude the possible contributions to the irreversible strain on repeated loading from factors such as stress concentrations, flaws by machining (the specimen was cut from a strip) and specimen-grip interaction, a smooth specimen was used for tension-tension cyclic loading. A smooth specimen is one tested in the as received and as-processed condition, which was long enough to avoid possible grip-specimen interactions. The overall length of the specimen was 140 mm and it measured 3.2 x 8.1 mm^2 in section with a gage length of 40 mm. The experimental fatigue arrangement was similar to that used for the notched specimen except a clip-on extensometer was attached to the gage length to measure the strain over the gage length without involving grip effects. The specimen was first stretched to a stress of about 308 MPa (70% of the fracture stress) and then subjected to repeated loading under a tensile stress range from 8.75 MPa to 308 MPa. The cyclic stress-strain response in the first 100 loading cycles was recorded continuously and is shown in Figure 41. It is very interesting that on unloading there is a considerable inelastic strain residuum, about 20% of the strain applied. This residuum continues to increase on repeated loading after the first tensile application.

After 100 loading cycles, the test was interrupted and the specimen surface was observed using a stereo binocular microscope. No cracks were visible on the exterior surface of the specimen. A further 900 loading cycles were then imposed, but these caused little irreversible strain. SEM observation at high magnification revealed the existence of microcracks on the specimen surface as shown in Figure 42. In comparison with the notched sub-specimen, the full size smooth specimen gave much less inelastic strain residuum on repeated loading and fewer surface microcracks as well. Based on the results for both types of the specimen, the nonlinear behavior is tentatively interpreted in terms of microcracking behavior as follows: during load application, the existing population of flaws either open as microcracks or stimulate microcracking, the elastic deformation including the sum of the crack opening displacements. During unloading, a certain fraction of these cracks remains open to produce the strain residuum, because of wedging, we believe, by spalled fragments, or crack closure associated with surface roughness [18]. Figure 41 shows that repeated loading and unloading causes a slight creep strain, possibly by accumulation of these irreversibilities. The difference in behavior between the notched and smooth specimens reflects an increased population of flaws introduced by the machining of the notch.

From comparison of the fracture surface of a cyclically-failed specimen with that of a specimen broken in monotonic deformation, it seems that the mechanism of failure by cyclic loading is similar to that of monotonic loading but tends to be more gradual and somewhat more localized although it is possible that the use of a notched specimen forced the localization. A more definitive study of the failure mechanism will require examination over a wider range of load fractions and in the interior of the specimen. The latter represents a difficult problem because of the danger of artificially introducing cracks during specimen sectioning and preparation. Methods are under development to circumvent this problem.

Cycling Under Pulsating Compression Loading

As reported in the previous section, the matrix dominated composite C/SiC, subjected to compressive loading, mainly shows linear elastic behavior. Few matrix cracks were believed to be generated until the moment of final failure under compressive loading. It was previously shown [19, 20] that crack extension is often observed in ceramics during unloading from a compressive stress, a phenomenon which could be classified as a fatigue effect or could lead to a fatigue phenomenon. More recently, investigations on polycrystalline alumina indicated [21] that the application of fully compressive cyclic loads can lead to Mode I crack growth at room temperature. Therefore, the damage accumulation that occurs under cyclic compressive loads is a problem of particular interest and practical importance for ceramics, especially for cross-weave composites which contain ordered arrangements of voids as part of the weave structure. However, the fracture behavior of both monolithic ceramics and ceramic matrix composites under cyclic compression is not understood. Tests of compression-compression cycling were, therefore, performed in the present study in a preliminary attempt to analyze the compressive mode of fatigue.

Tests were carried out in a conventional Instron servohydraulic machine. A specially designed test fixture described previously was used to ensure adequate alignment and to measure the strain of the specimen during cyclic compressive loading. Figure 43 shows the cyclic stress-strain response associated with an exploratory three-step test. The configuration of the specimen, also shown in Figure 43, indicates that the cross-weave was oriented in a 0/90 arrangement. The specimen was first cyclically loaded under a compressive stress amplitude ranging from -7 MPa to -277 MPa for 100 cycles, then cycled for 550 cycles under a stress range from -7 MPa to -354 MPa, and finally cycled to complete failure under a stress range from -7 MPa to -382 MPa. The total number of cycles to failure was 1,000 cycles exactly (and fortuitously). A triangular wave form with a frequency of 0.2 Hz was used throughout the entire test.

Several interesting points were revealed in the results shown in Figure 43. Firstly, compressive cycling caused creep deformation, the rate of which declined with cycling and finally reached a saturation stage at a given stress level. Secondly, sudden, large increases of cyclic creep were observed during the cycling. These episodes can be seen as gaps in the generally solid bands of pen recordings traced out during the creep process. This phenomenon is reminiscent of strain burst behavior observed during cyclic deformation of metals and alloys [22-24]. Thirdly, a continuous acceleration of cyclic creep occurred during the onset of the final failure in the specimen.

A preliminary attempt was made to explain the observed phenomena in terms of the damage of the specimen. Figure 44 shows a SEM micrograph from a specimen which was cycled for 500 cycles under a loading pattern similar to that shown in Figure 43. It can be seen that a characteristic feature of damage is edge delamination of the specimen. Combining this result with those obtained from monotonic tests in compression, it is reasonable to conclude that edge delamination of the specimen is a major damage process which is responsible in good part (but not necessarily totally) for the cyclic creep deformation and strain bursts observed during cyclic compression loading. However, it should be pointed out that while the results gathered so far are extremely interesting, the study must be considered far from complete because of the limited number of samples and stresses used, and the great complexity of the phenomena.

Conclusions

From tests on C/SiC cross-weave composite carried out under cyclic loading both in pulsating-tension and pulsating-compression, we offer the following conclusions:

(1) Tensile cyclic creep behavior, which seems to be frequency-dependent, was observed when notched specimens were tested in pulsating-tension. Repeated loading in such specimens induced surface cracks and spalling. Repeated loading on a smooth specimen gave much less creep strain and fewer surface cracks and spalling than observed in the notched sample; this behavior is attributed to the fewer pre-cycling imperfections in the smooth specimen.

(2) Compression-compression cyclic loading also caused a significant creep behavior and a strain burst phenomenon was observed. Edge delaminations which were observed in samples during repeated loading are taken to be mainly responsible for the compressive cyclic creep behavior.

(3) The mechanisms of failure by cyclic loading appear to be similar to those of monotonic loading but tend to occur more gradually and perhaps on a somewhat more localized level, although it is possible that the specimen design forced this conclusion.

(4) Fatigue or repeated loading will cause cumulative damage and, therefore, will degrade the inelastic properties of the ceramic composite materials. Obviously, if ceramic matrix composites are considered to be materials for safety-critical structural applications, evaluation of the materials with respect to cyclic loading will become absolutely essential.

MATERIAL FAILURE MODEL

FAILURE SCENARIO

The implications of the observed failure surface for the failure process of the material have been discussed above in the experimental section. The failure surface is reminiscent of the one observed in tensile failure of unidirectional glass/epoxy specimens. For such materials the failure surface is irregular and exhibits protruding broken single fibers. The present material failure surface is also irregular with protruding **groups** of fibers, Figure 31. The number of fibers in a group is typically between 5-9.

This indicates a failure mechanism which consists of accumulation of damage in the form of characteristic cracks which coalesce to produce catastrophic failure. The scenario is as follows:

a) Some flaw in the matrix is the source of a transverse crack which becomes unstable and propagates along its plane, normal to the fibers. This is in accordance with the transverse crack analysis in the section on Local Failure above which demonstrates the instability of such cracks. The propagating crack either ruptures or bridges fibers. In the first event, a transverse crack through fibers and matrix is formed but it will be ultimately arrested by the large matrix voids, longitudinal cracks or other regions of weakness in the matrix and fiber/matrix interface which it encounters. The larger the crack the more voids it is likely to encounter. If the crack does NOT rupture the fibers which it encounters, then these fibers will bridge the crack. But since the matrix in this kind of composite carries a large share of the load, the bridging fibers are subjected to a large increase in load. If one or more of them ruptures, the remaining bridging fibers are subjected to still further load increase until all bridging fibers rupture. The transverse crack thus formed is again arrested by longitudinal defects. Thus in both cases, the end result is the same: a unidirectional composite containing an accumulation of transverse cracks, roughly penny shaped, traversing fibers and matrix.

(b) Increase in axial tensile load will result in propagation of such cracks longitudinally in fiber direction thus forming cylindrical crack surfaces. It will be shown, further below, that these cylindrical cracks will become stable and arrested after they have propagated for sufficient distance. At this stage, the composite has a random accumulation of "penny shaped" cracks from which extend cylindrical cracks in fiber directions, Figure 45. In what follows, such cracks will be called H shaped cracks (HSC).

(c) Catastrophic failure occurs when such flaws interact and coalesce resulting in a jagged failure surface with protruding groups of fibers.

A schematic illustration of this failure scenario is shown in Figure 46. It is pointed out that it is entirely different from the failure process in unidirectional ceramics with glassy matrix. In that case local failure consists of a bridging crack which cracks the matrix on a plane transverse to the fibers, leaving the fibers intact. Such cracks occur at random places along the axis of the specimen and the specimen ultimately fails by fiber rupture on one of the bridging cracks.

ANALYSIS OF FAILURE SCENARIO

<u>Analysis of H-shaped Crack Stability</u>

A crucial aspect of the failure scenario proposed above is the stability of the HSC, Figure 45. We shall investigate this question on the basis of two models. In the first the composite is again modeled as an hexagonal array of identical circular fibers and it is assumed that the circular basis of any HSC extends over 7 fibers, one central fiber and 6 surrounding it, Figure 47. This is the only reasonable representation which is compatible with the hexagonal geometry since it has been experimentally found that the number of broken fibers in a group is 5-9. The HSC are assumed to be arranged in hexagonal patterns in transverse planes. A typical such plane is shown in Figure 47. The hexagonal geometry permits the definition of a triangular repeating element of the cracked composite, which is also shown in Figure 47. The finite element configuration for the repeating 3-D element is shown in Figure 48.

The matrix has been chosen as isotropic SiC and the fibers as transversely isotropic P100 carbon. Fiber volume fraction was assumed 40%. The model has been subjected to macroscopic uniform straining in fiber direction. This implies that the displacement on one cracked plane can be taken as zero while the displacement on the opposite cracked plane is constant. The boundary conditions on the planes bounding the triangle are found by symmetry considerations. A 3-D finite element analysis has been employed to compute the energy release rates of mode II, G_{II}, on the circular extremities of the cylindrical portions of the HSC, for various axial lengths, L_c. The computed maximum and minimum values along the crack peripheries are plotted in Figure 49. The results reveal that the axial cylindrical cracks are stable and get arrested after travelling a sufficient distance.

A much more simplified axisymmetric model for a composite containing HSC has also been considered. In this modeling fiber and matrix are not recognized and the HSC is assumed to be embedded in a representative cylinder which is homogeneous elastic and transversely isotropic and has the effective properties of the unidirectional composite. Stability of the crack in this problem has been investigated by axisymmetric finite element analysis. This analysis is significantly simpler and shorter than the one required for the previous model. Yet the results given in Figure 49 show that the G_{II} value obtained for the axisymmetric problem closely agree with the circumferential average values of the GII for the circular crack periphery of the hexagonal model. We have repeated this analysis for the case when frictional resistance is assumed along the cylindrical crack surfaces, Figure 50. Not surprisingly it has been found that friction significantly contributes to crack stabilization.

The results of the analysis support a fundamental premise of our failure scenario: the HSC stabilize in fiber direction.

It is expected that the stabilized HSC will propagate again when the composite is subjected to further load increments. The possible directions of the crack extension may be seen from the plots of the stress distributions in the representative cylinder containing a HSC. Shown in Figure 51 is the axial shear stress distributing along the axial direction at various radial locations, while Figure 52 shows the axial normal stress along the radial direction at different axial locations. Stress concentrations are observed for both the shear and normal stresses at the tip of the HSC. This indicates that the HSC may extend in the longitudinal direction by the axial shear stress and/or in the radial direction by the axial normal stress, depending on the local strength around the crack tips.

To further characterize the extension of a HSC, the longitudinal crack tip of the HSC embedded in a representative axisymmetric cylinder was extended in the radial direction to form a small radial crack. Finite element analyses were then performed to compute the G_I value that relates to the crack branching in the radial direction. The possible direction of crack extension at various longitudinal crack lengths is then determined by the local critical values of G_I and G_{II}. Figure 53 shows an example of the plot of $(G_{II}/G_I)^{1/2}$ versus L_c/r_c. It is interesting to note that for a small crack length G_{II} value is much larger than the G_I value and, thus, the crack is more likely to extend in the longitudinal direction. However, the ratio G_{II}/G_I seems to saturate to about one as the longitudinal cracks extends more than $3r_c$. The results also indicate that for a relatively weak critical value of G_{II} the crack can readily extend in the axial direction and results in long fiber-bundle pull out, while for a strong critical G_{II} failure with short fiber bundles is more likely. Finally, the extension and connection of such HSCs results in a jagged failure surface as that shown in Figure 46.

Stiffness Degradation

It is now our purpose to evaluate the effect of HSC accumulation on the stiffness of the fiber composite. This is important for two reasons: first, the stiffness in itself is an important engineering property and second, it can be measured without much difficulty. Therefore an accurate computational procedure which relates stiffness to HSC density will serve to determine the latter experimentally by measuring the former.

The mathematical basis for evaluation of the effective stiffness are some general results for the effective elastic properties of cracked bodies. It is recalled that in order to evaluate the effective elastic properties of a composite it is subjected to either one of the so-called homogeneous boundary conditions

$$u_i\ (S) = \epsilon^o_{ij}\, x_j \qquad (a)$$

$$T_i\ (S) = \sigma^o_{ij}\, n_i \qquad (b) \qquad (1)$$

where ϵ^o_{ij} and σ^o_{ij} are constant strain and stress, respectively; see e.g. [25]. When the composite is cracked the effective elastic moduli C^*_{ijkl} and the effective elastic compliances S^*_{ijkl} are defined by the relations

$$\bar{\sigma}_{ij} = C^*_{ijkl}\,\epsilon^o_{kl} \tag{2}$$

when (1a) is prescribed and by

$$\bar{\epsilon}_{ij} + \gamma_{ij} = S^*_{ijkl}\,\sigma^o_{kl} \tag{3}$$

when (1b) is prescribed.

Here overbars denote volume average and

$$\gamma_{ij} = \frac{1}{2V}\int_{S_c}\Big([u_i]\,n_j + [u_j]\,n_i\Big)\,dS \tag{4}$$

where

$[u_i]$ - displacement jumps across cracks (COD)
n_i - components of normal to crack surface
S_c - surface of all cracks
V - volume of composite

To evaluate the effective Young's modulus E^*_A for a distribution of HSC, we consider first the detailed hexagonal model, Figure 47. Applying a macroscopic strain ϵ^o in fiber direction we have

$$E^*_A = \bar{\sigma}_{11}/\epsilon^o \tag{5}$$

To evaluate the average stress $\bar{\sigma}_{11}$, we consider two planes of symmetry, transverse to the fibers, midway axially, between the cracked planes. Then $\bar{\sigma}_{11}$ is the stress average for such a plane. We have evaluated the reduction of E^*_A due to HSC distribution as a function of longitudinal crack length L_c. These results are shown in Figure 54.

Bearing in mind that the hexagonal model is complex and requires substantial computer resources, we have sought a simplified calculation procedure. To analyze a characteristic HSC, it may be imagined that the HSC is embedded in a circular cylinder, Figure 45, which is embedded in the effective material, Figure 55. At infinite distance uniform strain and stress are prescribed. This model is known as the generalized self consistent scheme (GSCS), see e.g., [26]. Its implementation in the present case is, however, very complex and, therefore, we have considered a still more simplified model. We consider a single circular cylindrical element containing an HSC, Figure 45. First we apply displacements to its boundary and evaluate the average stresses to obtain element stiffnesses. Second, we apply tractions to the faces and compute compliances. From inversion of the compliances we obtain stiffnesses. It may be shown that the first stiffnesses are larger than the second stiffnesses. If the two values are close, we take the average. The details of the implementation of this model are described in Appendix A.

Typical results for axial Young's modulus E_A^*, axial Poisson's ratio ν_A^*, transverse bulk modulus k^*, and the associated elastic constants of n^* and l^* are listed in Table 7(b) for the imposed displacement and traction boundary conditions, respectively. The results for E_A^* of the axisymmetric homogeneous cylinder, containing one HSC, are compared with the results for the hexagonal model. It is seen that the results for imposed displacements and tractions are upper and lower bounds, respectively, for the hexagonal array results. The bounds are quite close and their average provides good approximation.

The analysis for shear response is more complex because it turns out that there is partial closure of the crack in this case. This can be seen from Figure 56 which shows the deformation of the HSC when axial shear tractions are applied to the surface of the cracked cylinder. It is seen that parts of the crack surfaces overlap, which is a physical impossibility. This implies that part of the crack surfaces have come in contact during shear and this requires modification of the analysis. This can be done in terms of finite element procedures which employ contact elements. However, the analysis would be incremental nonlinear and, therefore, quite time consuming.

RESIDUAL EFFECTS UNDER CYCLIC LOAD

Ceramic composites are elastic-brittle materials. Our experience with such materials is that they do not exhibit residual strains due to a load cycle. In other words, when a ceramic specimen is loaded and unloaded to zero, we would expect the specimen average strain to disappear. Experiments show, however, that this is not the case. We have measured the specimen strains produced by cyclic load for the material employed in our experimental program. The results are shown in Figures 34, 41. It is seen that after loading, residual strains remain. When a number of load cycles are applied, the residual strain increases with every cycle and tends to attain a limit. This is demonstrated by the experimental results shown in Figure 41. This resembles the phenomenon of creep under cyclic load which is observed in metals. To the best of our knowledge no explanation of this phenomenon has been given in the literature.

To understand this phenomenon it is recalled that a ceramic composite is formed at high temperature, which is here taken as initial temperature T_0. It is assumed that at this stage the composite is stress free. Now let the composite be cooled down to room temperature T. As a result the composite develops stresses σ_{ij}^{T} and strains ϵ_{ij}^{T} and it may also develop damage in the form of cracks. Let this damage be denoted D^T. Then by definition the average strain $\bar{\epsilon}_{ij}^{T}$ is expressed in terms of the effective thermal expansion coefficient of the composite. Thus

$$\bar{\epsilon}_{ij}^{T} = \alpha_{ij}^{*}(T, D^{T})\ (T - T_0) \tag{6}$$

where α_{ij}^{*} is the secant temperature dependent effective TEC. See Figure 57 for definition of such a TEC. Note that if damage has been produced by cooldown, this affects the TEC. That cracking of a composite modifies its TEC significantly has been demonstrated in [27].

Next the composite is loaded by average stress $\bar{\sigma}_{ij}$. Let it be assumed that this load produces additional damage D^{σ}. This produces an additional average strain

$$\bar{\epsilon}_{ij}^{\sigma} = S_{ijkl}^{*} \left(T,\ D^{T} + D^{\sigma}\right) \bar{\sigma}_{kl} \tag{7}$$

where S_{ijkl}^{*} are the effective elastic compliances at temperature T for the damage produced by cooldown <u>and</u> loading and this is the strain which is measured during a test since the strain (6) was already present before the test. When $\bar{\sigma}_{ij}$ is unloaded, the strain (7) disappears, provided that the unloading does not modify the internal damage. However, because of the additional damage D^{σ} produced during loading, the initial residual stress σ_{ij}^{T} is now different since it has to satisfy new zero traction boundary conditions on the new crack surfaces formed during loading. It is in fact the same residual stress which would have been produced had the specimen developed damage $D^{T} + D^{\sigma}$ during cooldown. It follows that average strain which remains after unloading is

$$\bar{\epsilon}_{ij}^{Tu} = \alpha_{ij}^{*} \left(T,\ D^{T} + D^{\sigma}\right) \left(T - T_{0}\right) \tag{8}$$

Therefore, the residual strain observed after an unloading cycle is given by

$$\bar{\epsilon}_{ij}^{r} = \bar{\epsilon}_{ij}^{Tu} - \bar{\epsilon}_{ij}^{T} = \left[\alpha_{ij}^{*} \left(T,\ D^{T} + D^{\sigma}\right) - \alpha_{ij}^{*} \left(T, D^{T}\right)\right] \left(T - T_{0}\right) \tag{9}$$

This demonstrates that the residual stresses and strains formed in a composite during cooldown and the damage produced during loading are the reason for the phenomenon of macroscopic residual strain observed during load cycles.

It is easily understood that the present derivation is not limited to one load cycle but applies equally to any number of load cycles, if D^{σ} is interpreted as the damage produced by all of these load cycles.

Furthermore, it is known that effective TEC attain limiting values with crack saturation, [27]. Thus, if D^{σ} is the damage at crack saturation, this implies that further load cycles will not produce additional cracks, therefore, the TEC $\alpha^*_{ij}\ (T,\ D^T + D^{\sigma})$ remains unchanged and, therefore, the residual strain (9) does not increase with further load cycles. This explains the observed phenomenon of the residual strain attaining a limit.

As a simple example, consider a one-dimensional, Figure 58, model of a unidirectional fiber composite consisting of isotropic matrix and fibers where $\alpha_m > \alpha_f$. Assume that cooldown produces no damage. Then the effective TEC in fiber direction α^* is given with good approximation by

$$\alpha^*\ (T,\ D^T) = \alpha^*\ (T,\ 0) \cong \frac{E_m \alpha_m v_m + E_f \alpha_f v_f}{E_m v_m + E_f v_f} \tag{10}$$

where v_m, v_f are the volume fractions.

The composite is now loaded by tensile average stress $\bar{\sigma}$ in fiber direction. This produces tensile stress in matrix which is superposed on the tensile matrix stress produced by cooldown (since, by hypothesis, $\alpha_m > \alpha_f$). Assume that the specimen is loaded to the point of matrix crack saturation. This matrix crack accumulation is the damage D^{σ}. The matrix becomes ineffective and, therefore, the effective TEC becomes equal to fiber TEC. Thus,

$$\alpha^* \ (T, \ D^T + D^\sigma) = \alpha^* \ (T, \ D^\sigma) = \alpha_f \tag{11}$$

It follows from (9-11) that

$$\overline{\epsilon}^r = \frac{(\alpha_f - \alpha_m) \ E_m \, V_m}{E_m \, V_m + E_f \, V_f} \ (T - T_0) \tag{12}$$

Since $T < T_0$ (cooldown) and $\alpha_f < \alpha_m$ this is a positive residual strain.

CONCLUSION

In this work we have been concerned with analytical and experimental investigation of thermomechanical properties and failure mechanisms in unidirectional ceramic composites in which the ceramic matrix is flawed or variable. Preliminary numerical fracture mechanics studies have been conducted for perfect brittle matrix in order to assess the criticality of various kinds of cracks. It was found that transverse cracks tend to grow in unstable fashion through the matrix while axial cracks, in fiber direction, tend to stabilize as their length increases. The unstable growth of transverse cracks is in accordance with the bridging cracks observed for homogeneous glassy ceramic matrices, which traverse the specimen. In flawed matrix, however, transverse cracks are arrested by the flaws.

The experimental investigation has shown that stress-strain relations in tension are significantly nonlinear, this effect being due to crack accumulation and growth during loading. Examination of failure surfaces for tensile static load has revealed jaggedness and irregularity. In particular, fibers fracture in bundles consisting of 5-9 fibers. This is attributed to matrix variability and has led us to propose a failure scenario which is characteristic of composites with variable ceramic matrix. According to this scenario transverse cracks get arrested and then grow axially to form so-called H shaped cracks (HSC). Damage accumulates in the form of HSC which ultimately merge to result in failure. We have also analyzed stiffness reduction due to HSC formation.

Cyclic loading experiments performed have revealed the phenomenon of residual macro-strain formation after each cycle, in spite of the fact that the material is elastic brittle. We have given a theoretical explanation of this effect on the basis of the residual thermal stress state which is present in all ceramic composites because of the cooldown from manufacturing temperature.

Our study of ceramic composites which contain imperfections have identified several important local damage mechanisms. These local damages produce several important effects. They result in changes in the thermo-mechanical properties of composites subjected to applied loads and temperatures. The damages grow in size and number leading to material failure. In a similar fashion, the damages also influence lifetime under cyclic load and cyclic temperature conditions. Further research to quantify these effects will provide the capability to design and use ceramic matrix composite materials in practical applications.

REFERENCES

1. Budiansky, B., Hutchison, J.W., and Evans, A.C., "Matrix Fracture in Fiber-Reinforced Ceramics", Journal of Mechanics and Physics of Solids, Vol. 34, No. 2, pp. 167-189, 1986.
2. Aveston, J., Cooper, G.A., and Kelly, A., The Properties of Fiber Composites, pp. 15-26, Conference Proceedings, National Physical Laboratory, Guildford, IPC Science and Technology, Press Ltd., 1971.
3. Marshall, D.B., Cox, B.N., and Evans, A.G., 1985, "The Mechanics of Matrix Cracking in Brittle Matrix Fiber Composites", Acta Metallurgica, Vol. 33, No. 11, pp. 2013-2021.
4. McCartney, L.N., Proc. Royal Society, A409 (1987), pp. 329-350.
5. Prewo, K.M., Brennan, J.J., and Layden, G.K., "Fiber Reinforced Glasses and Glass-Ceramics for Performance Applications", Ceramic Bulletin, Vol. 65, No. 2, 1986, pp. 305-313.
6. Tredway, W.K. and Prewo, K.M., "Carbon Fiber Reinforced Glass Matrix Composites for Structural Space Based Applications", Final Report for ONR, Contract No. N00014-85-C-0332, July 31, 1989.
7. Brennan, J.J. and Prewo, K.M., "Silicon Carbide Reinforced Glass-Ceramic Matrix Composites Exhibiting High Strength and Toughness", J. of Material Sciences, Vol. 17, 1982, pp. 2371-2383.
8. Jarmon, D.C. and Prewo, K.M., "Characterization of SiC Monofilament Reinforced Glass and Glass-Ceramic Composites", UTRC Final Report for ONR, Contract No.N000148-81-C-0571, Nov. 15, 1986.
9. Prewo, K.M., "Carbon Fiber Reinforced Glass Matrix Composite Tension and Flexure Properties", J. of Material Sciences, Vol. 23, 1988, pp. 2745-2752.
10. Starrett, H.S., Southern Research Institute, Communicated Data, 1985.
11. Kohnke, P, "ANSYS Engineering Analysis System Theoretical Manual", Swanson Analysis System, Inc., 1987.

12. "ABAQUS, Theory Manual", Hibbitt, Karlsson & Sorensen, Inc., 1990
13. Hashin, Z., "The Differential Scheme and Its Application to Cracked Materials", J. Mech. Phys. Solids, Vol. 36, 1988, pp. 719-734.
14. Marshall, D.B. and Evans, A.G., J. Am. Ceram. Soc. 68 (9185) 225.
15. Mah, T, Mendiratta, M.G., Katz, H.P., Ruh, R., and Mazdiyasni, K.S., J. Am. Ceram. Soc., 68 (1985) C27-C30.
16. Shaizero, O. and Evans, A.G., J. Am. Ceram. Soc., 69 (1986) 481.
17. Hull, D., "An Introduction to Composite Materials", Chapter 7, Cambridge University Press, 1981.
18. Ritchie, R.O., Mater. Sci.Engng., 103A (1988), 15.
19. Evans, A.G., International J. Fracture, 16 (1980), 485.
20. Evans, A.G., Widerhorn, S.M., Liner, M., and Fuller, E.R., Bulletin Am. Ceram. Soc., 54 (1975), 576.
21. Ewart, L. and Suresh, S., J. Mater. Sci. Letters, 5 (1986), 774.
22. Neumann, P, Acta Metall., 17 (1969), 1219.
23. Lorenzo, F. and Laird, C., Acta Metall., 32 (1984), 671.
24. Hong, S.I. and Laird, C., to be published.
25. Hashin, Z., "Theory of Fiber Reinforced Materials", NASA CR 1974, 1972.
26. Christensen, R.M., Mechanics of Composite Materials, Wiley-Interscience, New York; 1979.
27. Hashin, Z., "Thermal Expansion Coefficients of Cracked Laminates", Composites Sciences & Technology, 31, 247-260, (1988).

TABLE 1. CONSTITUENT PROPERTIES

MATERIAL	E_a, E_t Msi	ν_a, ν_t –	G_a Msi	α_a, α_t 10^{-6}/°F	ρ pci
SiC–1*	66.0	0.2	27.5	2.4	0.115
SiC–2**	37.0	0.2	15.4	2.4	0.086
NICALON FIBER	29.0	0.2	12.1	1.72	0.092
SiC MONOFILAMENT	62.0	0.25	24.8	2.7	0.12
P100 FIBER	112.0, 1.0	0.25, 0.73	3.2	−0.82, 6.7	0.076

* MONOLITHIC SiC MATRIX

** MONOLITHIC SiC MATRIX WITH 25% VOIDS

TABLE 2. ENERGY RELEASE RATES FOR AN IN-PLANE MATRIX CRACK PERPENDICULAR TO FIBERS WITHOUT FIBER CRACKING AND DEBONDING, NICALON/SiC-1, $a/r_f = 0.35$, $V_f = 40\%$.

CRACK PERIPHERY	NODAL POINTS	$\frac{\sqrt{G_I}}{\sigma_c}$, $10^{-6}\ lb^{-\frac{1}{2}} in^{-\frac{3}{2}}$ *
$r_f + a$	1	70.9
	2	70.8
	3	70.9
	4	70.8
	5	70.8
	6	70.7
	7	70.7
r_f	8	65.3
	9	65.3
	10	65.3
	11	65.3

* G_I ENERGY RELEASE RATE OF MODE 1 CRACKING

σ_c: EFFECTIVE COMPOSITE APPLIED STRESS

TABLE 3. ENERGY RELEASE RATES FOR IN-PLANE MATRIX CRACKS WITHOUT FIBER CRACKING AND DEBONDING, NICALON/SiC-1.

a/r_f	$\frac{\sqrt{G_I}}{\sigma_c}$, $10^{-6}\ lb^{-\frac{1}{2}} in^{-\frac{3}{2}}$ *	
	SIDE A	SIDE B
0.35	70.7	70.9
0.7	94.5	94.9
1.0	125.8	107.9
1.2	--	125.2
1.66	--	122.4

* FOR MODE 1 CRACKING ON CRACK PERIPHERIES $r_f + a$

TABLE 4. ENERGY RELEASE RATES FOR AN IN-PLANE CIRCULAR MATRIX CRACK PERPENDICULAR TO FIBERS, NICALON/SiC-1, $a/r_f = 0.5$ $V_f = 40\%$

NODAL POINT ON CRACK PERIPHERY $r = a$	$\frac{\sqrt{G_I}}{\sigma_c}$, $10^{-6}\ lb^{-\frac{1}{2}} in^{-\frac{3}{2}}$
1	72.8
2	72.6
3	72.6
4	72.6
5	72.5
6	72.7
7	72.3
8	72.0
9	71.9
10	71.9

TABLE 5. ENERGY RELEASE RATES FOR RING MATRIX CRACKS WITH INTERPHASES WITHOUT FIBER CRACKING AND DEBONDING, SiC/SiC-2, V_f = 40%

case	a/r_f	$\frac{\sqrt{G_I}}{\sigma_c}$, $10^{-6}\ lb^{-\frac{1}{2}} in^{-\frac{3}{2}}$			
		CRACK PERIPHERY r_f		CRACK PERIPHERY $r_f + a$	
		SIDE A**	SIDE B**	SIDE A	SIDE B
$E_i = E_m$	0.35	60.6	60.6	50.4	50.4
	0.94	97.5	97.4	78.8	78.6
	1.6	112.7	113.3	109.6*	80.3
$E_i = 0.1E_m$	0.35	48.2	48.2	56.0	56.0
	0.94	77.7	77.8	87.1	93.1
	1.6	93.3	93.5	89.4*	93.3

* FIBER CRACKS

** GEOMETRIC CONFIGURATION SEE FIGURE

TABLE 6. ENERGY RELEASE RATES FOR MATRIX CRACKS WITH FIBER DEBONDING, NICALON/SiC−1, V_f = 40%

a/r_f	b/r_f*	$\frac{\sqrt{G_I}}{\sigma_c}$, $10^{-6}\ lb^{-\frac{1}{2}} in^{-\frac{3}{2}}$	
		IN−PLANE CRACK $r = a + r_f,\ z = 0$	DEBONDING CRACK $r = r_f,\ z = b$
0.35	0.00	70.7 (I)	65.3 (I)**
0.35	0.18	74.0 (I)	27.2 (II)
0.35	0.42	81.3 (I)	17.6 (II)
0.70	0.00	94.5 (I)	116.8 (I)
0.70	0.18	99.8 (I)	43.4 (II)

* r_f = 0.3321 d

** ( ): FRACTURE MODE

Table 7a. Elastic Constants For Homogeneous Uncracked P100/SiC, V_f = 40%

E_A Msi	E_T Msi	ν_A	ν_T	G_A
84.66	19.47	0.173	0.439	14.63

Table 7b. Computed Effective Constants For A Representative Cylinder With H-Crack

Imposed Homogeneous Boundary Conditions	n^* Msi	I^* Msi	k^* Msi	E_A^* Msi	ν_A^*
Displacements	68.69	1.97	6.99	68.13	0.141
Tractions	62.98	1.89	7.06	62.48	0.134

Note: r_c/r_f = 4.11, L/r_f = 8.23, R/r_f = 7.82, L_c/r_f = 2.06

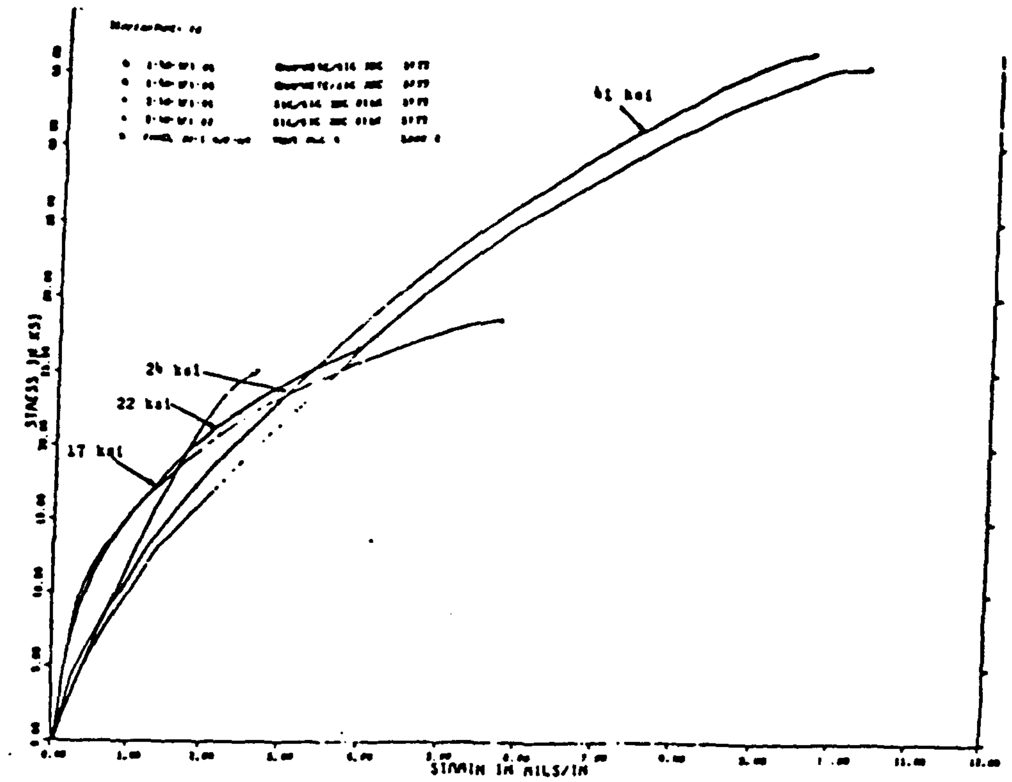

Figure 1. Tensile Stress-Strain Curves at 70°F for the SEP Nicalon-SiC and Graphite-SiC Composites

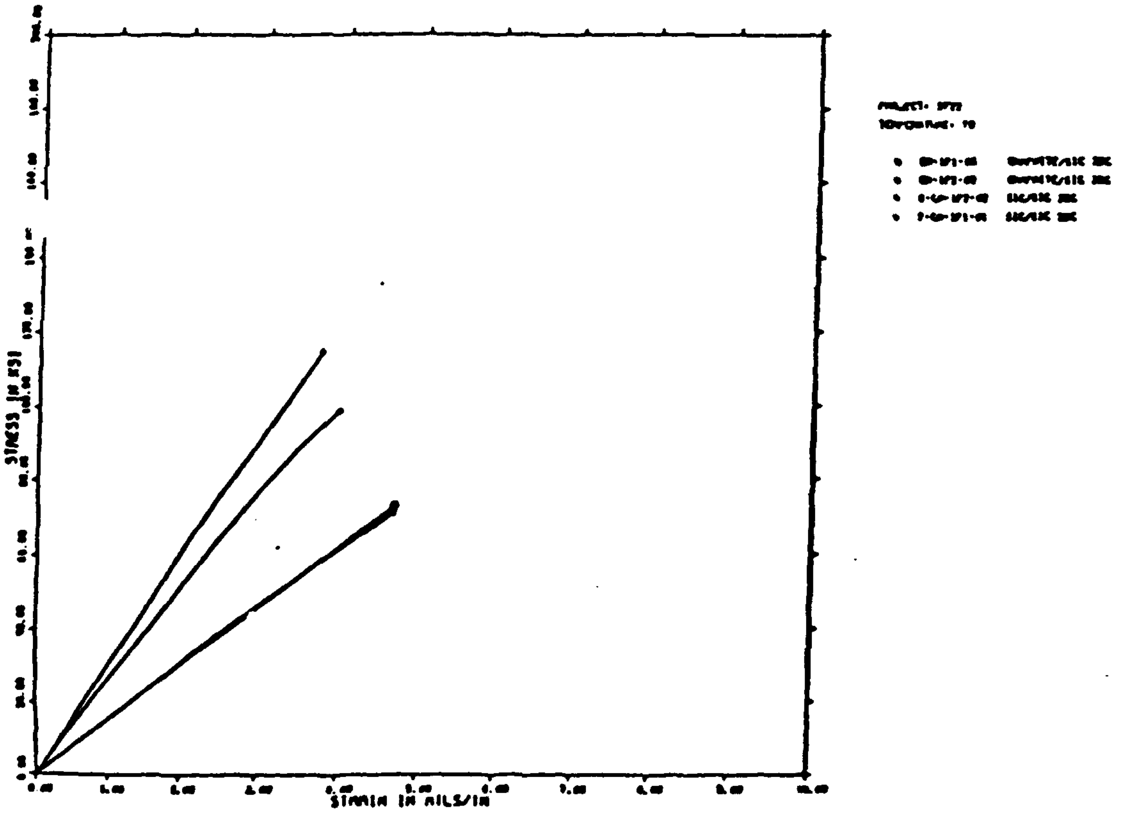

Figure 2. Compressive Stress-Strain Curves at 70°F for the SEP Nicalon-SiC and Graphite-SiC Composites

Figure 3. Photomicrograph of SEP Nicalon/SiC Composite

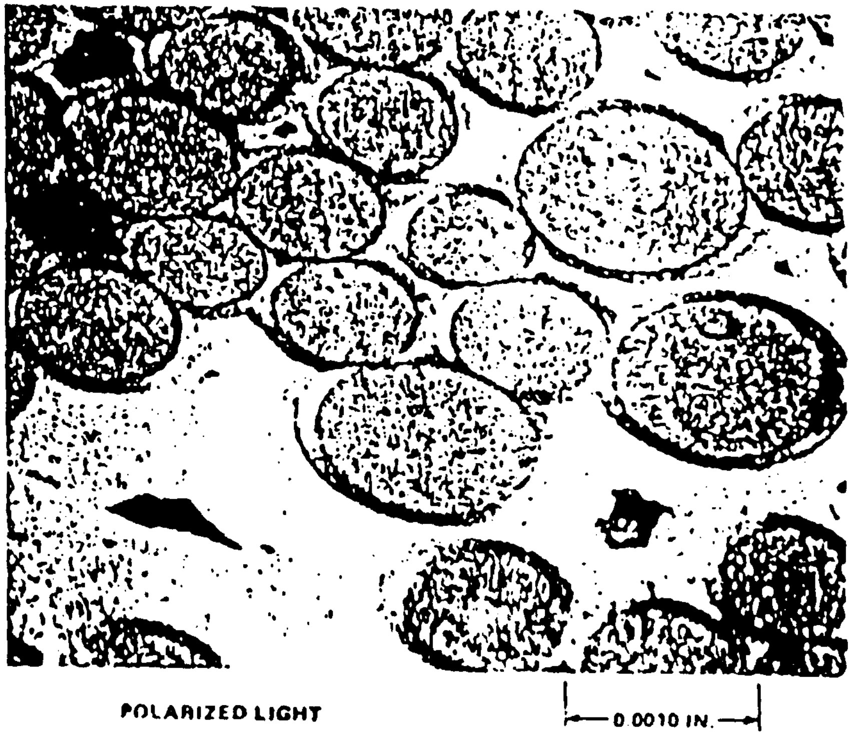

Figure 4. Nicalon filaments in CVD SiC Matrix, SEP Nicalon/SiC Composite

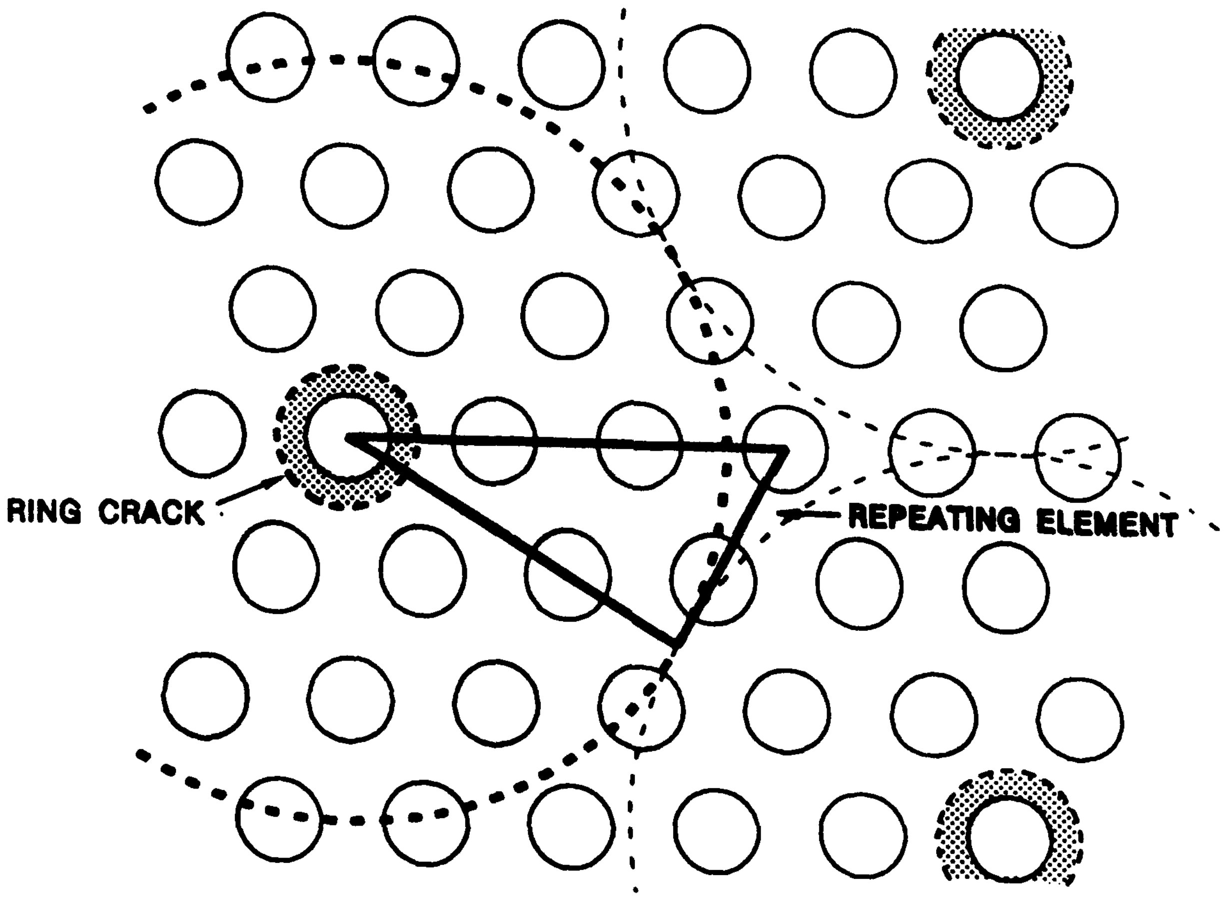

Figure 5. Model for repeating matrix crack in a hexagonal array of circular fibers.

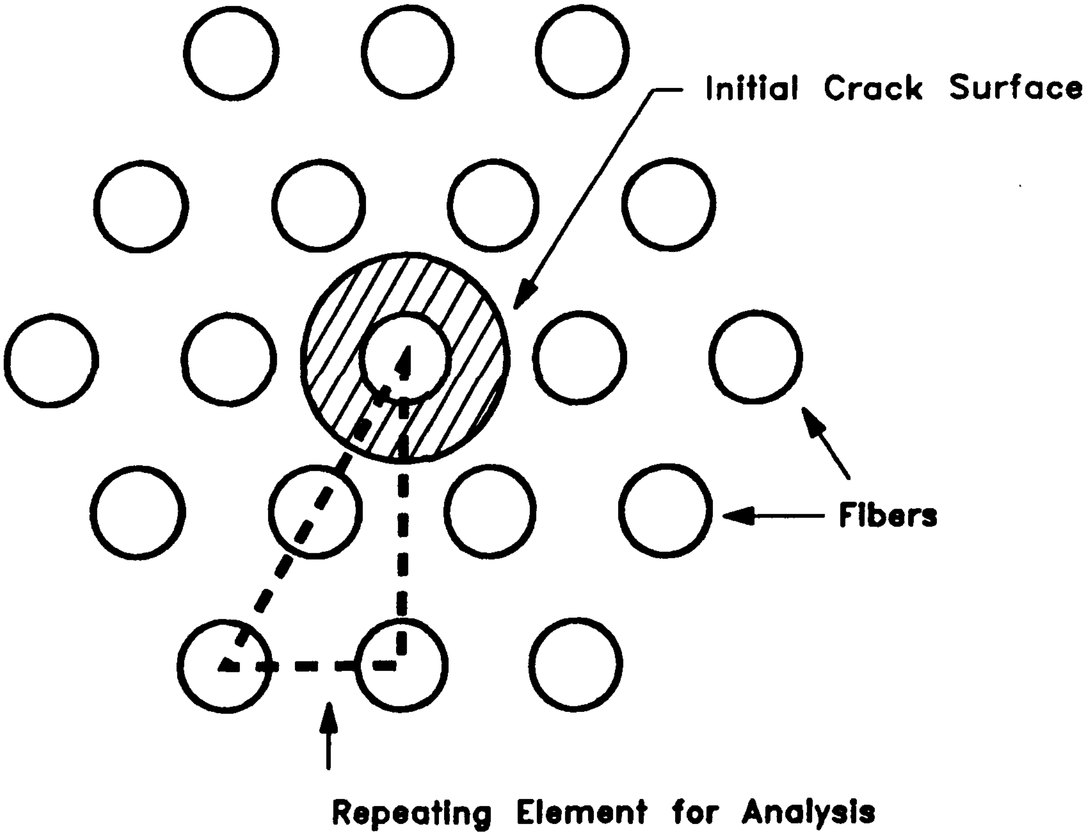

Figure 6. Model for Crack Stress Analysis.

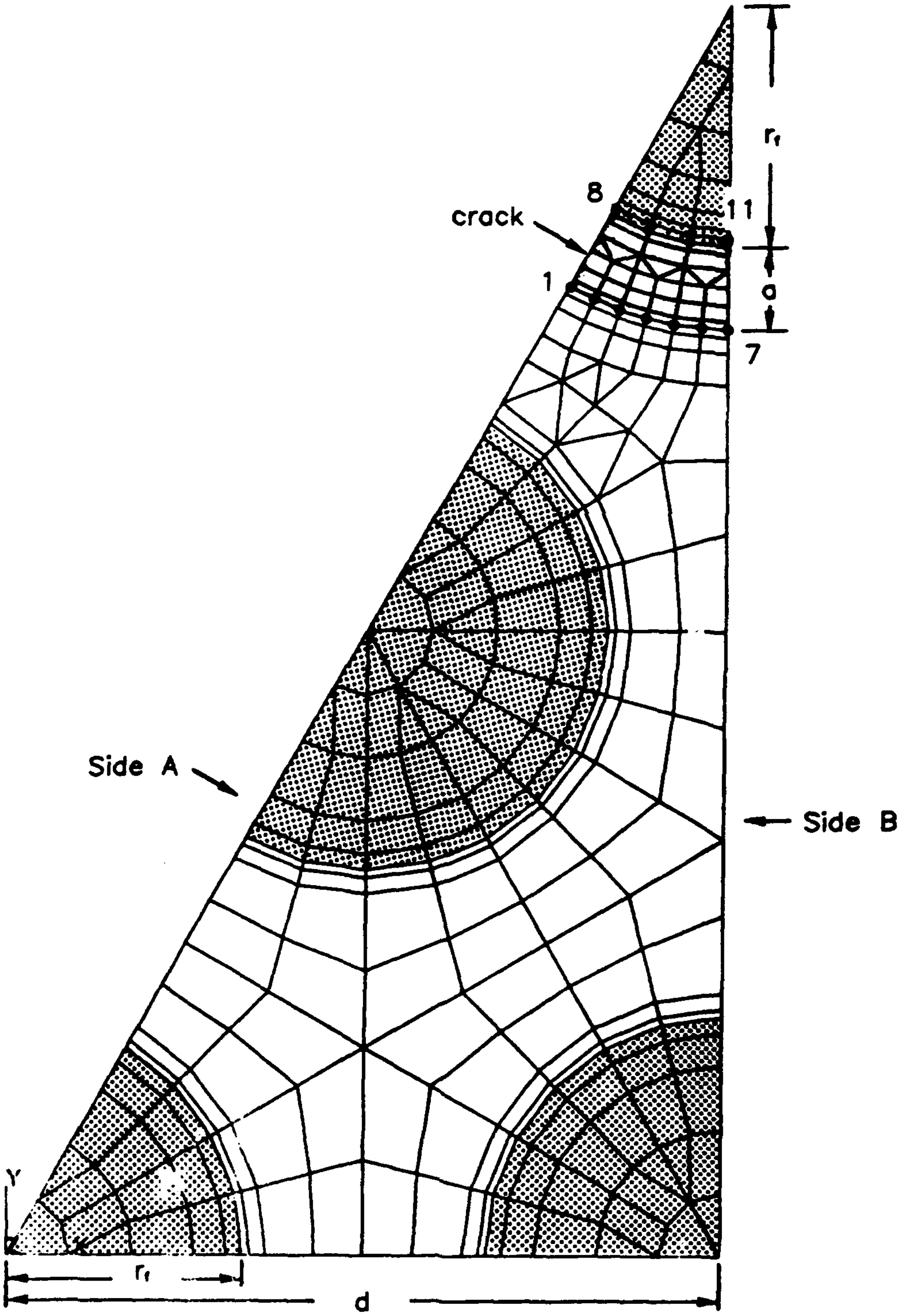

Figure 7. Finite element model for a repeating triangular element including an in-plane matrix crack.

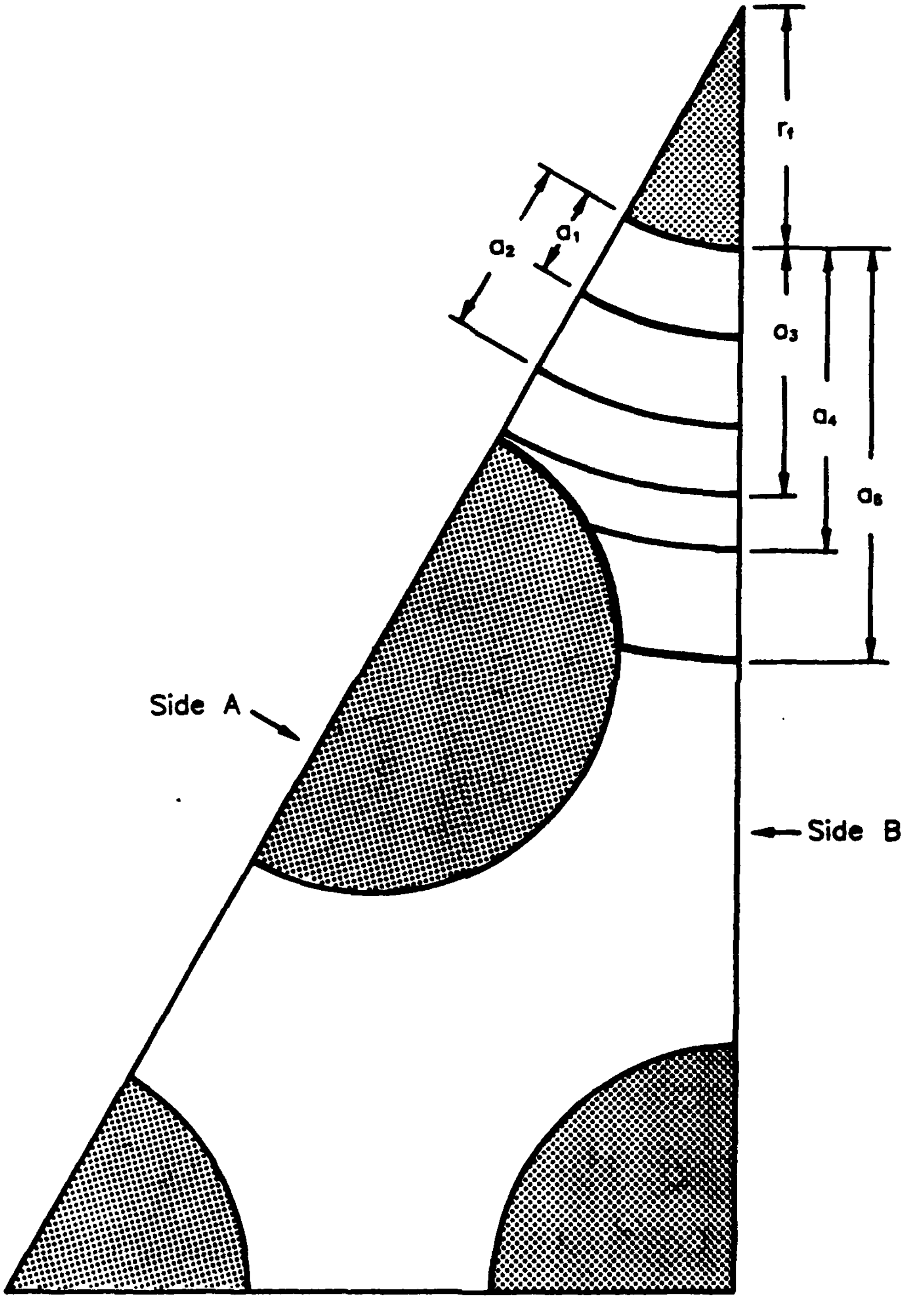

Figure 8. In–Plane matrix cracks without fiber cracking and debonding.

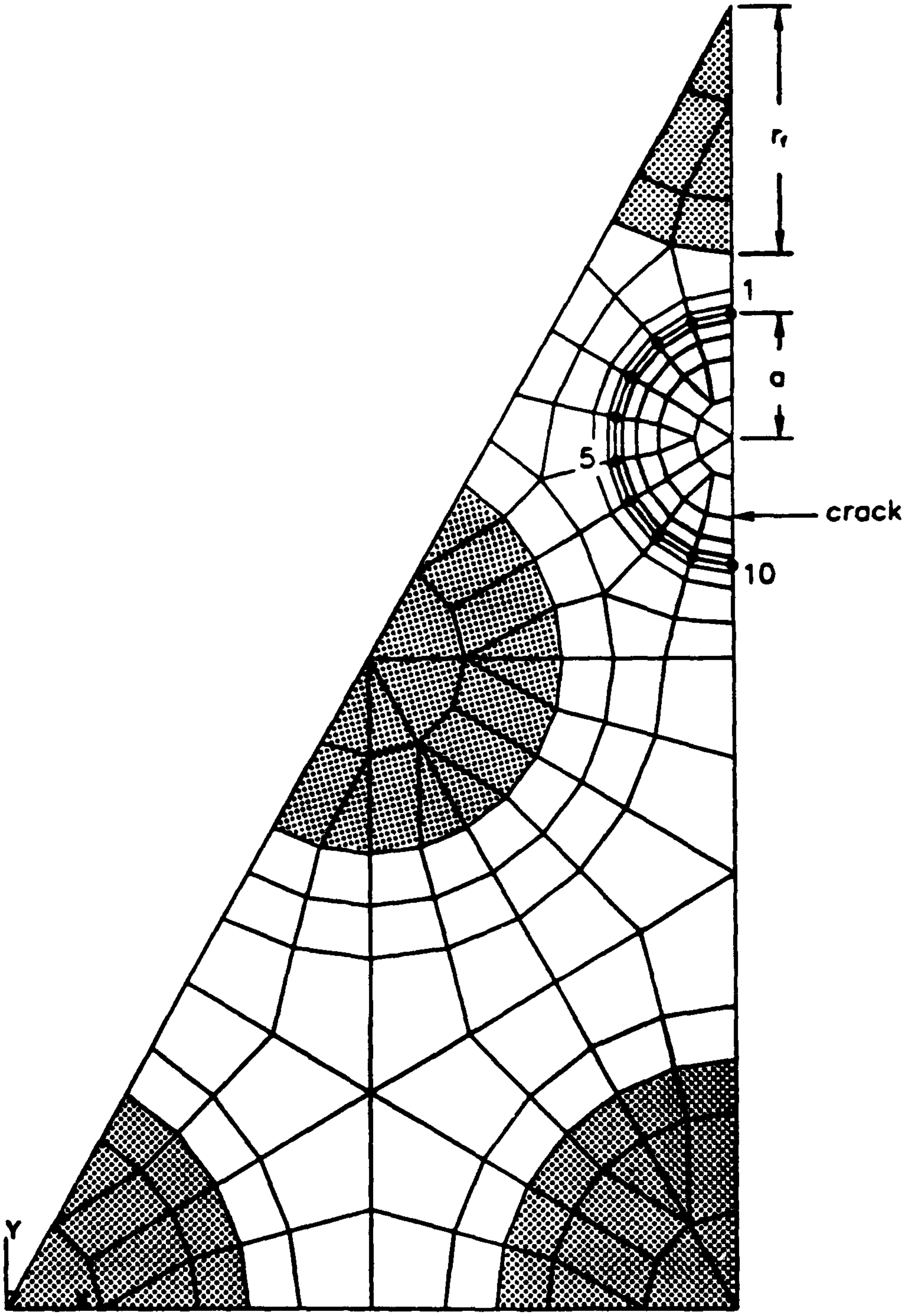

Figure 9. Finite element model for a repeating element of a unidirectional composite with dispersed circular matrix cracks perpendicular to fibers.

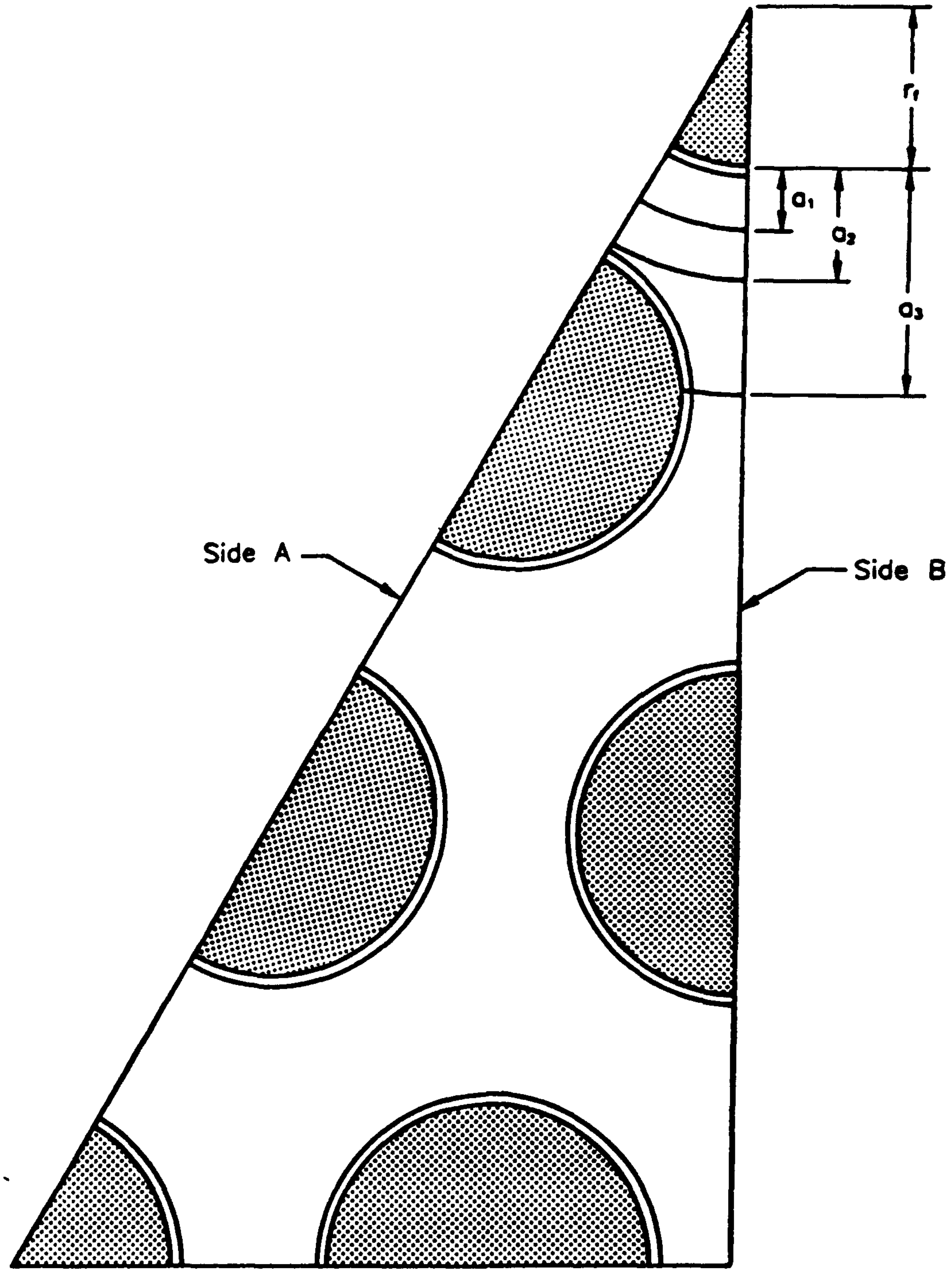

Figure 10. In–Plane matrix crack with interphases between fibers and matrix without fiber cracking and debonding.

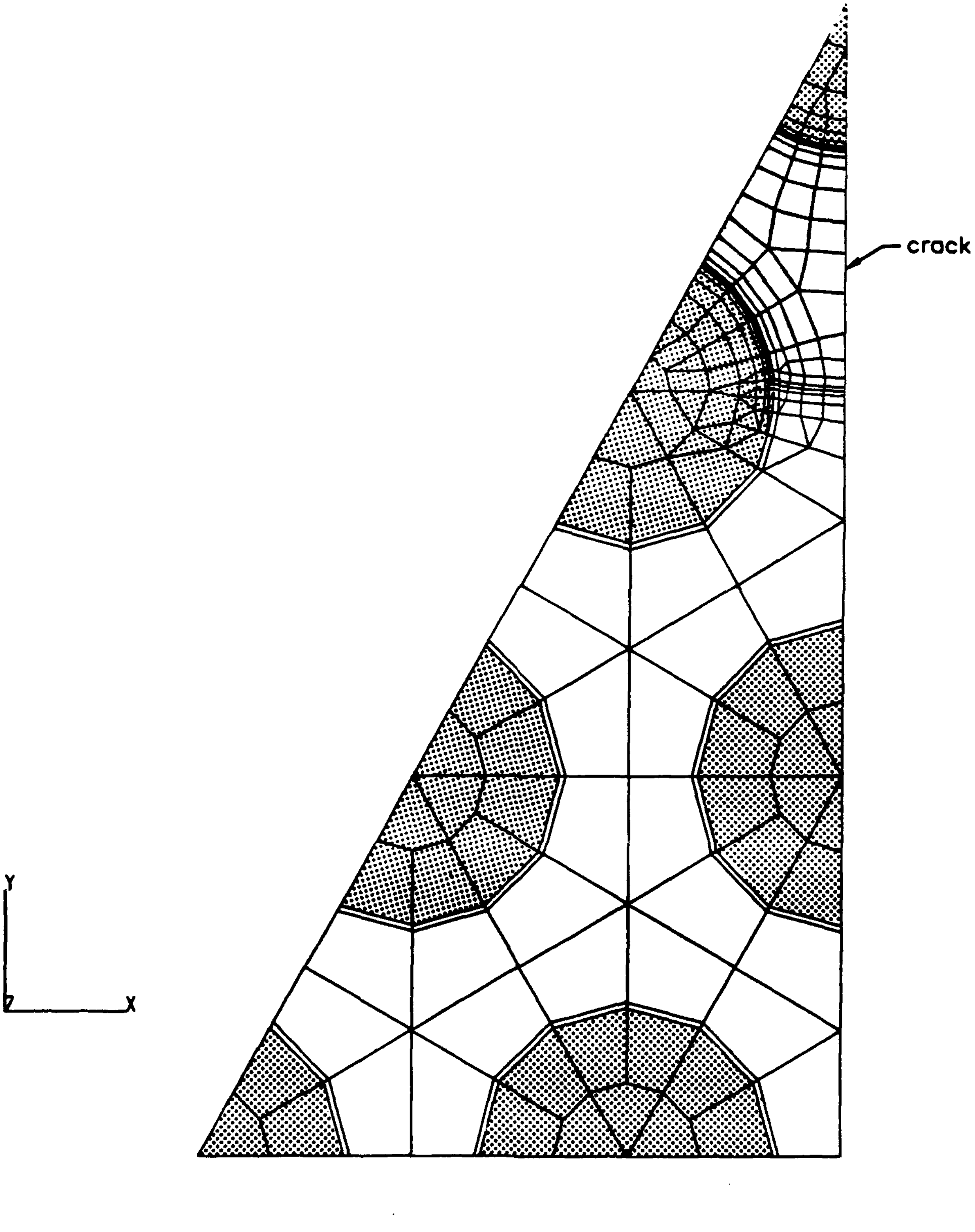

Figure 11. Finite element model for an in-plane matrix crack with length a_3.

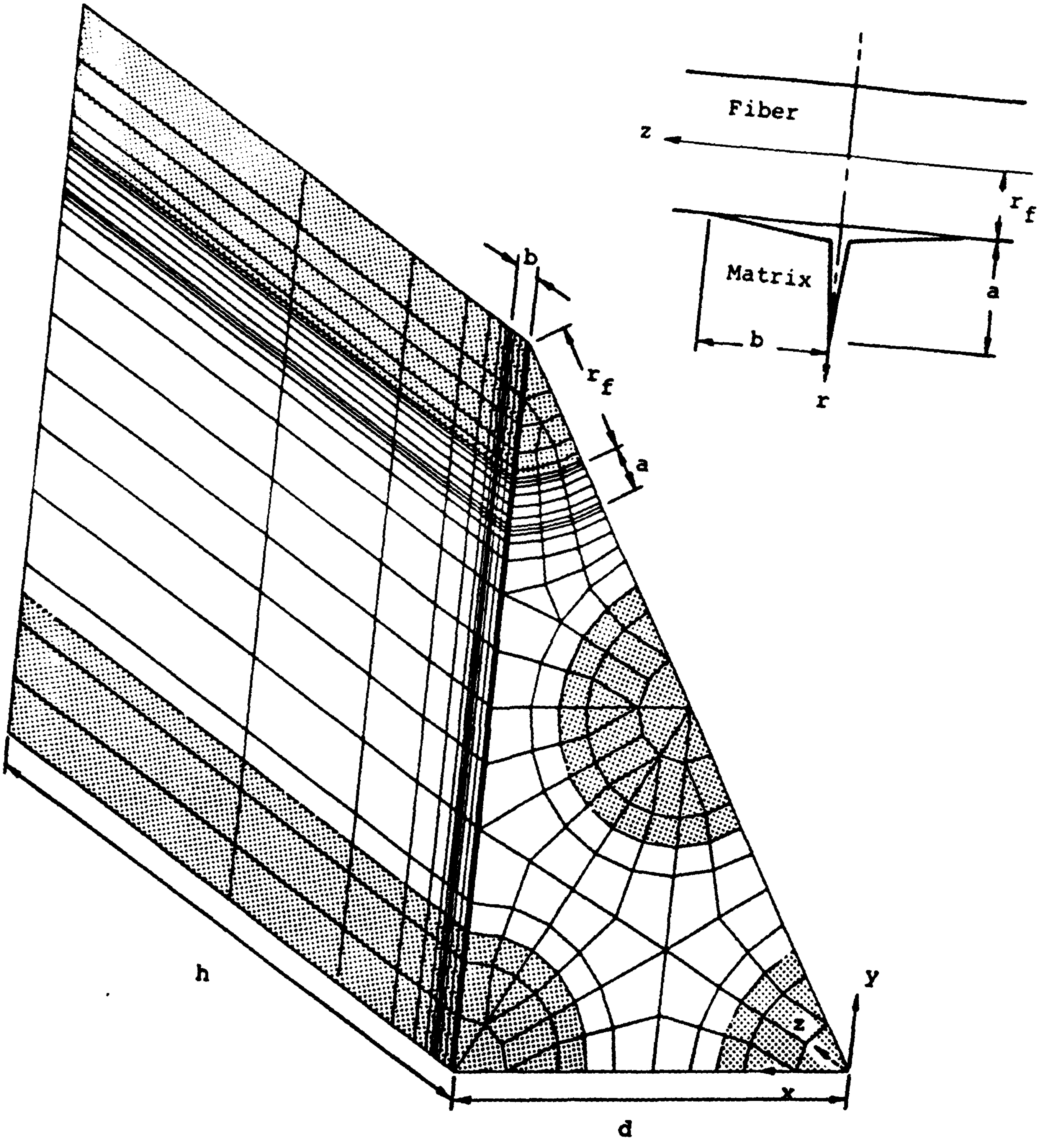

Figure 12. Finite Element Model for Combined In-Plane Matrix Crack and Fiber/Matrix Debonding Crack

Figure 13. As-Received Carbon SiC Cross-Weave Composite

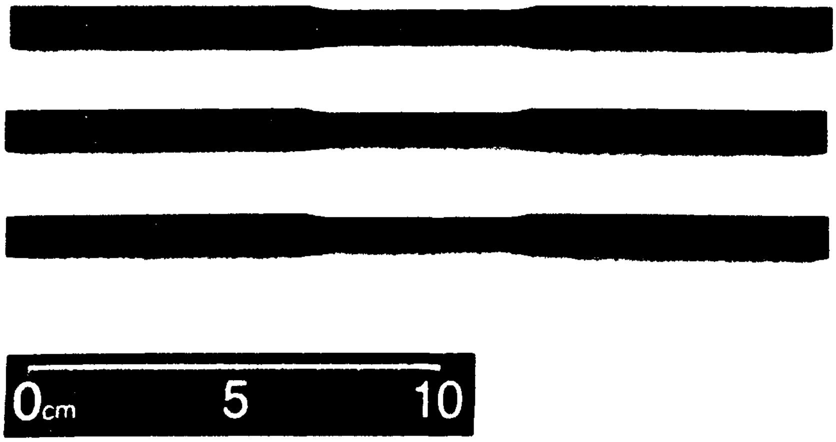

Figure 14. As-Received Carbon/SiC Cross-Weave Composite Specimens

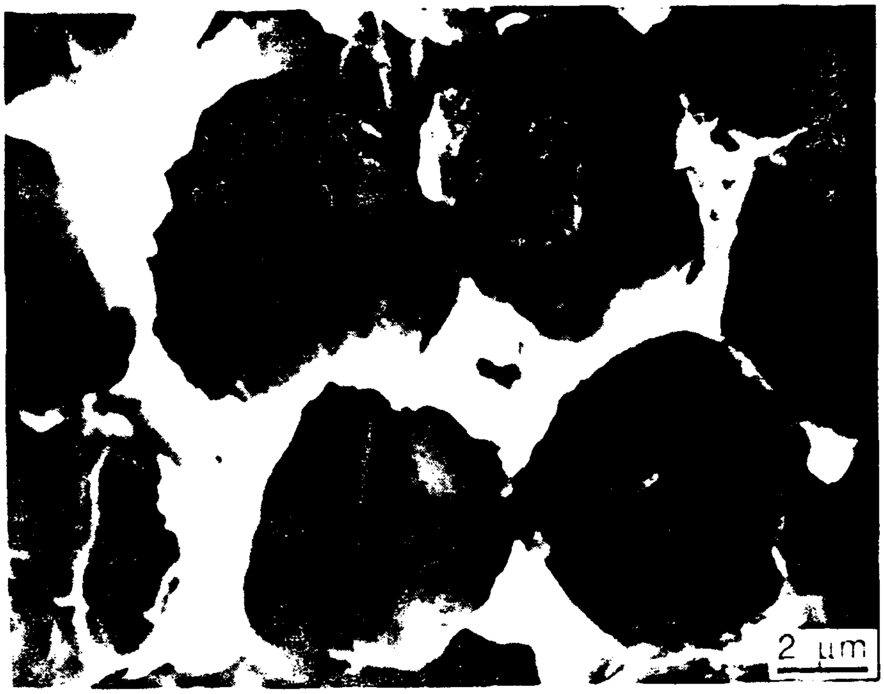

Figure 15. Cross-Section Through Carbon Fiber Bundle of C/SiC Composite, Showing Deviation From Close Packing and Inhomogeneously Distributed SiC Matrix. Sectioned by Diamond Saw.

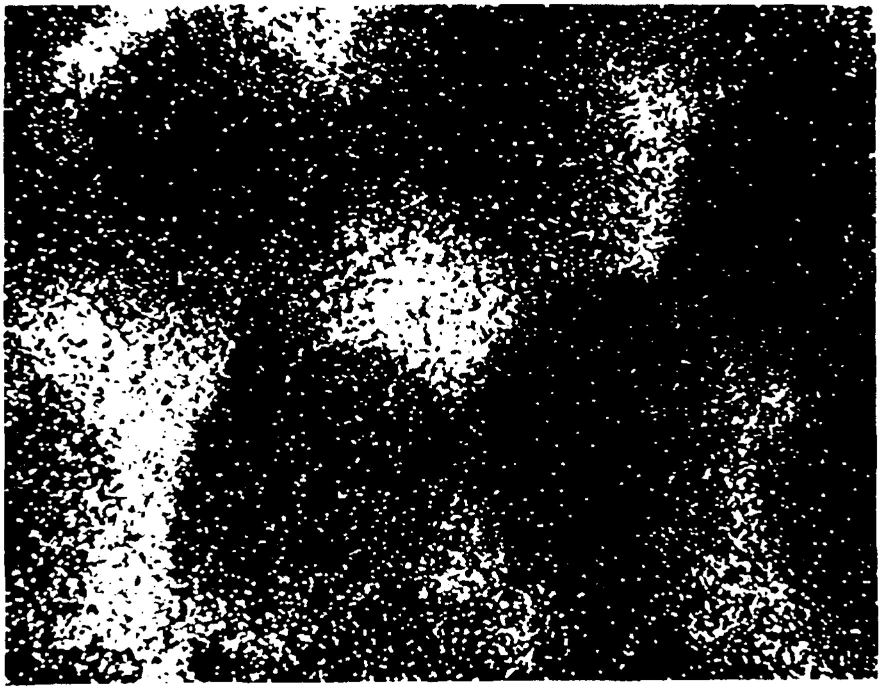

Figure 16. EDAX Si Map Corresponding To The Region Shown In Figure 3, And Viewed At The Same Magnification

Figure 17. SEM View of Composite Specimen Fractured In The Scanning Auger Microscope Showing The Microstructure

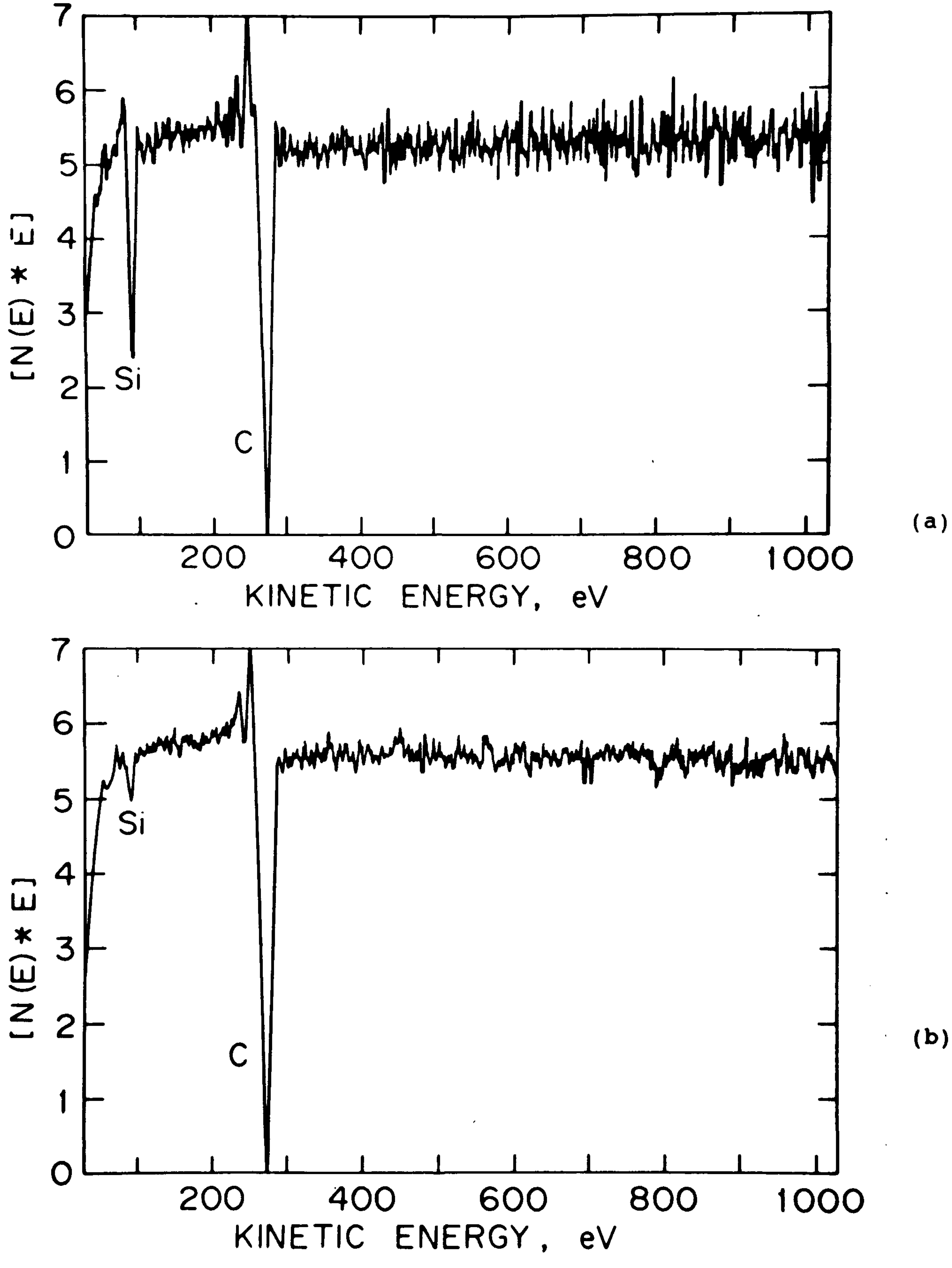

Figure 18. Typical Auger Spectra Taken From The Region Shown in Figure 5: (a) from the matrix; (b) from the fiber/matrix interface.

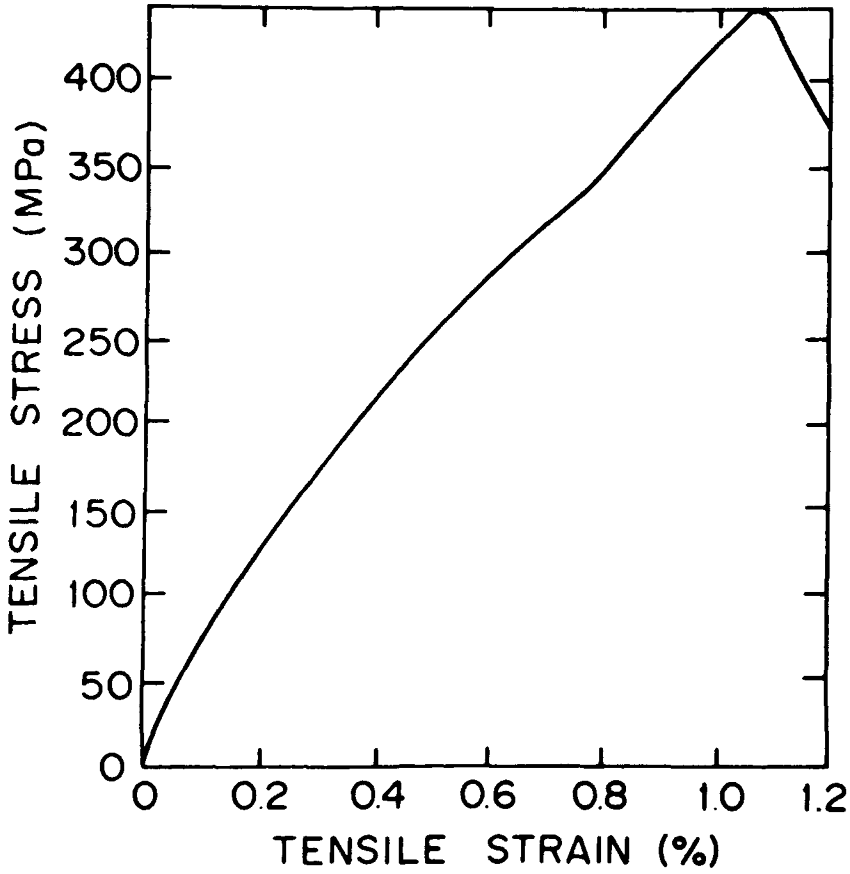

Figure 19. Tensile Stress-Strain Curve for Carbon/SiC Cross-Weave Composite. Tested at room Temperature

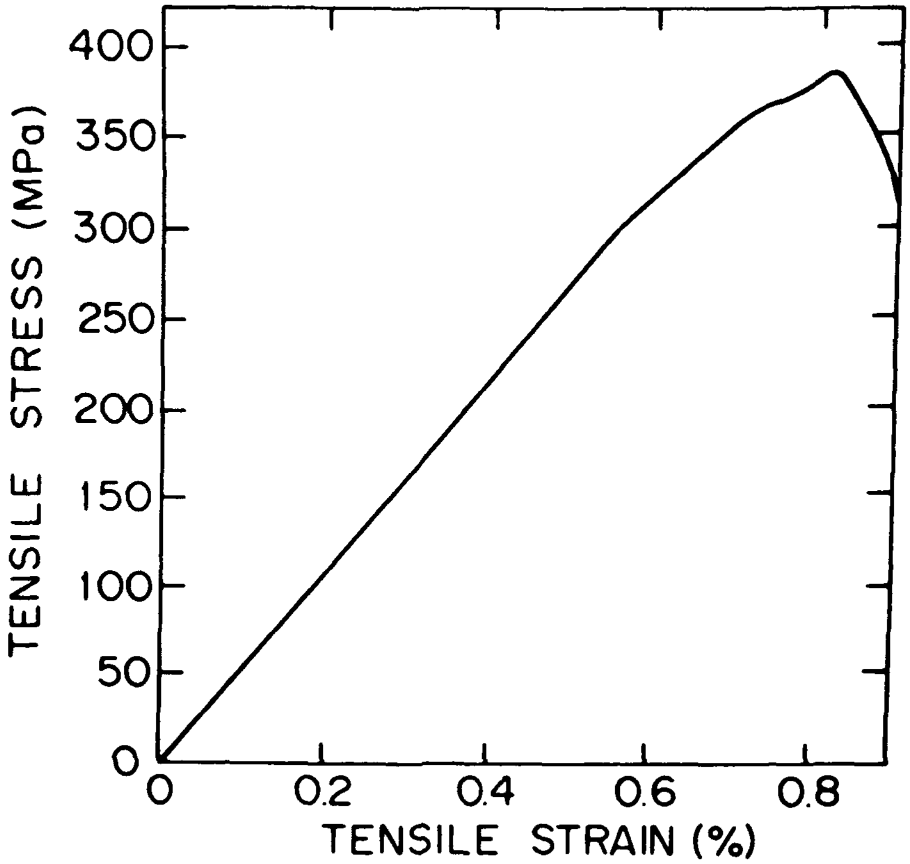

Figure 20. Tensile Reloading Stress-Strain Curve of a Composite Specimen Which Was Initially Loaded in Tension to a Stress of About 306 MPa, and Then Reloaded

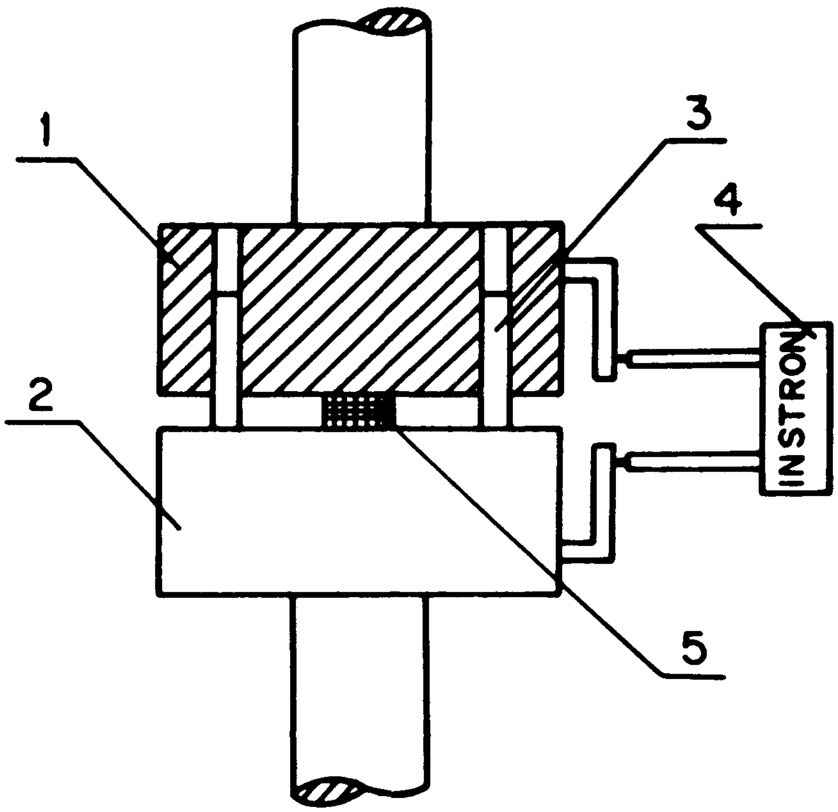

1. Upper compressive block
2. Lower compressive block
3. Guide pin
4. Extensometer
5. Specimen

Figure 21. Schematic Diagram of the Fixture for Compressive Tests

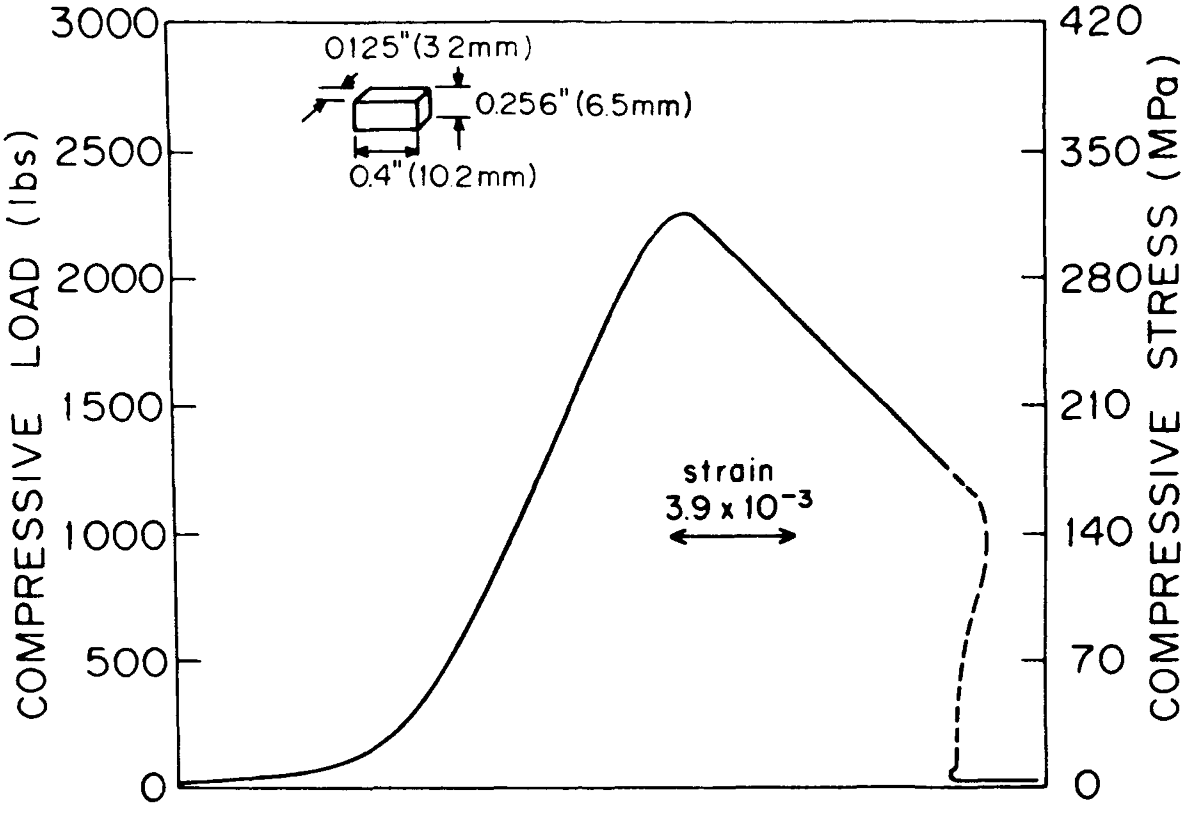

Figure 22. Compressive Stress-Strain Curve At Room Temperature For Carbon/SiC Cross-Weave Composite

Figure 23. SEM micrograph taken from a specimen which was loaded in compression to the ultimate stress level, showing fiber buckling and matrix fragmentation. The direction of the applied compressive stress is horizontal.

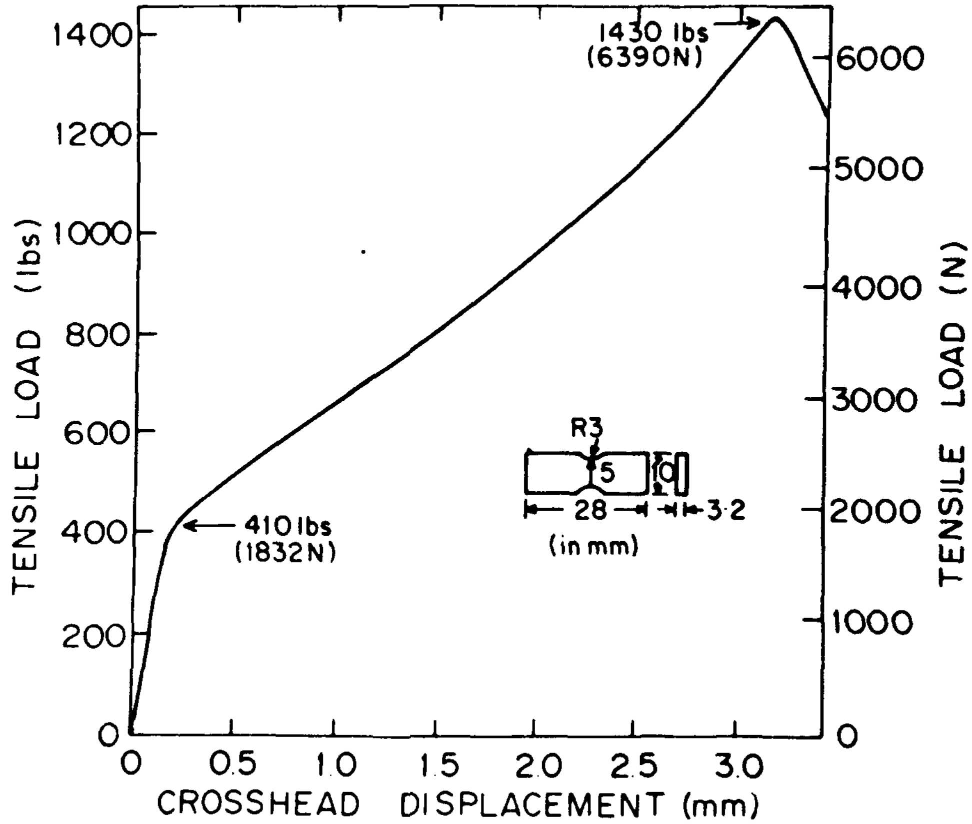

Figure 24. Tensile Load vs. Crosshead Displacement Curve for a Notched Composite Specimen. Tested at Room Temperature.

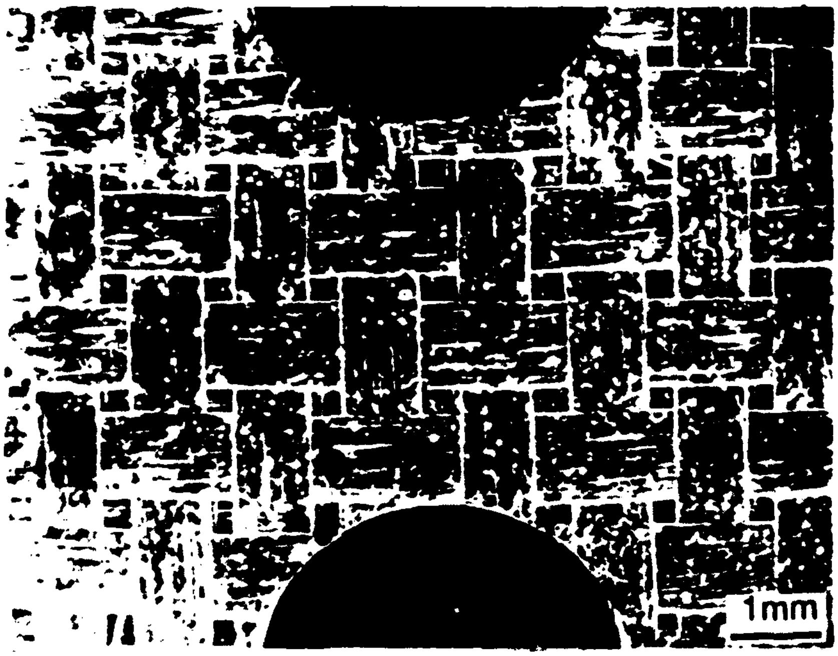

Figure 25. The Appearance of the Notched Gage Section on a Specimen for Studying Tensile Failure Processes, Before Loading

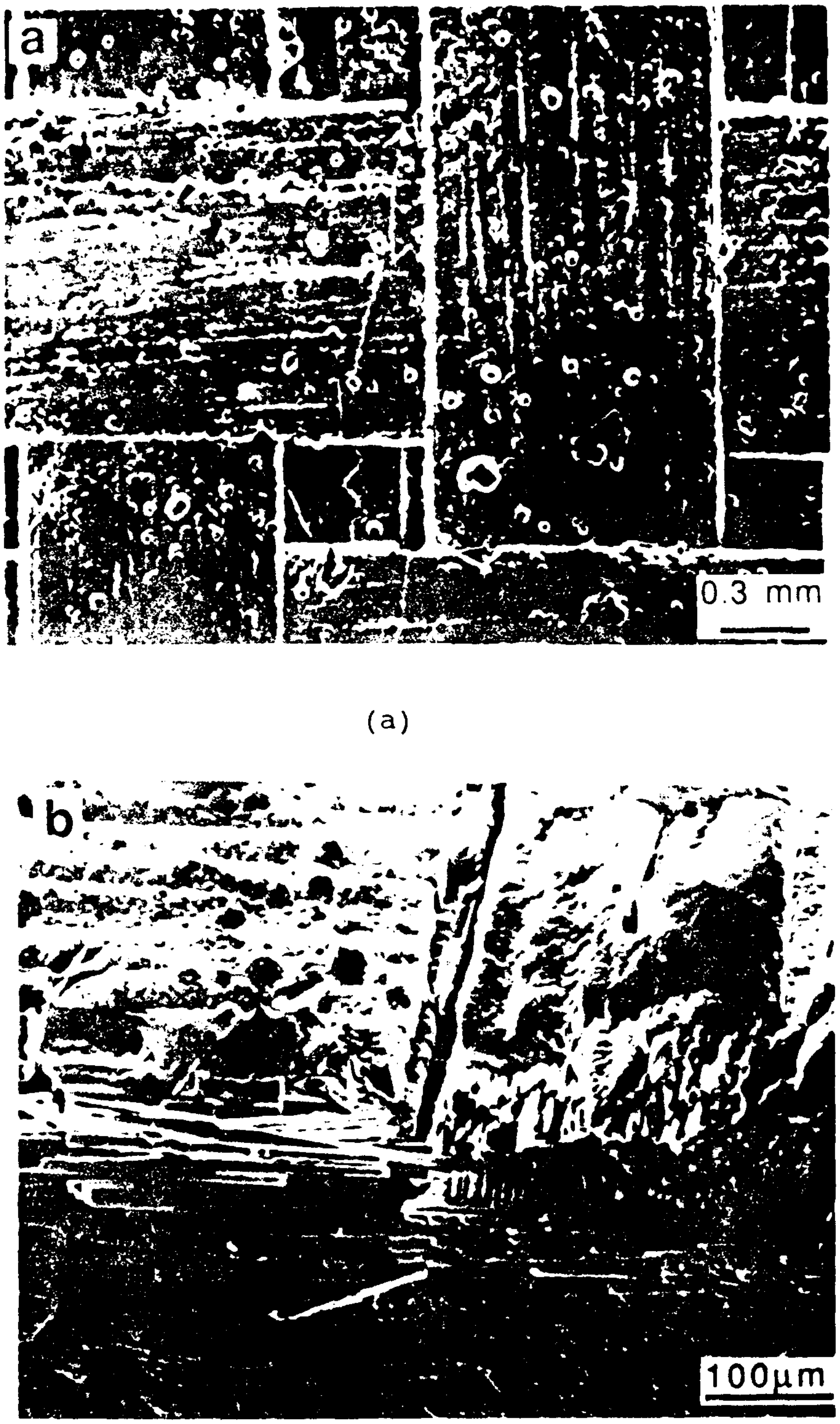

(a)

(b)

Figure 26. Cracking of c/sic composite after exposure to tensile load of 2681 N. (a) Normal View; (b) Side View

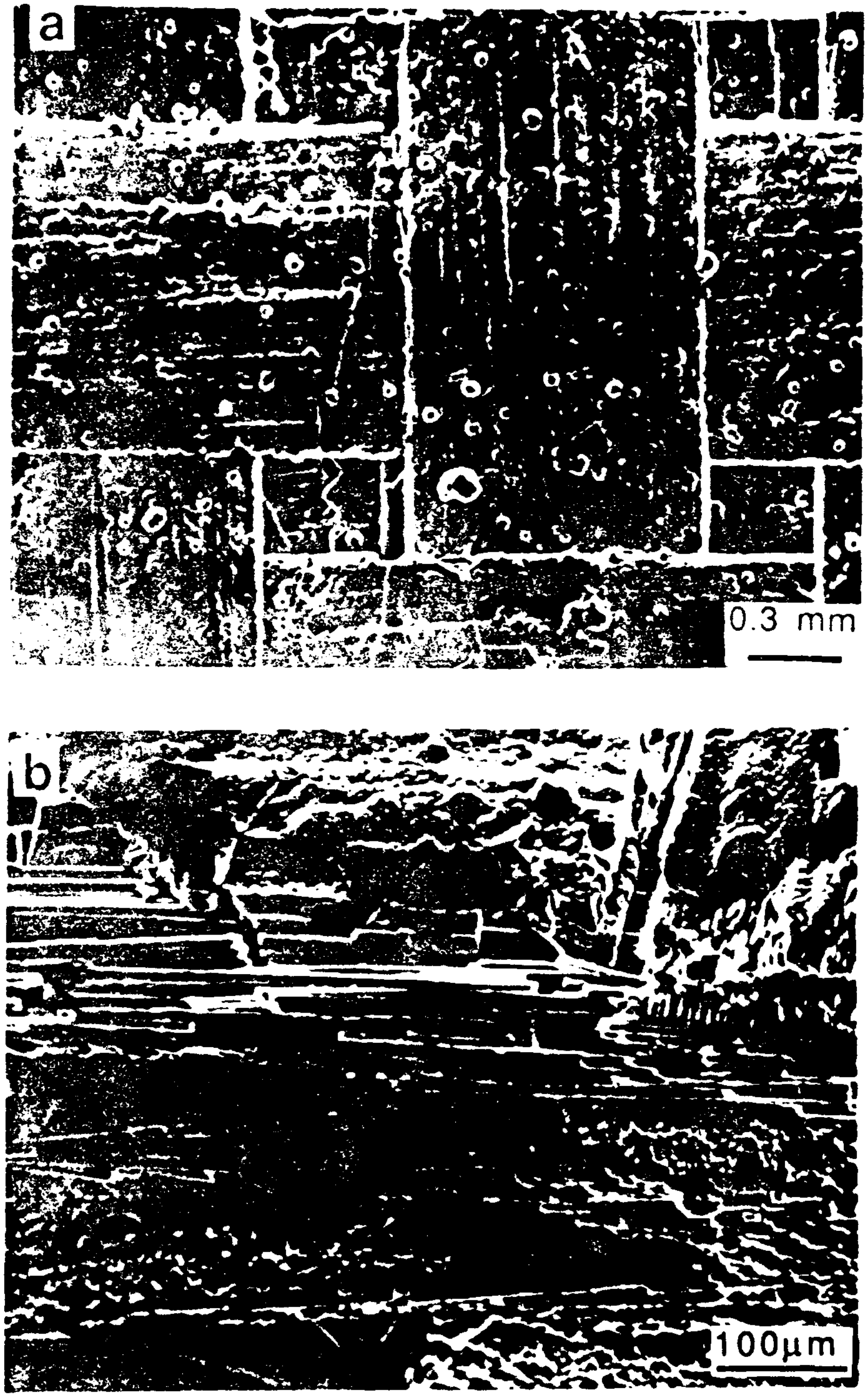

Figure 27. The Same Area as That Shown in Figure 14 After Loading in Tension to 4469 N (1000 lbs)

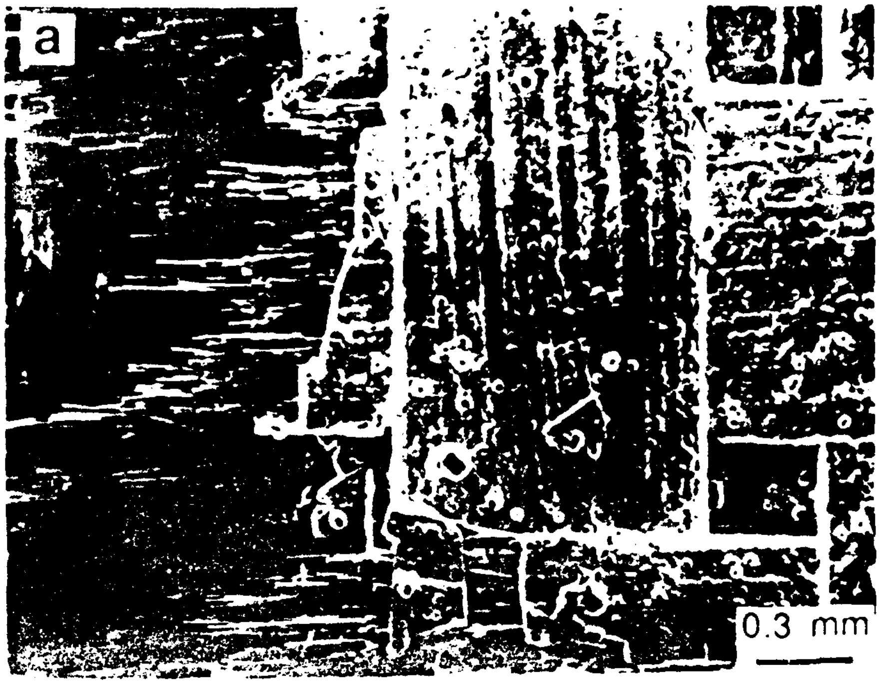

Figure 28. The Appearance of the Specimen After Fracture at 6256 N (1400 lbs); the Same Area as in Figures 14 and 15 is Shown

Figure 29. Macroscopic View of the Fracture Surface of a C/SiC Cross-Weave Composite Failed in Tension

Figure 30. Characteristic feature of fiber bundle fracture viewed at an angle to the fracture surface. (a) Near the sample edge; (b) in the sample interior, showing adherence of the ceramic to the fibers

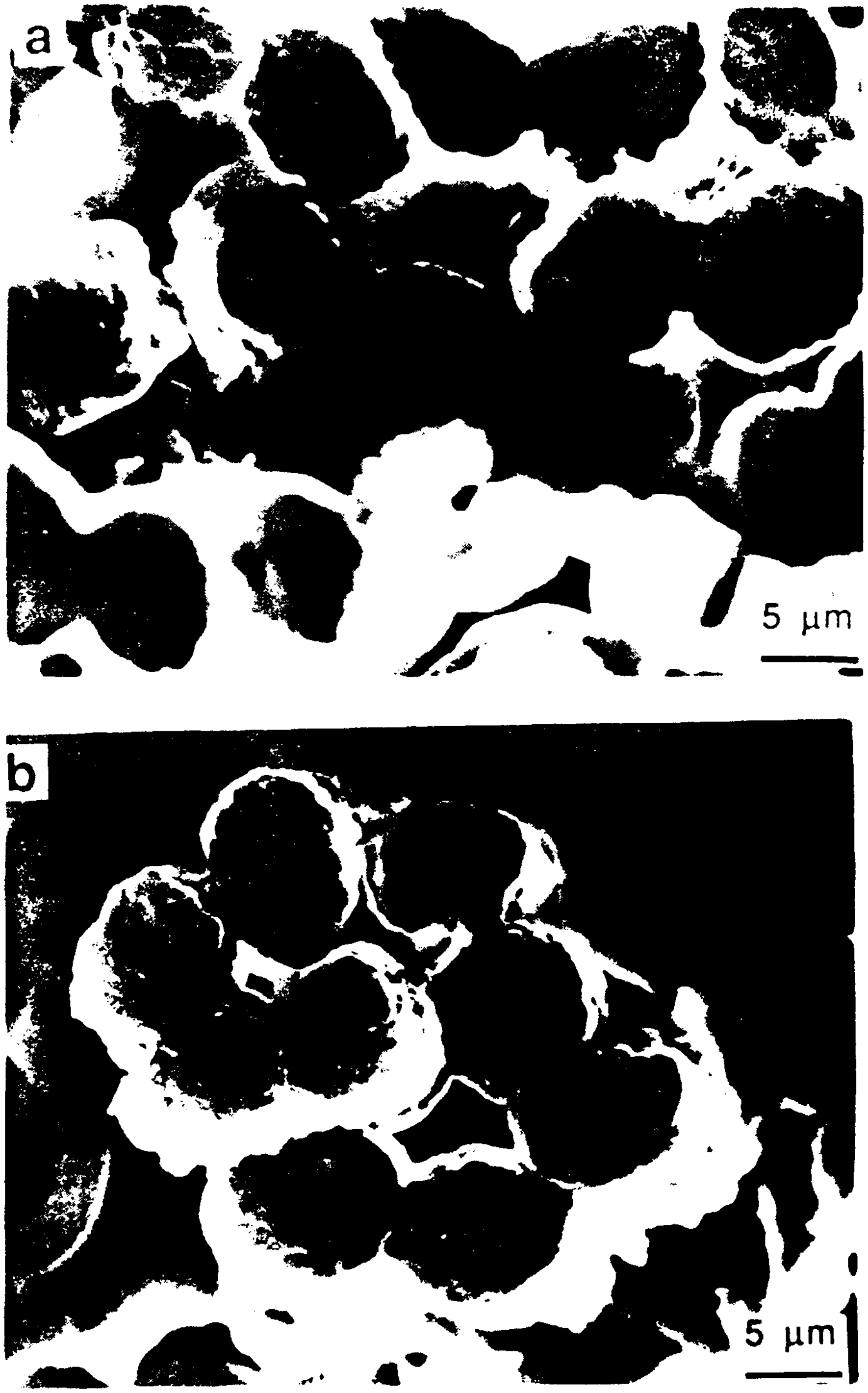

Figure 31. Characteristic Features of Fiber Bundle Fracture, Viewed Normal to the Fracture Surface

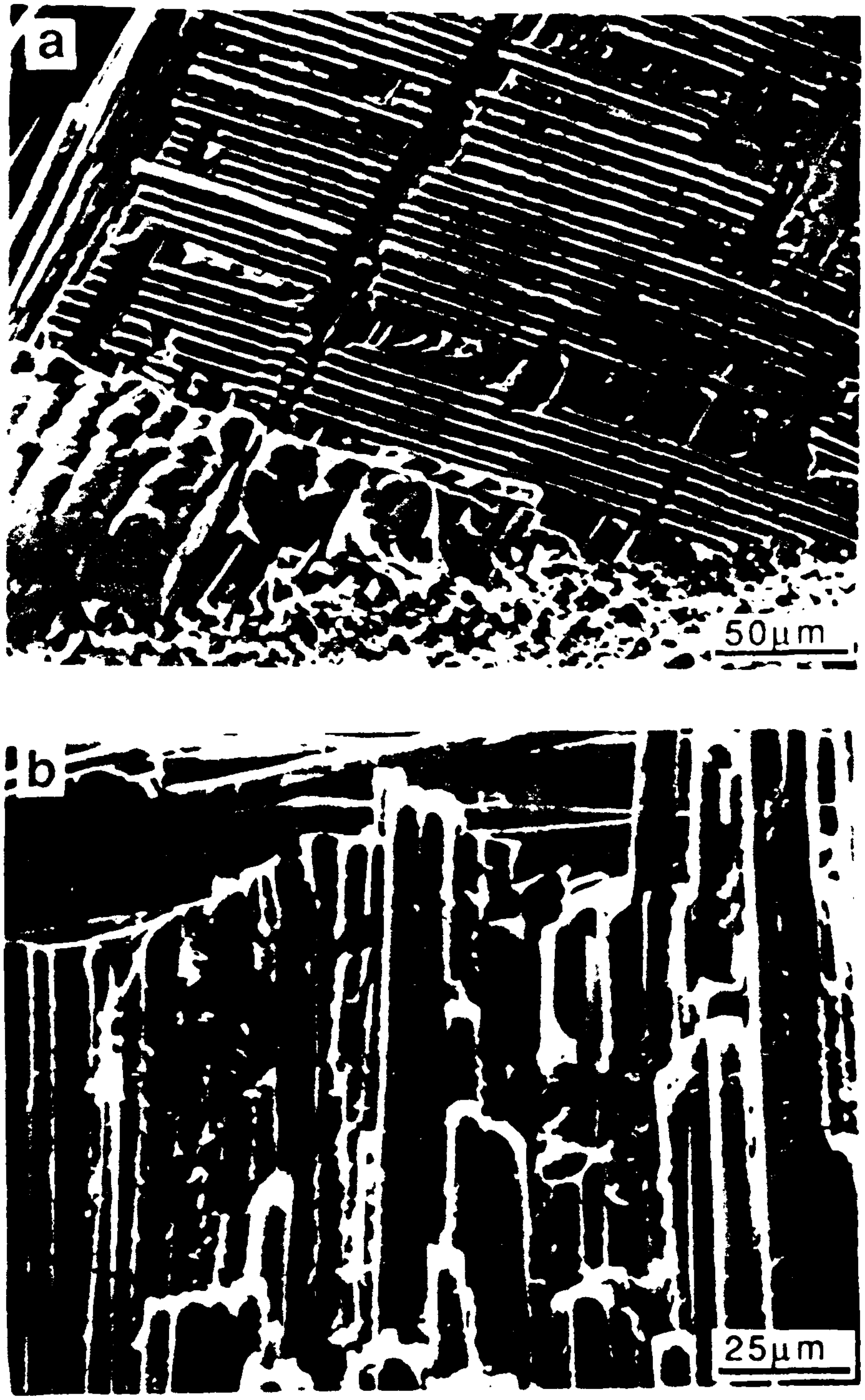

Figure 32. SEM micrographs of fracture surface, showing fiber debonding and pull-out (a, b) and showing an example of a matrix crack cutting fibers (b)

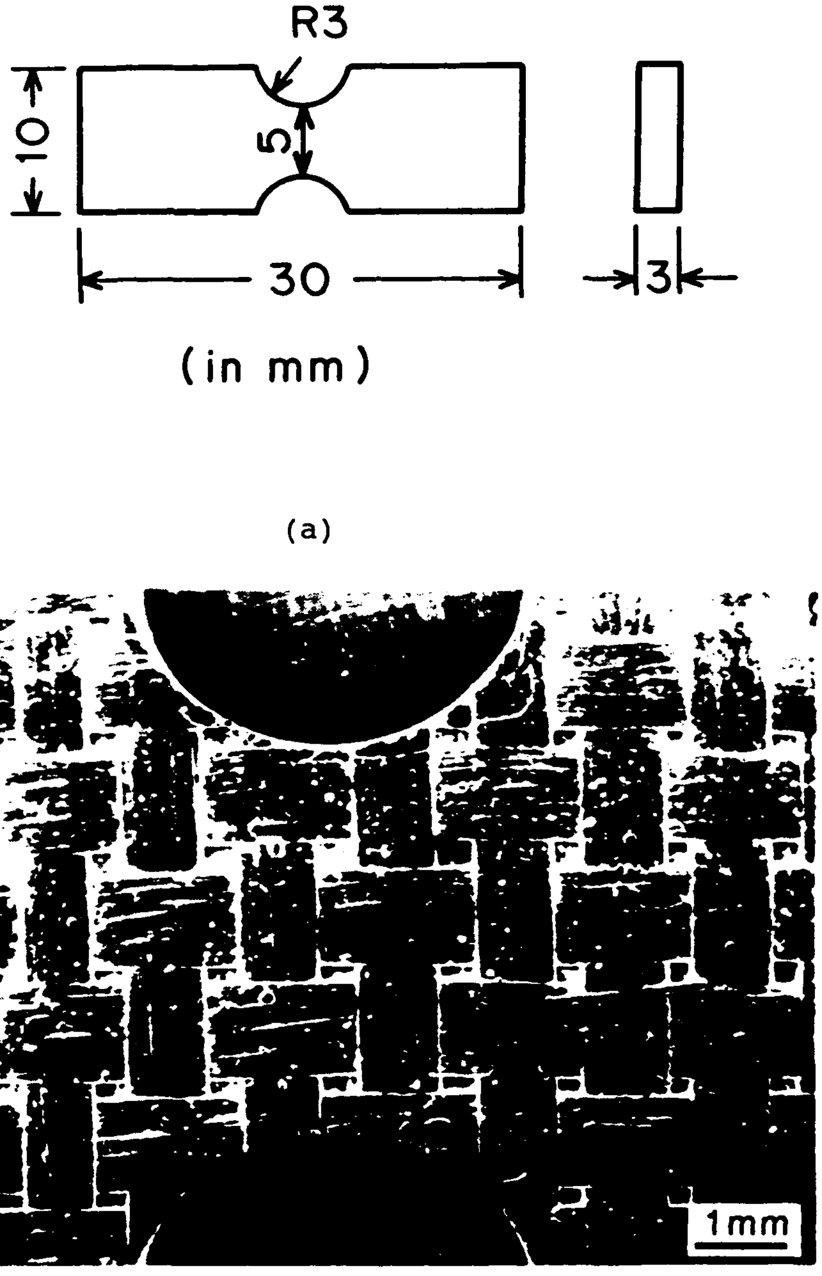

Figure 33. The Notched Specimen Used for Cyclic Tension-Tension Tests. (a) Dimensions; (b) Appearance of an Actual Specimen

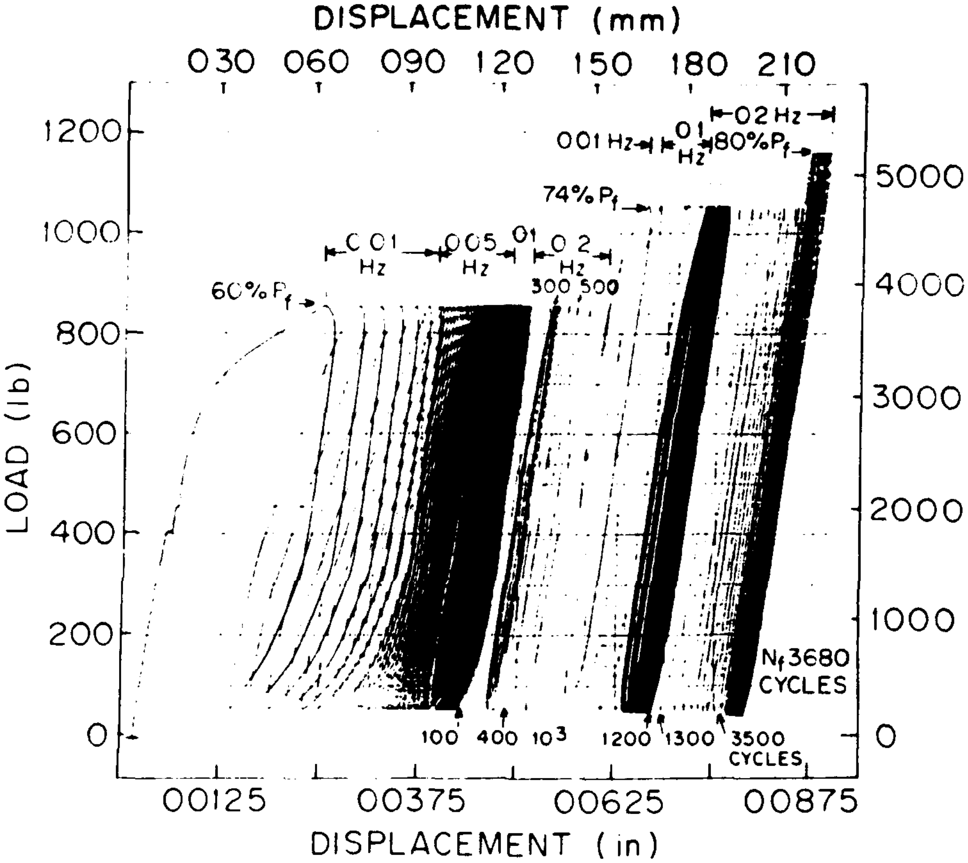

Figure 34. Cyclic Load-Displacement Response of the Notched Specimen Subjected to an Ascending step Test Using Various Frequencies Indicated

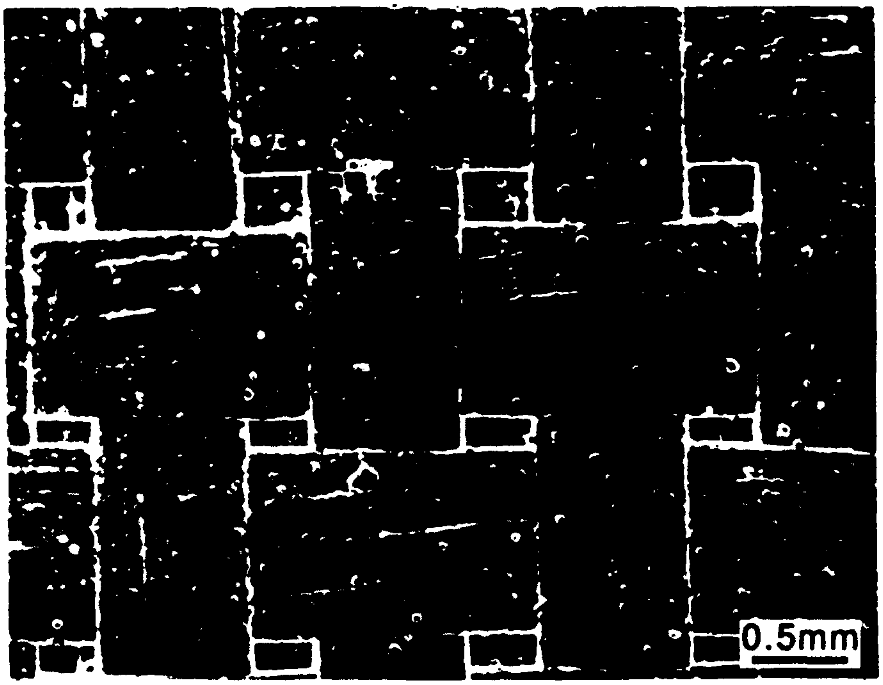

Figure 35. The Central Surface Area of the Notched Specimen Before Testing

Figure 36. The same area as in figure 3 after the specimen was cycled for 150 cycles under a load range from 222N to 3782N. (a) and (b) are at different magnifications. The loading axis is horizontal.

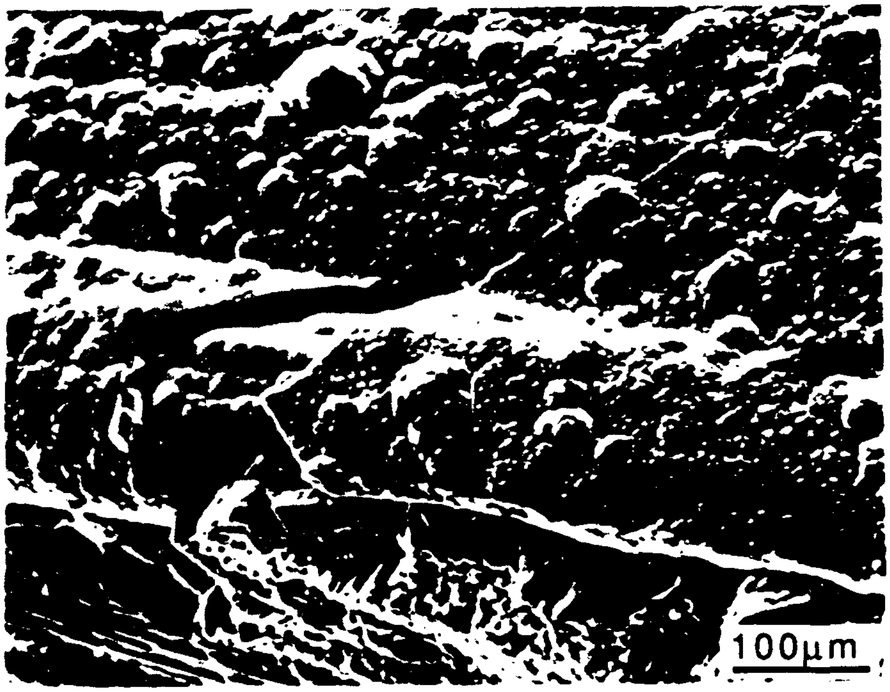

Figure 37. SEM Micrograph Showing the Damage to the Specimen Edge Due to Cycling Under a Load Range From 222N to 2783N for 150 cycles

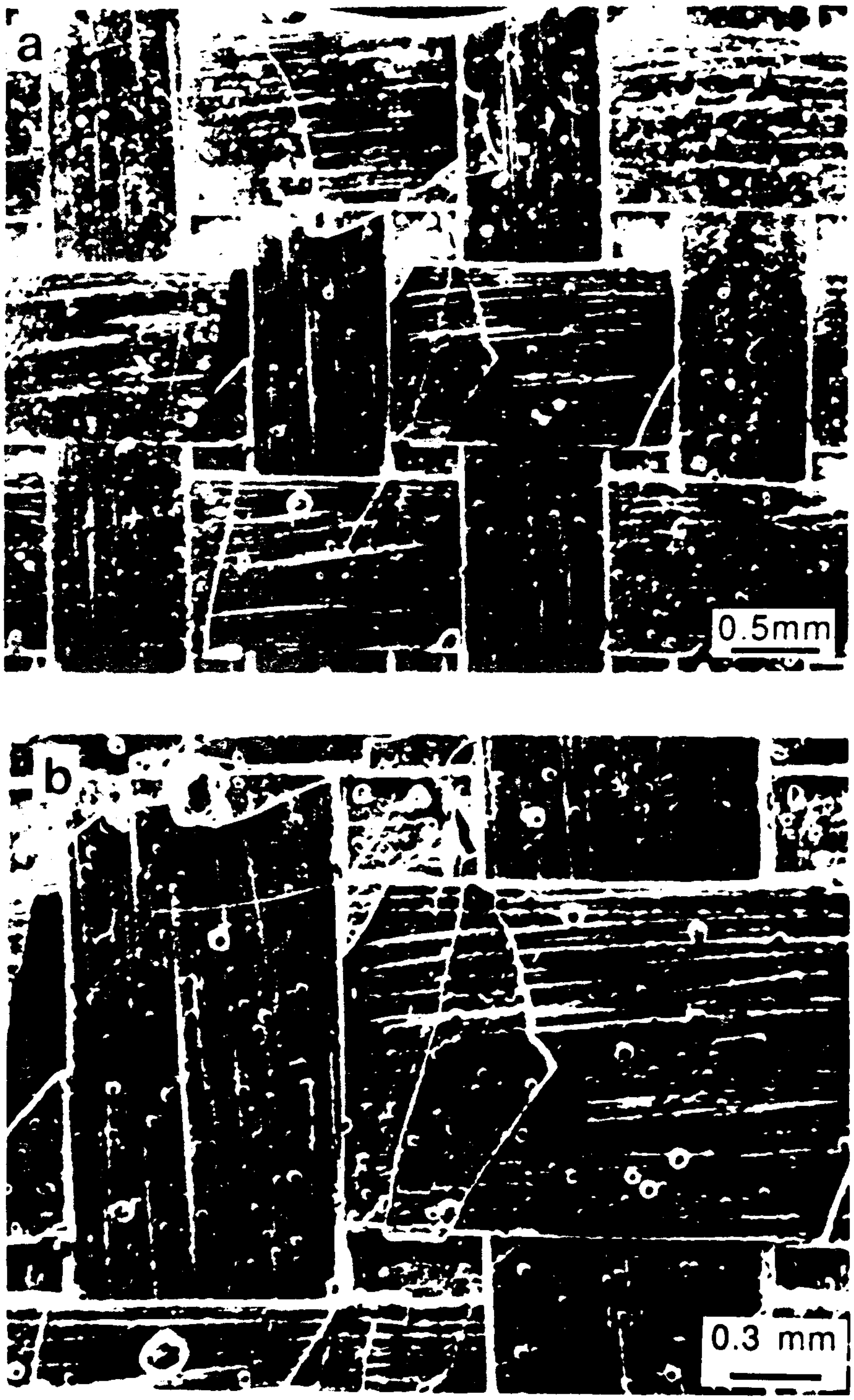

Figure 38. SEM micrographs taken from the same areas as in Figure 4 after the specimen was subjected to a further cyclic exposure for 700 cycles. (a) and (b) were taken under different magnifications.

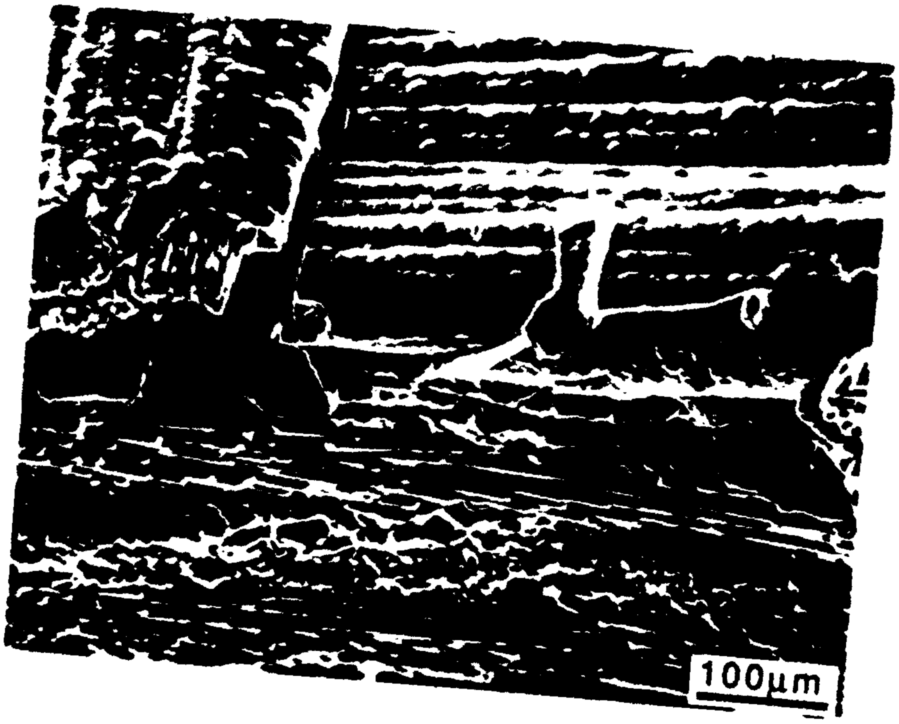

Figure 39. The appearance of the specimen edge after a further cycling for 700 cycles. Notice that the far right area shows the same area as seen in the left lower corner of Figure 5.

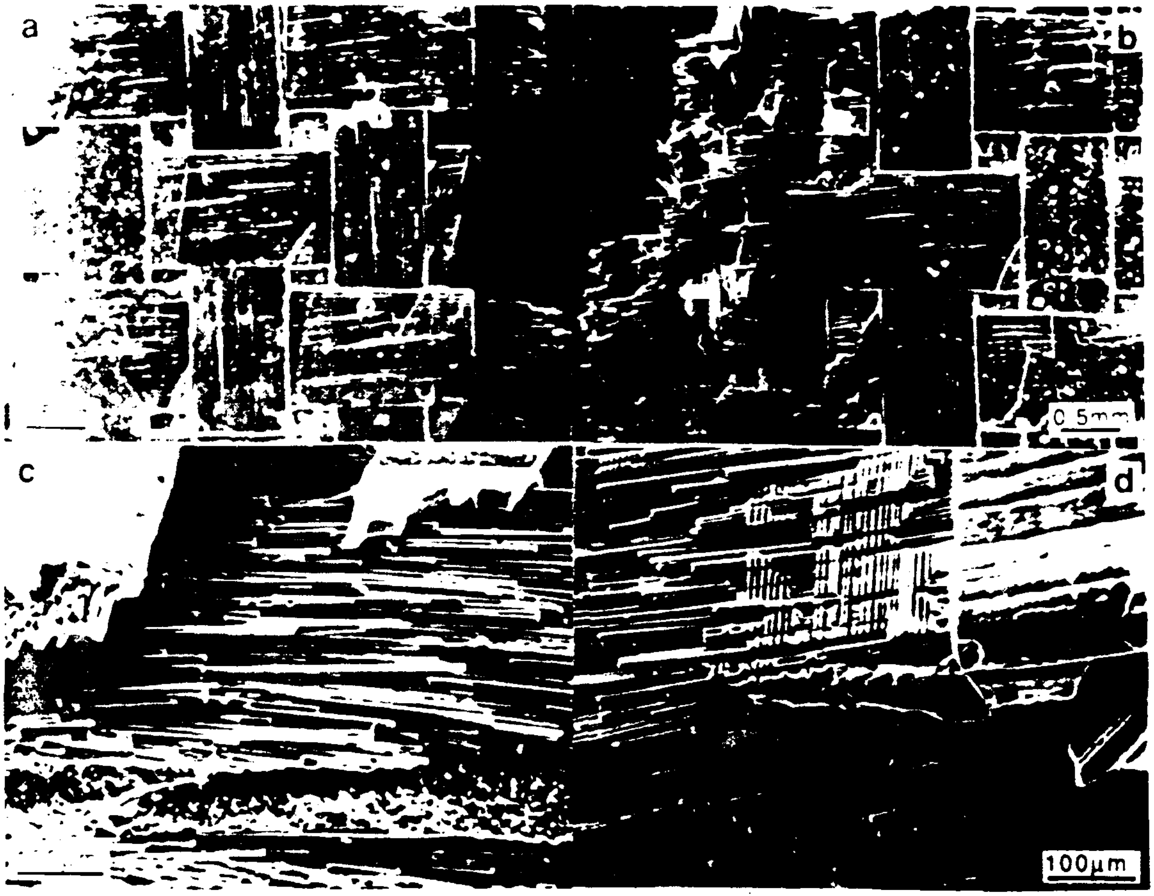

Figure 40. SEM micrographs showing the characteristic features of the totally failed specimen. (a) and (b) are seen normal to the surface. (c) and (d) show the appearance of the specimen edge.

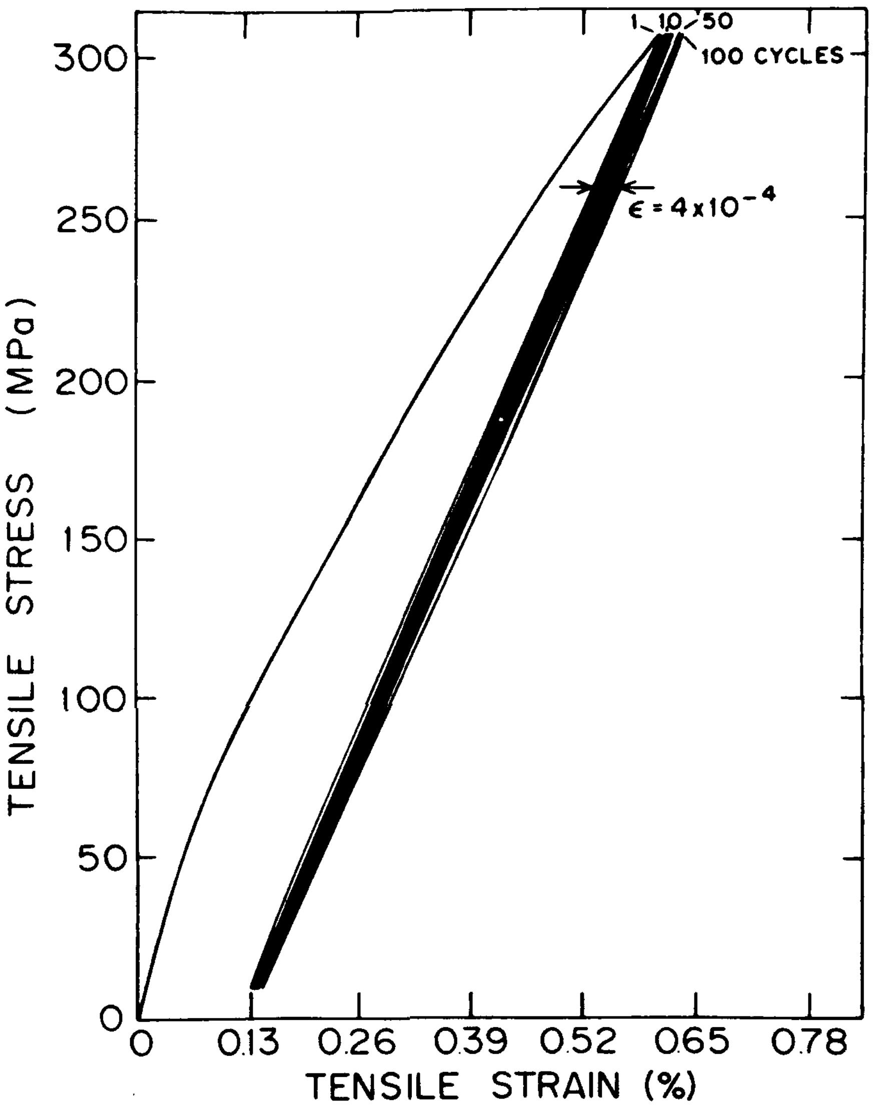

Figure 41. Stress-Strain Response of a Smooth Full-Size Specimen Cycled in Tension (R=+0.028) for 100 Cycles .

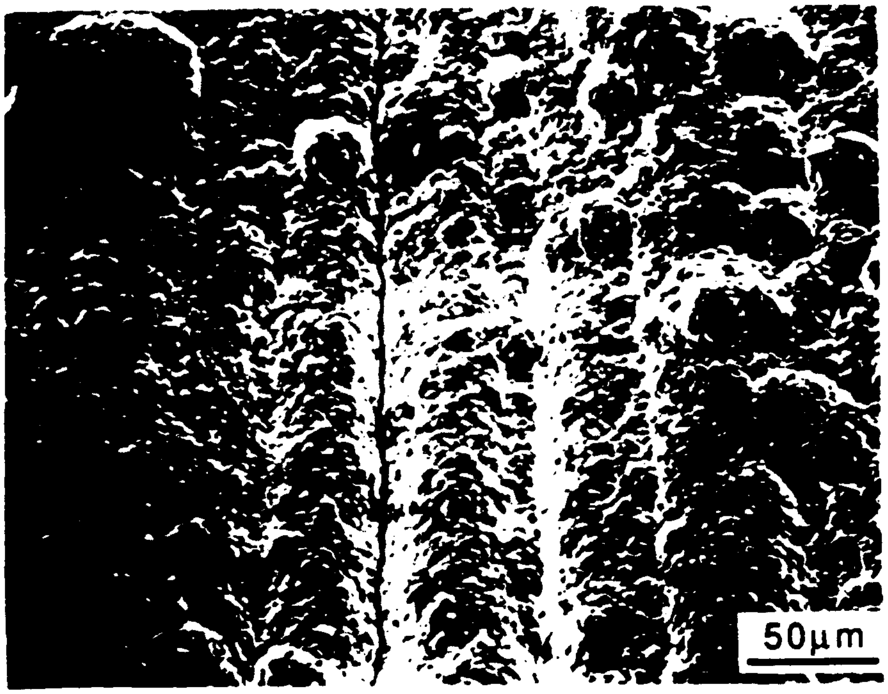

Figure 42. SEM micrograph showing a surface microcrack after the specimen was cyclically loaded for 1000 cycles under a stress range from 8.75 MPa to 3.08 MPa. The stress axis is horizontal.

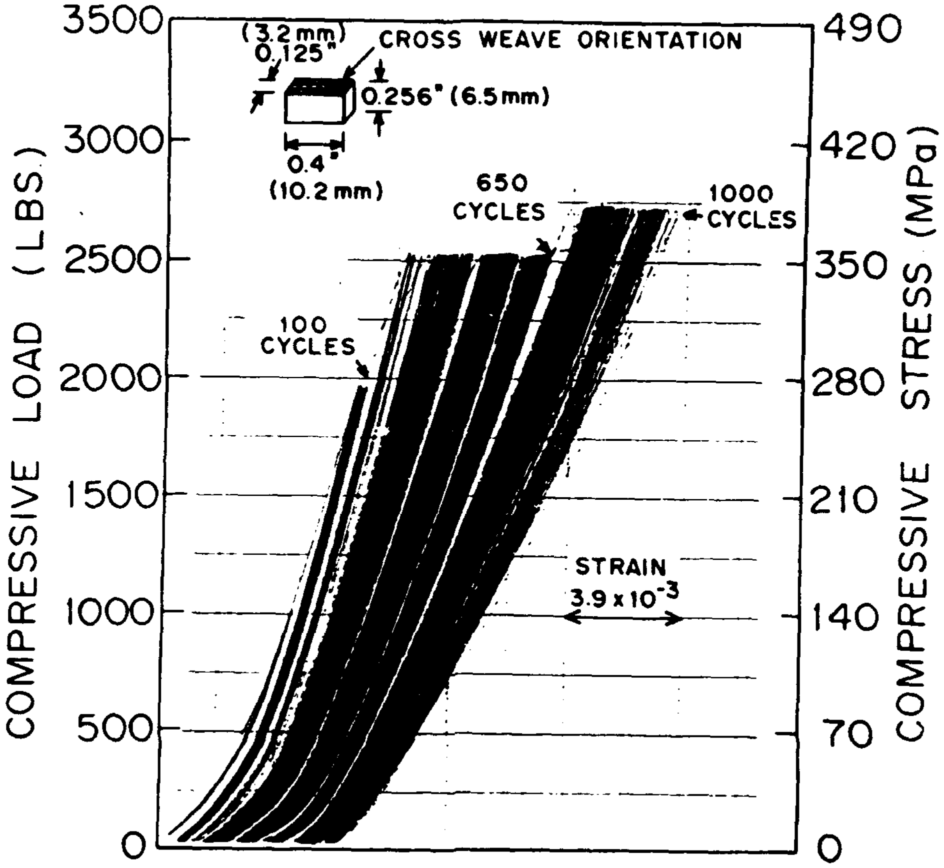

Figure 43. Cyclic compressive stress-strain response of C/SiC composite subjected to a three-step test. The configuration of the specimen is shown in the insert.

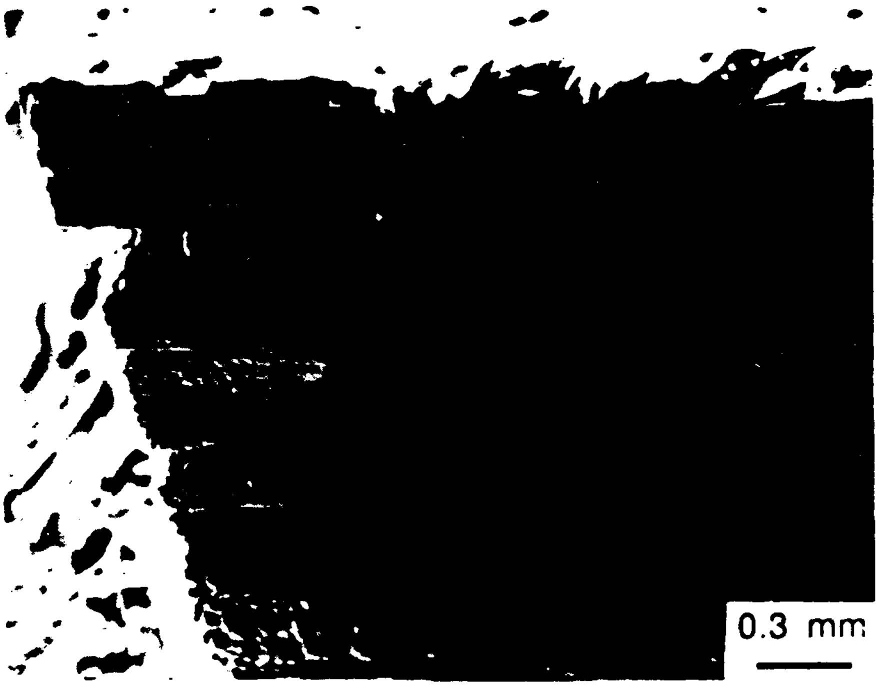

Figure 44. SEM micrograph of the specimen edge delamination after the specimen was cycled in compression-compression for 500 cycles. The stress axis is horizontal.

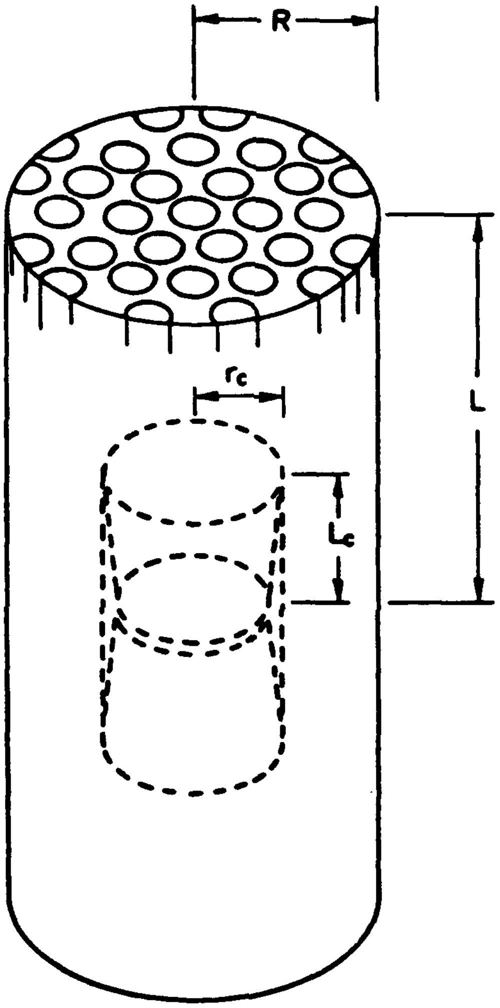

Figure 45. H–Shaped Crack In A Cylindrical Representative Volume Element.

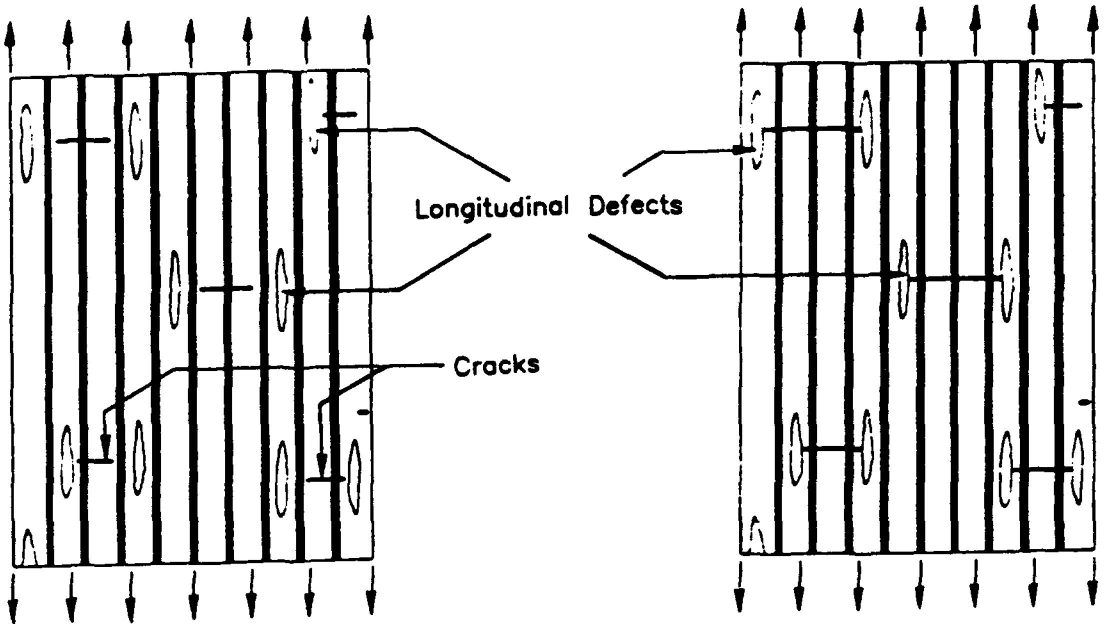

(a) Crack Initiation

(b) Transverse Crack Arrest

(c) Axial Crack Growth And Arrest

(d) Failure

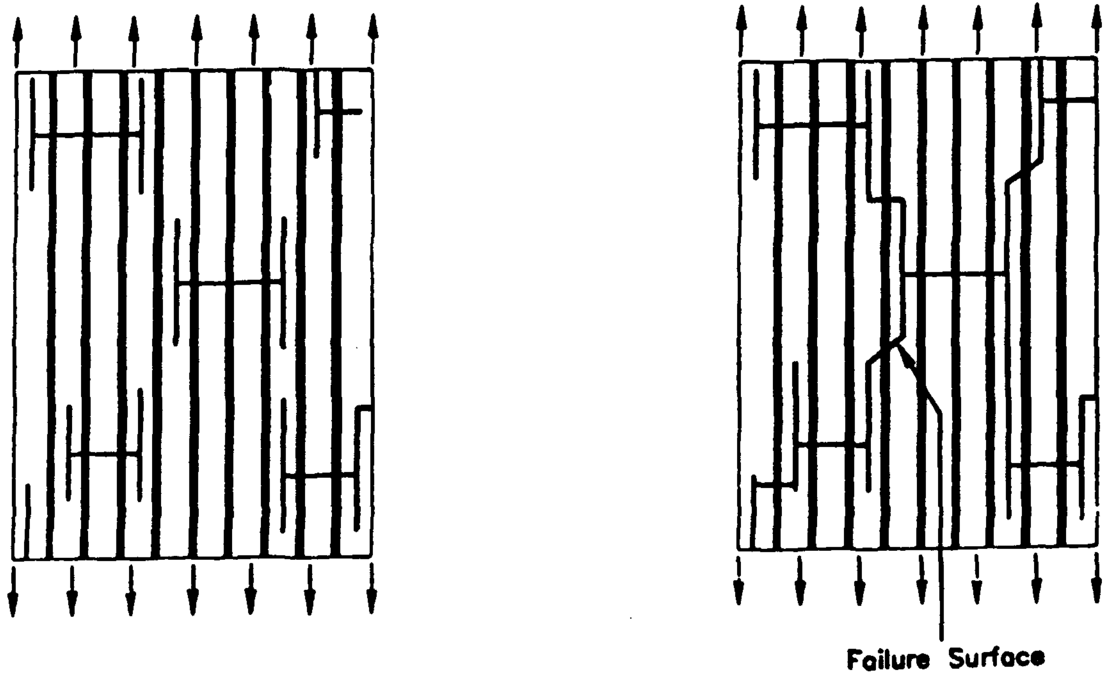

Figure 46. Failure Scenario For Ceramic Matrix Composites.

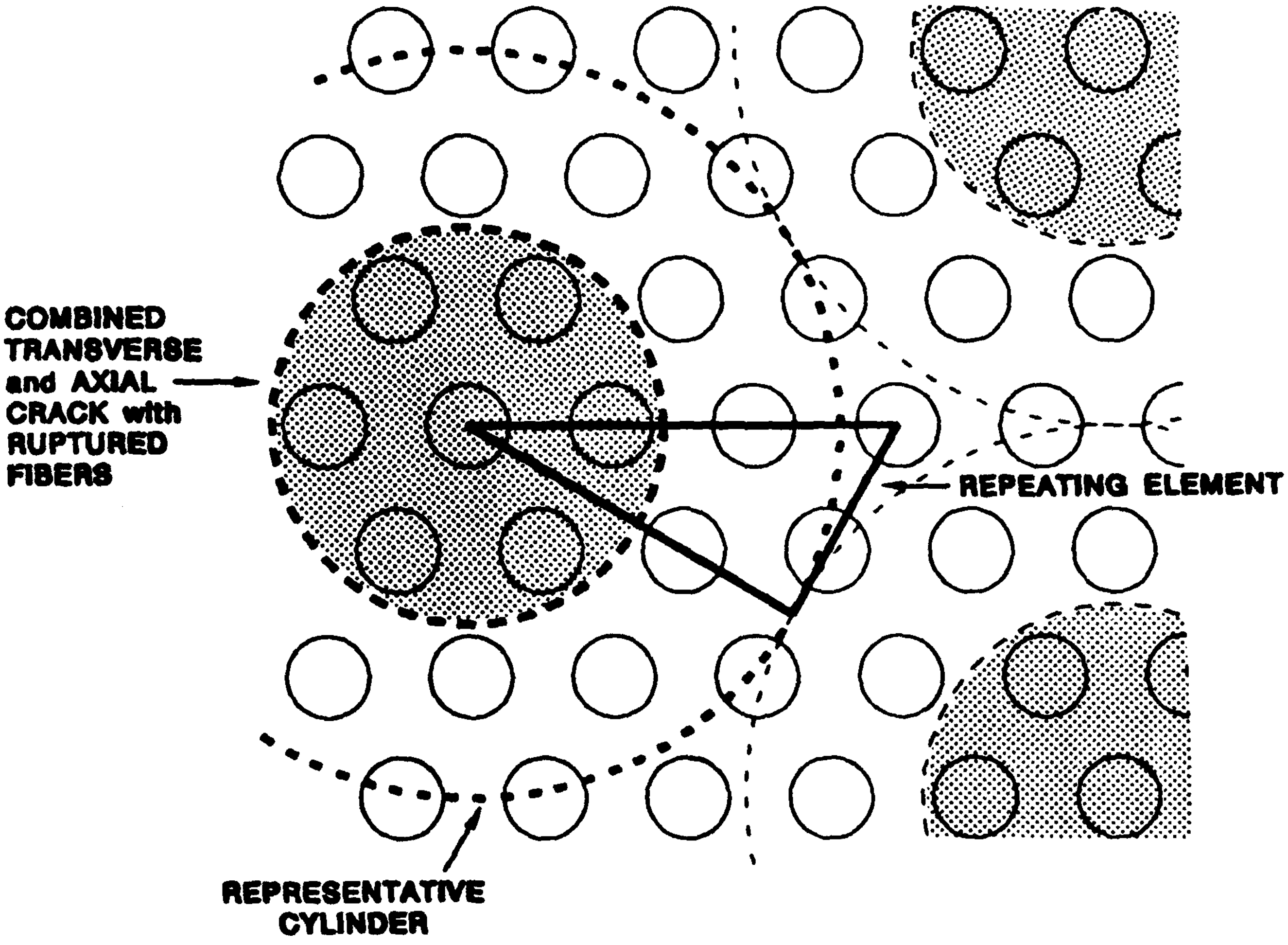

Figure 47. Local Failure Model Assuming A Hexagonal Array Of Identical Fibers.

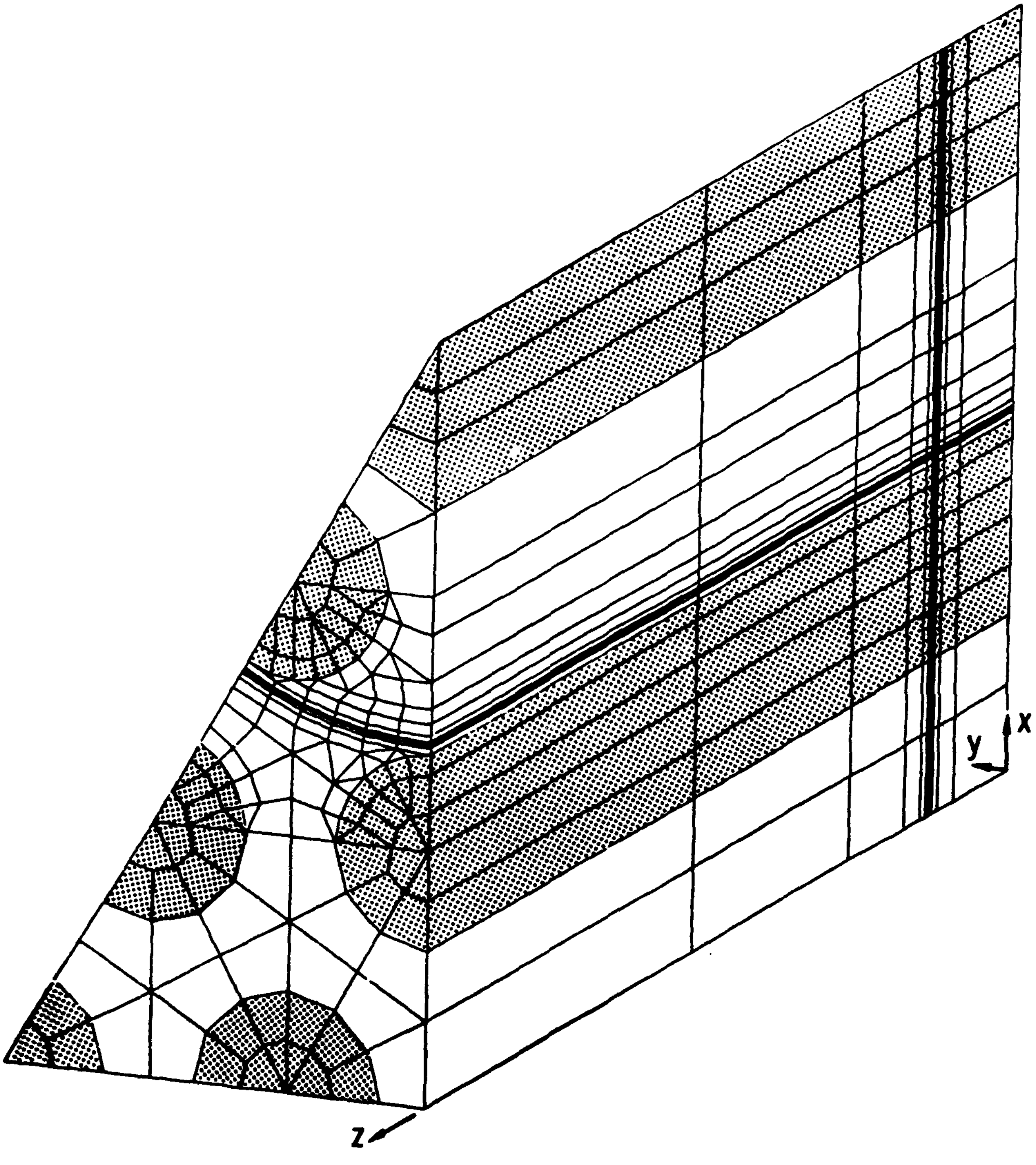

Figure 48. Axial Progagation Of Transverse Crack Through 7 Fibers And Matrix: STABLE.

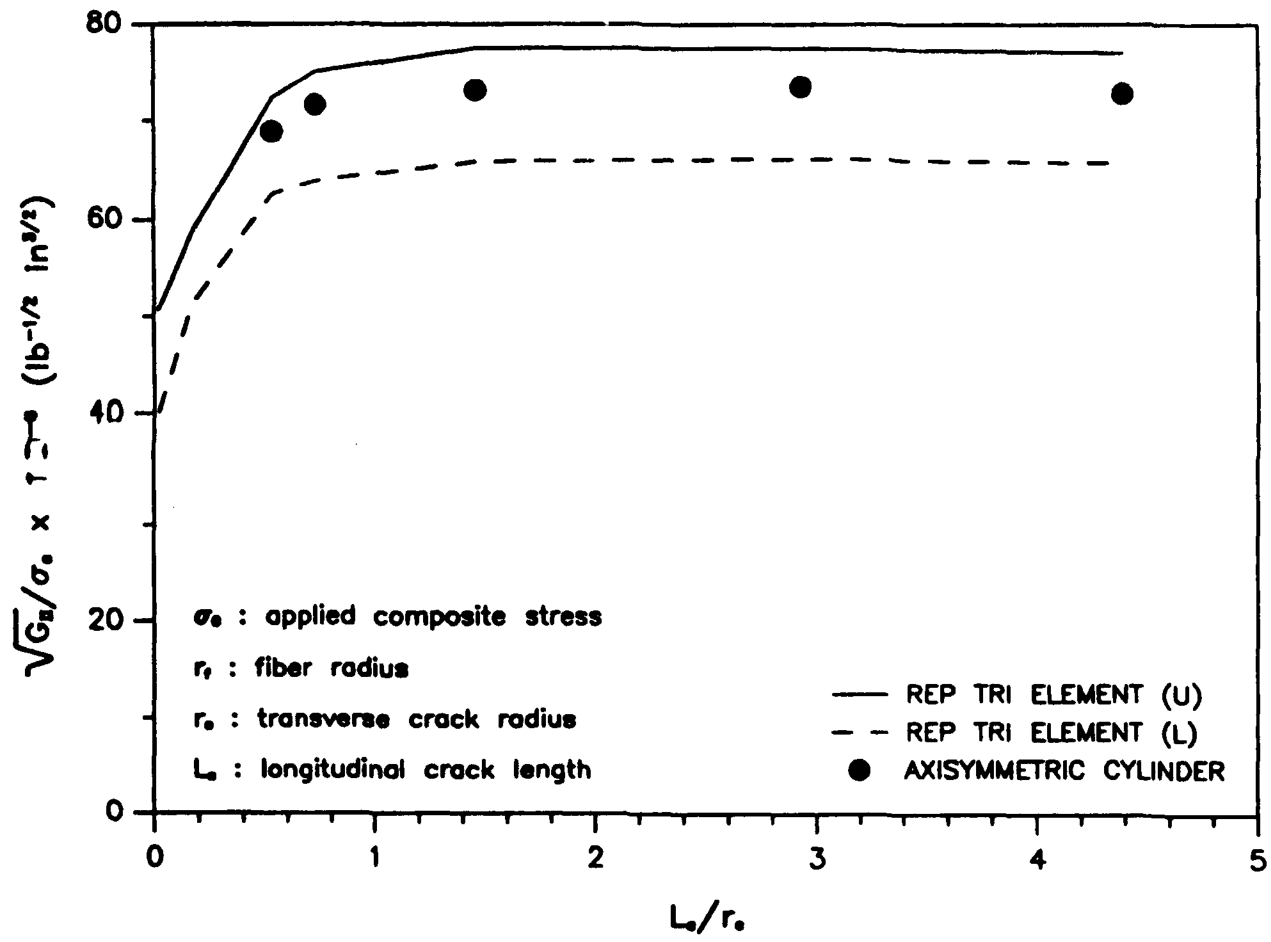

Figure 49. Energy Release Rates In Mode II At Tip Of Longitudinal Crack In Unidirectional Graphite/SiC. r_e/r_f = 4.11, V_f = 40%

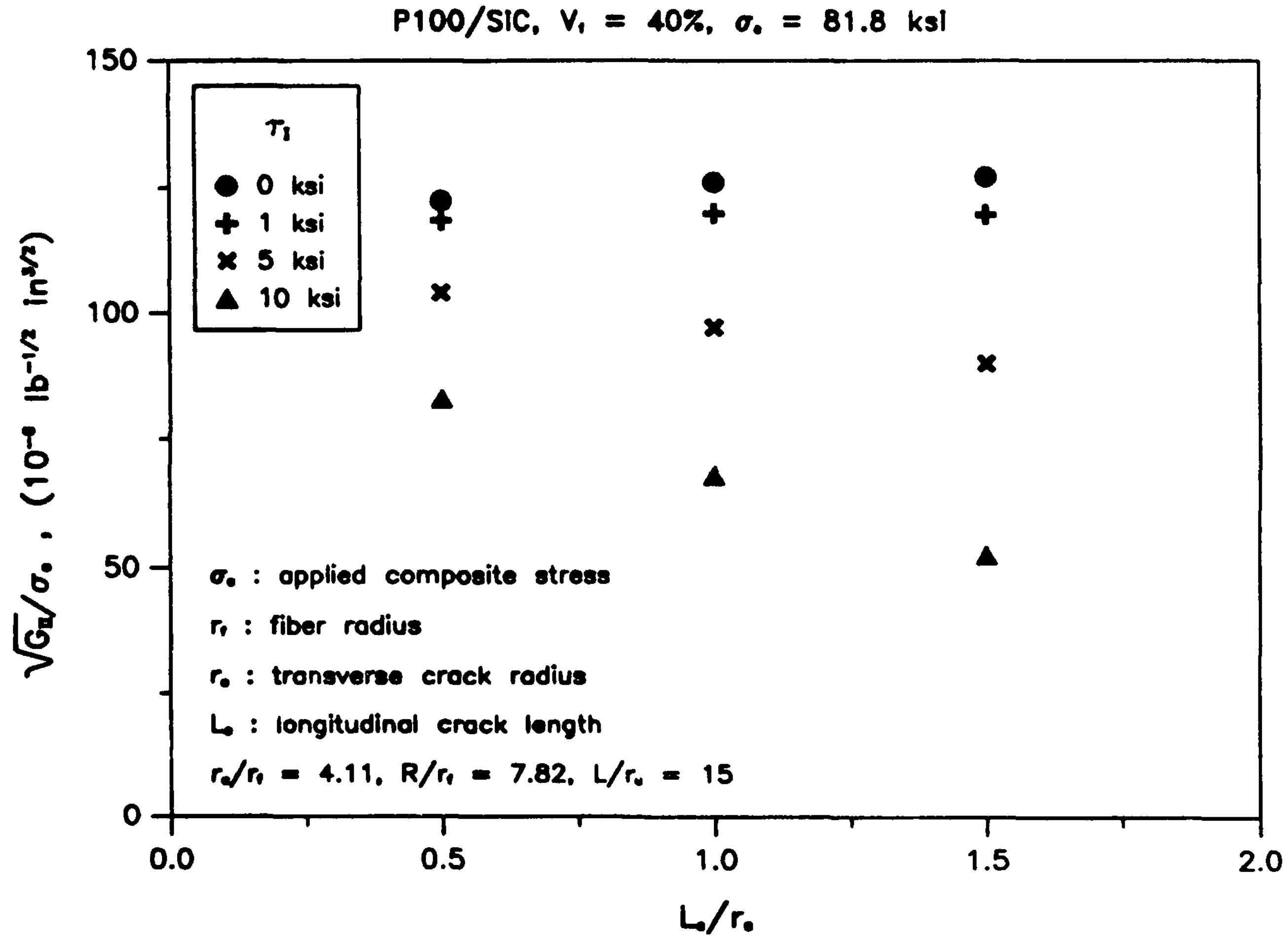

Figure 50. Energy Release Rates In Mode II At Tip Of H-Crack In A Cylindrical RVE Subjected To A Uniform Axial Displacement.

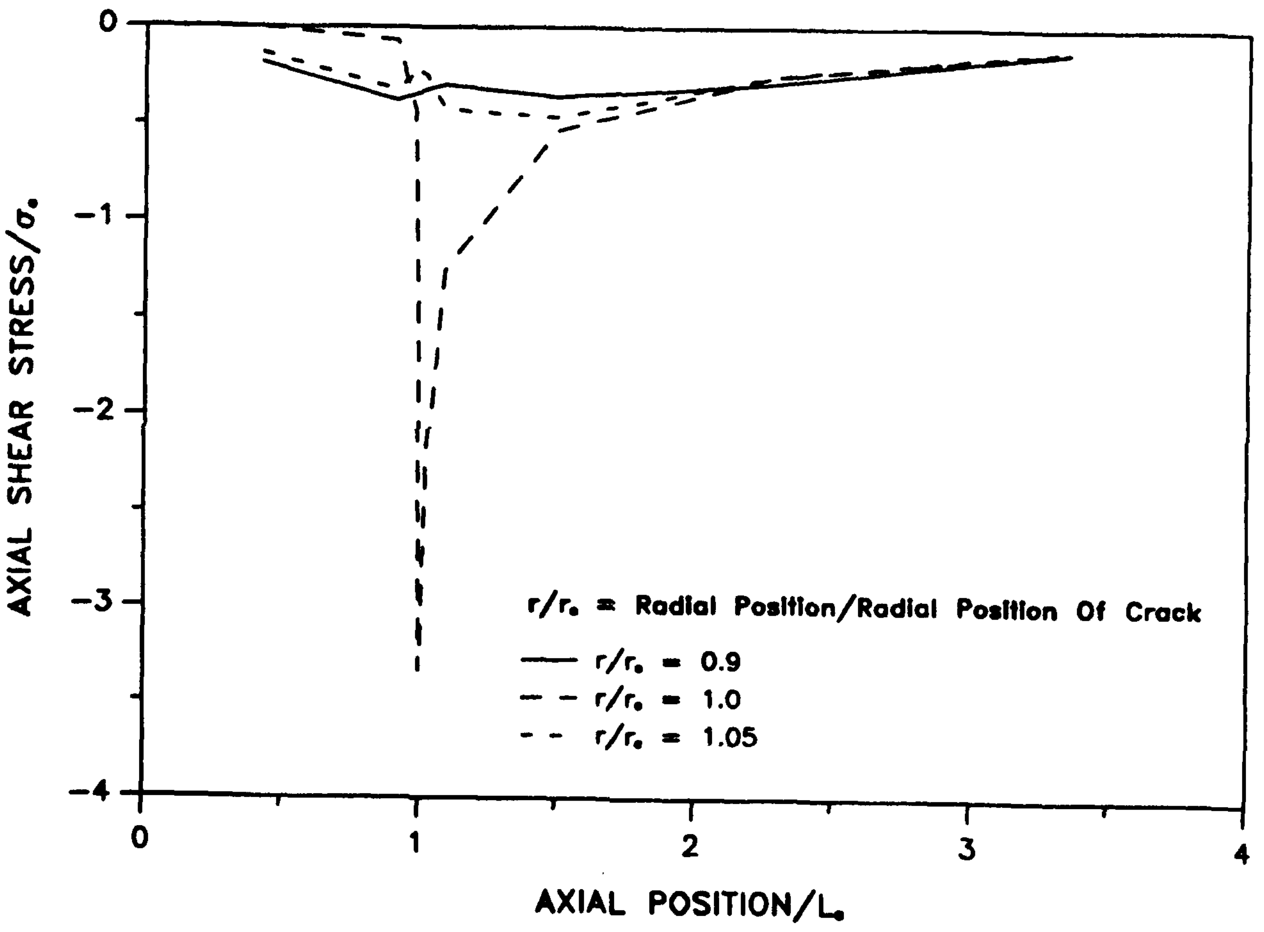

Figure 51. Shear Stress Distributions Along Axial Direction At Various Radial Locations For An Imposed Uniform Axial Traction.

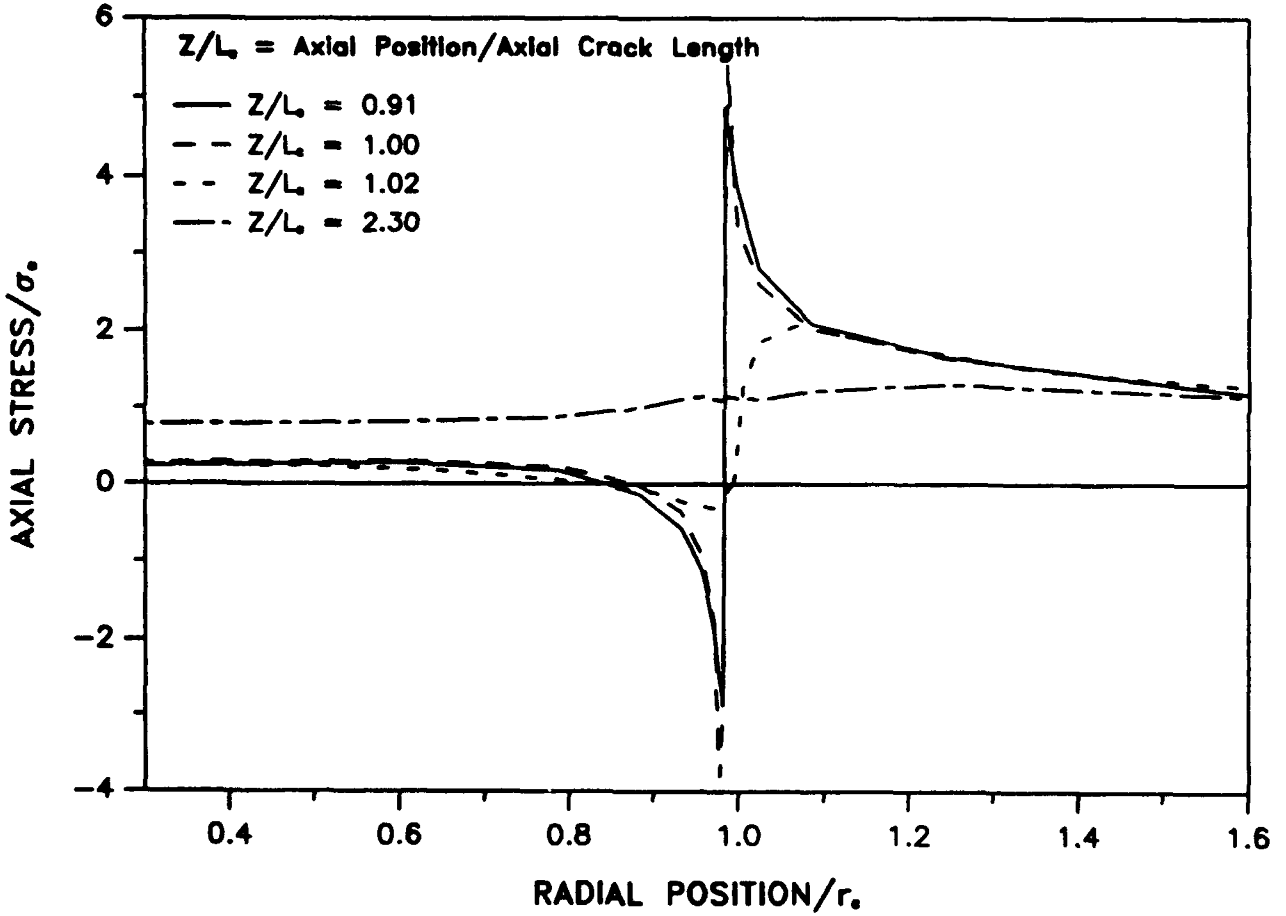

Figure 52. Axial Stress Distributions Along Radial Direction At Various Axial Locations For An Imposed Uniform Axial Traction.

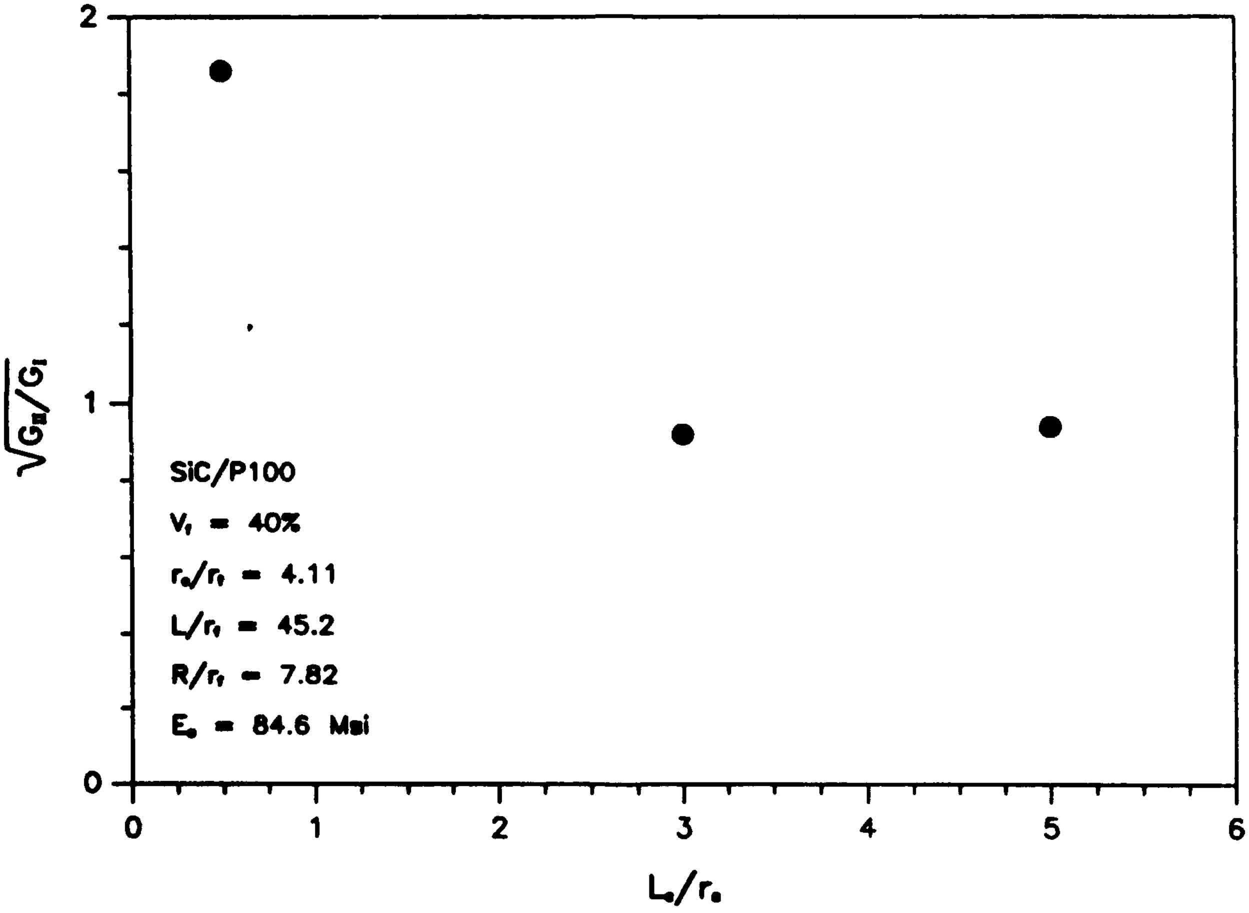

Figure 53. Values Of $\sqrt{G_{II}/G_I}$ At Various Longitudinal Crack Lengths.

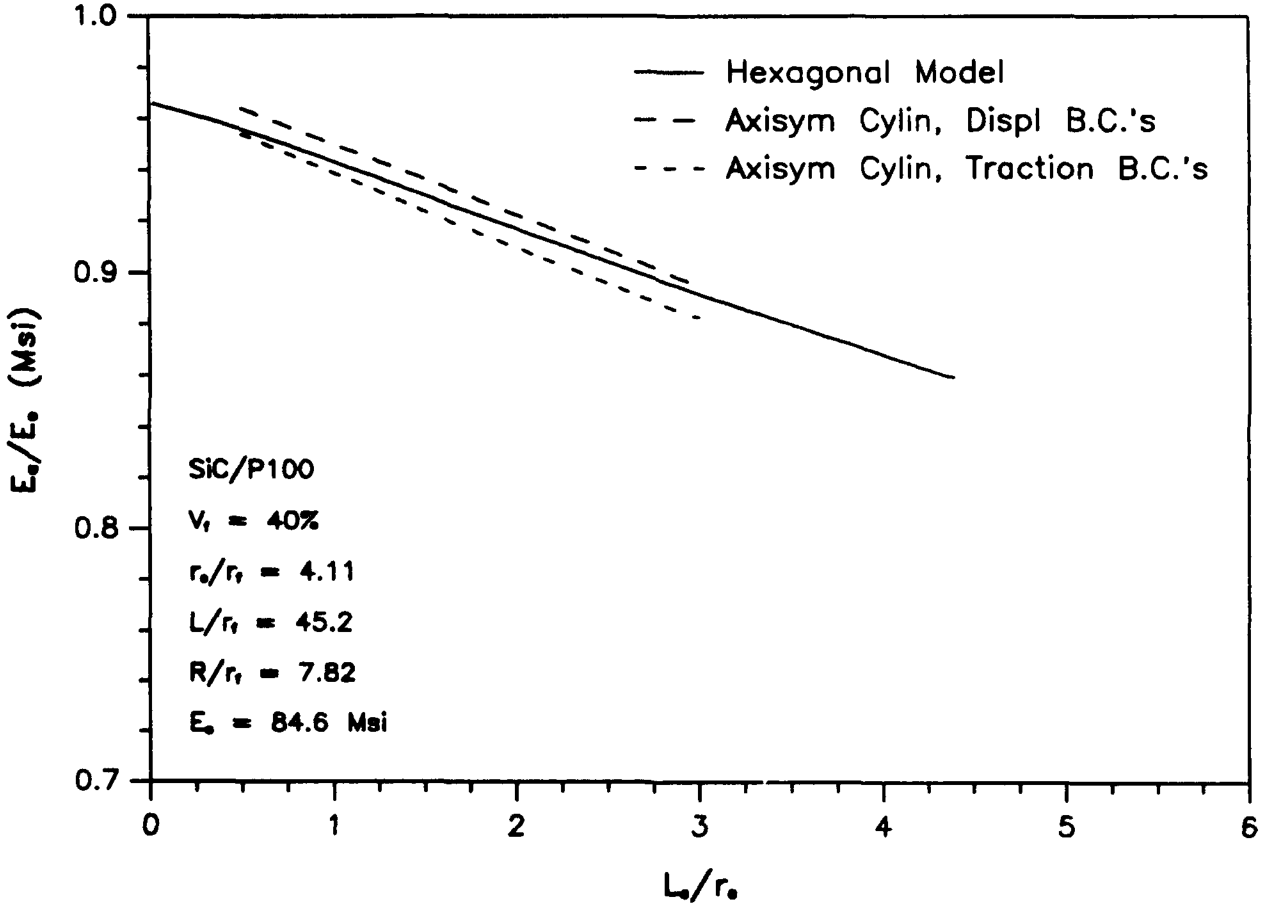

Figure 54. Effective Axial Modulus Of Composite Consisting Of An H-Shaped Crack Array With Various Longitudinal Crack Extension.

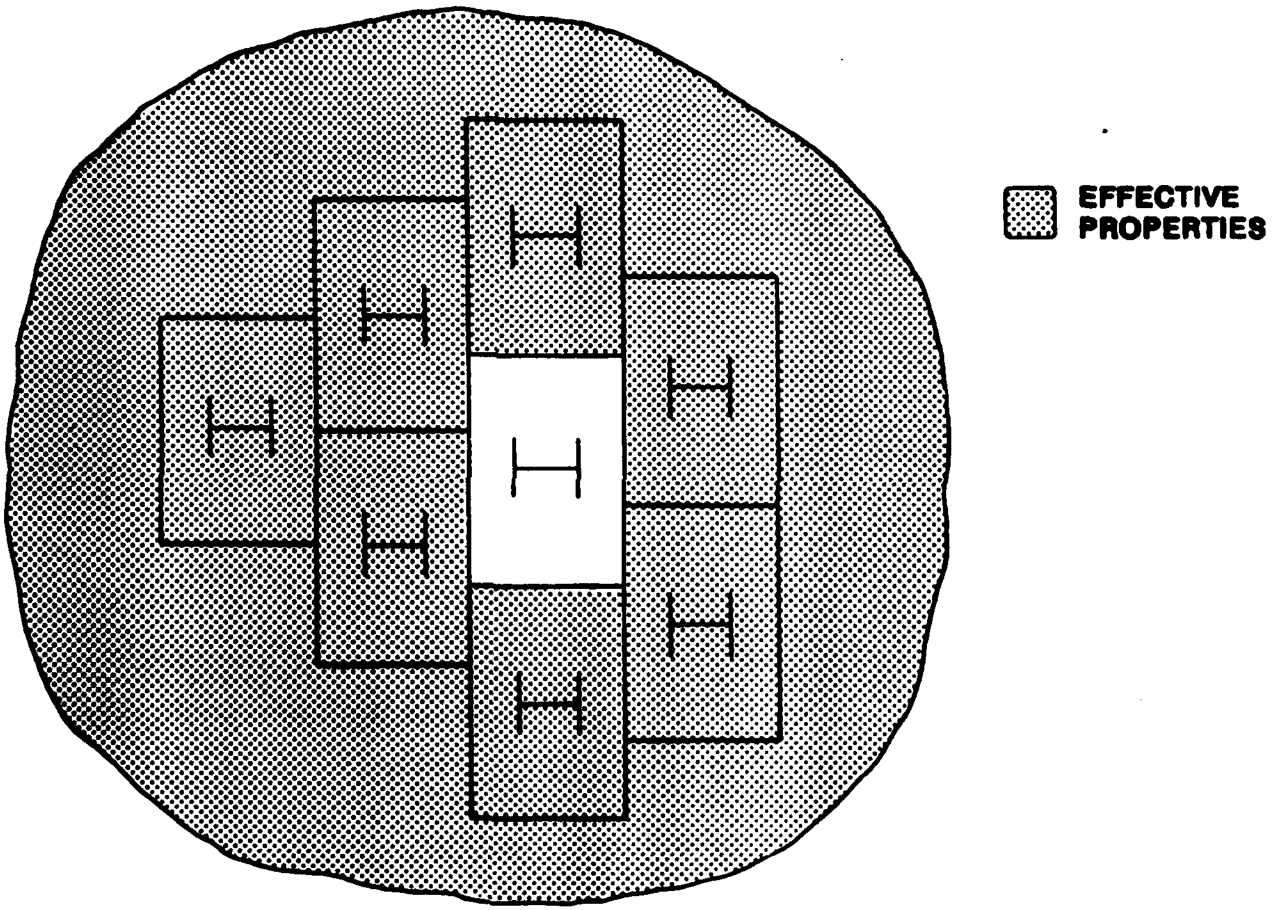

Figure 55. Generalized Self–Consistent Scheme For Material Failure Model.

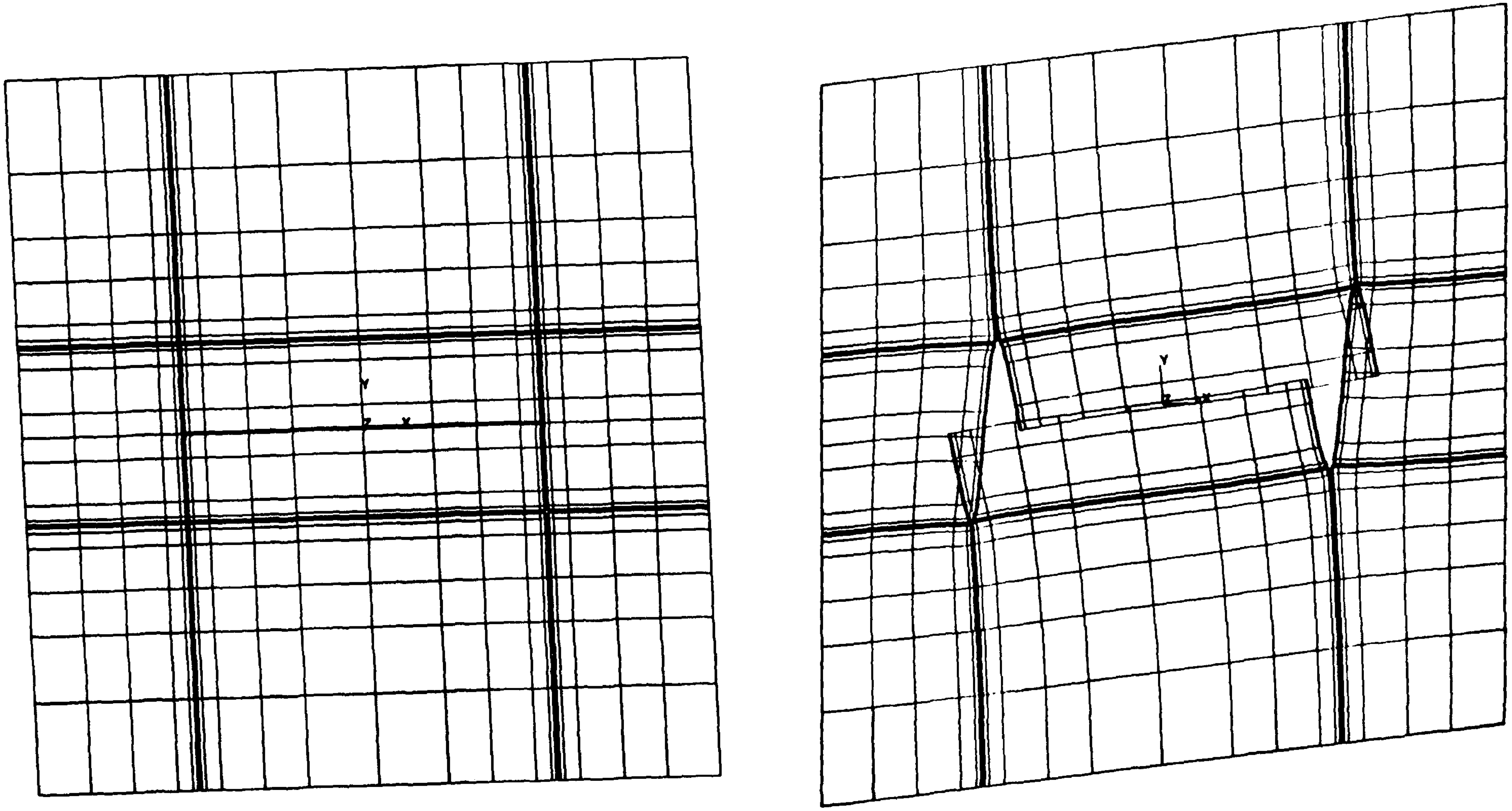

(a) Original Mesh

(b) Deformed Mesh

Figure 56. Finite Element Model For Shear Module Analysis.

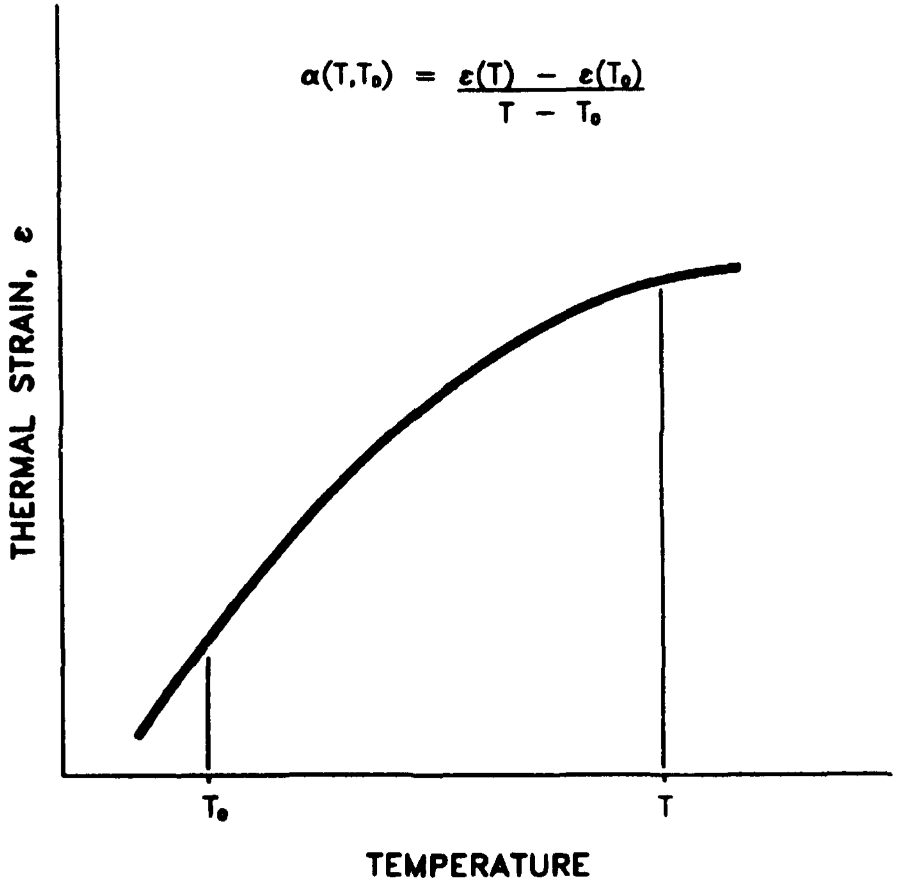

Figure 57. Secant TEC.

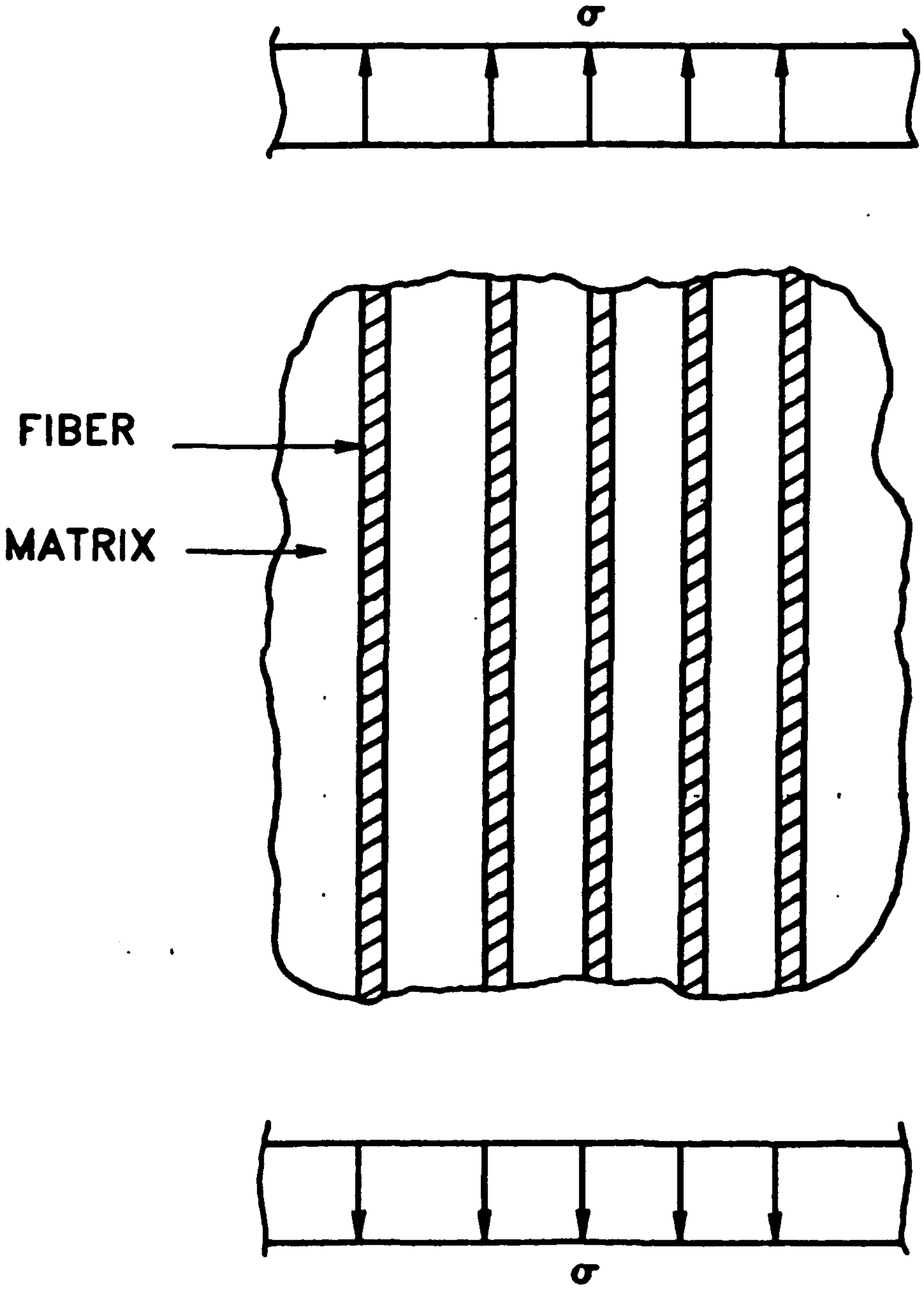

Figure 58. A one-dimensional model for a undirectional fiber composite

APPENDIX A

APPENDIX A

EVALUATION OF ELASTIC PROPERTIES OF A CYLINDER WITH A CENTRAL H-SHAPED CRACK

We apply (2-4) to evaluate the properties of a cracked cylinder as shown in Figure 45. We are interested only in the axisymmetric properties. We first apply to the surface of the cracked cylinder an axisymmetric displacement

$$\begin{aligned} u_z\,(S) &= \epsilon^{o}_{zz}\, Z \\ u_r\,(S) &= \epsilon^{o}_{rr}\, R \\ u_\theta\,(S) &= 0 \end{aligned} \qquad \text{(A-1)}$$

The axisymmetric effective moduli are defined by

$$\begin{aligned} \bar{\sigma}_{zz} &= n^{*}\epsilon^{o}_{zz} + 2l^{*}\epsilon^{o}_{rr} \\ \frac{1}{2}\left(\bar{\sigma}_{rr} + \bar{\sigma}_{\theta\theta}\right) &= l^{*}\epsilon^{o}_{zz} + 2k^{*}\epsilon^{o}_{rr} \end{aligned} \qquad \text{(A-2)}$$

Effective axial Young's modulus E^{*}_{A} and associated Poisson's ratio ν^{*}_{A} are defined in terms of these by

$$\begin{aligned} E^{*}_{A} &= n^{*} - 4k^{*}\nu^{*2}_{A} \\ \nu^{*}_{A} &= k^{*}/2l^{*} \end{aligned} \qquad \text{(A-3)}$$

Next we apply the loads

$$\sigma_{zz} = \sigma^{o}_{zz} \qquad \sigma_{rz} = \sigma_{\theta z} = 0 \qquad on \;\; Z = \pm L$$

$$\sigma_{rr} = \sigma^{o}_{rr} \qquad \sigma_{rz} = \sigma_{\theta z} = 0 \qquad on \;\; r = R \tag{A-4}$$

Then

$$\bar{\epsilon}_{zz} + \gamma_{zz} = \frac{\sigma^{o}_{zz}}{E^*_A} - 2\frac{\nu^*_A}{E^*_A}\sigma^{o}_{rr}$$

$$\frac{1}{2}\left(\bar{\epsilon}_{rr} + \bar{\epsilon}_{\theta\theta}\right) + \frac{1}{2}\left(\gamma_{rr} + \gamma_{\theta\theta}\right) = -\frac{\nu^*_A}{E^*_A}\sigma^{o}_{zz} + \left[\frac{1}{2k*} + \frac{2\nu^{*2}_A}{E^*_A}\right]\sigma^{o}_{rr} \tag{A-5}$$

where

$$\gamma_{zz} = \frac{1}{V}\int_{S_c}\left[u_z\right] n_z \, dS$$

$$\gamma_{rr} + \gamma_{\theta\theta} = \frac{1}{V}\int_{S_c}\left[u_r\right] n_r \, dS \tag{A-6}$$

Here V is the cylinder volume and S_c is the surface of the HSC.

Evaluating the averages and the surface integrals numerically, we obtain the values of E^*_A and ν^*_A in the two cases.